**Single-Cell Profiling of Paracrine Network and Immune Landscape in Non-Alcoholic Steatohepatitis**

by

Henry Kuang

A dissertation submitted in partial fulfillment
of the requirements for the degree of
Doctor of Philosophy
(Cellular and Molecular Biology)
in the University of Michigan
2020

Doctoral Committee:

      Professor Jiandie Lin, Chair
      Associate Professor Ken Inoki
      Associate Professor Carey Lumeng
      Professor Ormond MacDougald

Henry Kuang

henrykg@umich.edu

ORCID iD:  0000-0002-1957-6726

## Dedication

This dissertation is dedicated to all my past, present, and future mentors, both in and out of academia, regardless of our conflicts and disagreements, for being a part of who I am.

# Acknowledgements

I also want to credit my academic community and administrative support, particularly the MSTP and CMB programs. The MSTP program includes our current director Ron Koenig and administrative staff who have cared for me for 7 years now, Justine Hein, Ellen Elkin, Hilkka Ketola, Laurie Koivupalo, Liz Bowman, and Gretchen Aland. The CMB program has included director Bob Fuller and admin staff Pat Ocelnik, Margarita Bekiares, Jessica Kijek, and Lauren

**Table of Contents**

# List of Figures

**Abstract**

The liver is a heterogeneous organ comprising a diverse array of cells including parenchymal hepatocytes, and non-parenchymal cells (NPCs) including endothelial cells, hepatic stellate cells, cholangiocytes, and various immune cells. These different cell types function in concert to regulate hepatic metabolism and maintain tissue homeostasis. Non-alcoholic fatty liver disease (NAFLD) is a major hepatic comorbidity of metabolic syndrome that is characterized by pathogenic fat accumulation. Chronic NAFLD may progress to non-alcoholic steatohepatitis (NASH), an inflammatory condition that is associated with liver injury, immune cell infiltration, and liver fibrosis, and increases the risk for end-stage liver diseases such as cirrhosis and hepatocellular carcinoma. Despite the prominent roles of NPCs in NASH pathogenesis, the molecular nature of intercellular crosstalk among different liver cell types and their reprogramming in disease remains poorly understood.

Single-cell RNA sequencing (scRNA-seq) is a powerful technique for unraveling cellular heterogeneity in complex tissue through profiling transcriptomes of individual cells. In my thesis research, I performed scRNA-seq on NPCs isolated from healthy and diet-induced NASH mouse livers to dissect the paracrine signaling network and to uncover the immune cell landscape in NASH. We found that each cell type exhibited enriched expression of a unique subset of secreted ligands and membrane receptors, in a restricted pattern conserved from mouse to human. We confirmed expression for this paracrine network through quantitative proteomics and found macrophages and stellate cells to be major hubs of ligands and receptors which were upregulated in NASH. The hepatic stellate cells (HSCs) provide a source of stellakines which are predicted to act on endothelial and immune cells. Functionally, we showed that HSCs express a class of G-protein coupled receptors that regulate cellular contractility in response to vasoactive ligands.

ScRNA-seq revealed a highly disease-specific population of NASH-associated macrophages (NAMs) marked by abundant expression of marker genes including Trem2 and Gpnmb. NAMs

were found at higher levels in both human and mouse NASH and decreased upon dietary and therapeutic interventions for NASH. Their transcriptional profile indicates a propensity for phagocytosis, antigen presentation, and extracellular matrix remodeling, illustrating a potentially important role for NAMs in NASH progression. Tracing hematopoietic cells through bone marrow transplantation, we demonstrated that NAMs originate from the bone marrow and not tissue-resident progenitors. We developed a Trem2 Cre knockin mouse strain to track the emergence of NAMs during NASH progression. Our mouse liver injury and fibrosis assays were unaffected by Trem2 knockout in NASH, indicating Trem2 itself may be unimportant in NASH, but the role of the NAMs they mark are not yet precluded from pathophysiology. Finally, we discovered that NASH is linked to liver CD8+ T cell exhaustion, which is characterized by high levels of PD1 and LAG3 expression and diminished IFNγ, IL2, and TNFα secretion upon T cell stimulation. NASH-associated T cell exhaustion is attenuated by the adipose hormone Neuregulin 4 (NRG4), which protects mice from diet-induced NASH and hepatocellular carcinoma. Taken together, my thesis work has revealed the transcriptomic nature of liver cell heterogeneity, the global landscape of cell-cell signaling in the liver, and NASH-associated NPC reprogramming at a single-cell resolution.

**Chapter 1**
**Introduction**

Through evolution, unicellular organisms have developed into more complex multicellular beings, conferring numerous advantages. The specialization of a progenitor into distinct cell types allows for division of roles and therefore, more advanced functions such as whole-body metabolism. In higher-order beings such as mammals, the different cell types of each tissue cooperatively regulate energy homeostasis and growth. The tissues responsible for maintaining homeostasis in the face of a changing environment are heterogeneous in cellular composition. These organs in mammals include the liver, adipose tissue, and pancreas. The heterogeneity of cell types within these tissue allows them to accomplish this difficult task. The liver alone comprises a parenchymal population of hepatocytes, as well as the non-parenchymal populations of hepatic stellate cells, endothelial cells, epithelial cells, and Kupffer and other immune cells. These subsets each have distinct roles but also function together in a tightly-regulated paracrine network.

A critical aspect of the cell types in metabolic tissue is the specific reprogramming they undergo in diseases such as metabolic syndrome and non-alcoholic steatohepatitis (NASH). Research on the pathophysiology of these conditions has provided some insight into their whole-body effects, such as insulin resistance and lipid accumulation. However, it has become clear that metabolic diseases are multi-factorial and involve contributions from each of the different cell types within the tissue. Growing bodies of research have implied secreted ligand-receptor interactions are key to regulating whole-body metabolism, and that perturbations in these communications lead to disease. This paradigm necessitates a better understanding of each cell-type's function as well as the crosstalk network between them. Our present understanding of the development of these diverse niches, and the paracrine network between them, remains basic.

Single-cell genomics is a recently developing technology that has demonstrated great potential in dissecting the underlying cellular heterogeneity in these tissues. As cell-sorting, fluidics, and droplet-based techniques become more sophisticated, we are able to analyze these niches at a single-cell resolution with unprecedented depth. This combined with developing informatics approaches has powerful advantages over traditional whole-tissue studies. The first major benefit to this is from a functional perspective. At its most basic level, single-cell RNA sequencing (scRNA-seq) provides a transcriptome of each cell, indicating its identity and implying its biological function. scRNA-seq can also be utilized to map the developmental trajectory of cells and determine the nature of multipotent progenitors. In the context of disease, scRNA-seq unravels the cellular transitions that occur, providing novel insights into the mechanisms of pathogenesis. Most importantly, scRNA-seq now allows us to determine the true sources of secreted ligands and their membrane receptors within tissue. With this we may map out the intercellular crosstalk networks that govern physiology and disease. Studying cellular heterogeneity at a single-cell level thus begets a deeper understanding of whole-body physiology.

**Cellular heterogeneity as an intrinsic property of metabolic tissues**

The liver is a hub for metabolism, responsible for duties which range from storing nutrients and converting them into usable forms for other tissue, maintenance of circulating plasma proteins, to xenobiotic processing and waste handling. Many of these tasks are classically thought to be carried out by the major cell population of the liver, the hepatocyte. In addition to hepatocytes, the non-parenchymal cell (NPC) population of the liver includes endothelial cells lining the vasculature, the bile-duct lining epithelial cells, the hepatic stellate cells, and various immune cell populations including B cells and plasma cells, T cells, monocytes, and its own resident macrophage population, Kupffer cells (Friedman, 2008; Krenkel and Tacke, 2017; Poisson et al., 2017; Robinson et al., 2016; Tabibian et al., 2013). Even more in-depth is the broad spectrum of physiological differences within each cell type. The liver is divided into units known as lobules, each with hepatocytes positioned in linear arrangements between the central vein and portal region consisting of the bile ducts, hepatic arteries, and portal vein (Hoehme et al., 2010; Teutsch, 2005). In the theory of 'zonation', it was thought that liver cells are graded in function between the central and portal regions to facilitate the flux of nutrients and metabolites between

them (Gebhardt and Matz-Soja, 2014; Jungermann and Katz, 1982; Jungermann and Kietzmann, 1996; Schleicher et al., 2015). Previous studies had utilized primarily histochemistry to infer the zonation of hepatocytes by proxy (Andersen et al., 1984; Feldmann et al., 1992; Jungermann et al., 1982). Some attempts had been made to discriminately isolate peri-portal and peri-central hepatocytes from each other and perform RNA-sequencing (Braeuning et al., 2006; Quistorff and Grunnet, 1987), and other researchers had utilized laser-capture microscopy to distinguish the two major hepatocyte groups (Saito et al., 2013). These methods can certainly provide a whole-transcriptome bulk view of zonation. However, to truly map the anticipated spectrum of function from the central to portal regions required a higher resolution than a mechanical separation of the lobules.

Utilizing fluorescence in-situ hybridization on liver, Halpern et al. localized a set of 6 highly-expressed 'landmark' genes that could consistently be used to infer zonation of hepatocytes. After dividing hepatic lobules into 9 concentric zones based on landmark gene profile, they correlated scRNA-seq expression of hepatocytes with these 6 genes to finally spatially map genes at a single-cell resolution on the liver zonation profile (Halpern et al., 2017). This redefining study determined that 50% of hepatic genes are zonated, much more than previously thought (Braeuning et al., 2006). Confirming the heterogeneity within hepatocytes, Halpern et al. found zonation in numerous pathways including oxidative phosphorylation, glucose and lipid metabolism, secretion of proteins, xenobiotic metabolism, glutathione processing, and bile acid synthesis. Interestingly, with this higher resolution, Halpern et al. were able to examine mid-lobule hepatocytes and found a sequential expression of bile-acid synthesis enzymes down the zonation profile. Several other liver-centric pathways were attributed to these mid-lobule regions including iron regulation and production of Igfbp2, a key regulator of the insulin growth factors. Indeed, with the power of scRNA-seq we now have a clearer picture of the division of labor within the hepatocytes and even more importantly, the spatial map of how these tasks are committed. The specialization of the mid-lobule populations implied there is still much more to learn regarding this age-old concept of zonation.

Because the liver receives all of the circulation of the digestive system, an important regulator of liver function are the endothelial cells. By acting as a barrier to pathogens and metabolites from

reaching hepatocytes, it seemed likely that these cells likely also exhibited zonation (Rafii et al., 2016; Strauss et al., 2017). Expanding on their previous study, Halpern paired endothelial cells with hepatocytes by performing a mild cell isolation. This results in duplexed endothelial hepatocyte pairs marked by CD31, which they then sequenced. Matching it with their previously uncovered hepatocyte zonation profile, they could then infer new landmark genes and construct a map of endothelial cell zonation in the liver at a single-cell level (Halpern et al., 2018). Just as in hepatocytes, they found endothelial cells to stratify along the portal to central axis for many pathways such as Wnt signaling. In finding that 35% of genes are zonated in the liver endothelial cells, Halpern et al. determine that there is likely also specialization of this population of cells. In addition to demonstrating the difference in function along the lobules' zonation profiles, they utilized the transcriptomes of the hepatocytes and endothelial cells to identify novel markers to 'map' this gradient. This zonation of endothelial cells was later confirmed by Xiong et al. in their single-cell profile of mouse livers in non-alcoholic steatohepatitis (Xiong et al., 2019). In this case, scRNA-seq was used to spatially map distinct cell populations and infer their role in organ function. Further cell populations in the liver have shown to be quite heterogeneous in their contributions to physiology such as the hepatic stellate cells, which will be discussed in a later section.

The pancreas is classically divided into the exocrine portion, which secretes enzymes critical in digestion of food, and the islet populations. The two major islet subpopulations are the beta and alpha cells which respectively produce insulin and glucagon, two of the most important anabolic and catabolic factors in the body. Major work has gone into understanding the development and dysregulation of these populations due to their central role in metabolism and specifically, diabetes. As the broad array of endocrine cells within the pancreas are interspersed into small islets, it is difficult to mark and trace their development. scRNA-seq studies have begun to uncover novel markers to distinguish between alpha and beta cells, as well as the other endocrine populations of the pancreas (Muraro et al., 2016; van Gurp et al., 2019). These endocrine cells are known to arise from a single common progenitor. Despite this, the large diversity of cells concentrated into the small islets have complicated lineage-tracing studies, resulting in an incomplete understanding of islet cell development. Single-cell technology has allowed investigators to pinpoint the transcriptional state of each progenitor as it differentiates through

time points, resulting in a more complete map of islet development (Byrnes et al., 2018; Scavuzzo et al., 2018; van Gurp et al., 2019). These studies have uncovered key transcriptional regulators in beta cell development, and also identified novel markers for future characterization of intermediate states in their development.

These initial studies have demonstrated a great potential for single-cell technologies in unraveling the heterogeneity of complex metabolic tissues, and mapping their developmental processes. Not only have they discovered novel cell populations and matched them with function, these studies have identified markers for key subsets of cells, augmenting future studies on specific cell populations. By combining scRNA-seq data from the various tissues discussed, we may eventually develop a whole-body atlas of metabolism. Such a comprehensive map could provide researchers an understanding of the molecular basis for whole-body changes in physiology.

**Re-evaluating adipose tissue heterogeneity and development**

Another crucial tissue in regulating peripheral metabolism is the adipose. It is now well known that adipose tissue is a highly diverse and active tissue with much more function than simple energy storage. The diverse niche of adipose tissues include adipocytes, and stromal-vascular fraction populations including fibroblasts, endothelial cells, smooth-muscle cells, adipocyte progenitors, and immune cells. The major cell type in adipose tissue, the adipocyte, already exists in subtypes including white, brown, and beige, with differing function and localization (Chechi et al., 2013; Harms and Seale, 2013). Two major categories of white adipose depots are the vascular and subcutaneous types (Gesta et al., 2007; Rosen and MacDougald, 2006). The white adipose comprises the majority of fat pads in humans, distinguishing themselves based on varying capacities for adipogenesis and metabolism. Additionally, these subtypes of white adipose display differing levels of susceptibility to inflammation and fibrosis, which links obesity to insulin resistance (Khan et al., 2009; Montague et al., 1998; Sun et al., 2013; Weisberg et al., 2003). These different adipocyte types result from multiple lineage pathways in their progenitor populations. As a result, a great deal of research has gone into understanding what drives these different modes of adipogenesis, an important topic to be discussed in a later section.

Regardless of development, the final function of these adipocytes plays a central role in regulating peripheral metabolism. In addition to its lipogenesis and storage capacity, adipose tissue is a substantial source of endocrine adipokine factors that regulate energy homeostasis and inflammation (Chen et al., 2017; Guo et al., 2017; Wang et al., 2015a; Wang et al., 2014). Furthermore, subsets of beige and brown adipocytes have well-established roles in thermogenesis (Chechi et al., 2013; Cohen et al., 2014). Though lipid storage, adipokine production, and thermogenesis have long been attributed to broad adipocyte categories such as white, brown, or beige, only indirect evidence has hinted that distinct subtypes of each were specialized for these roles (Lee et al., 2019; Lee et al., 2013a; Min et al., 2019). Lee et al. had previously demonstrated that a particular population of adipocyte and progenitors marked by expression of Tbx15 displayed high glycolytic capacity and enriched in subcutaneous depots, demonstrating heterogeneity of metabolism just within white adipocytes (Lee et al., 2017). Similarly in beige and brown fat, a similar dichotomy appeared to arise with respect to glycolysis regulation, wherein a beige progenitor population with myogenic markers such as Myod1 were found to give rise to glycolytic beige fat (Chen et al., 2019). Bertholet et al. demonstrated that certain beige adipocytes generate heat in the absence of UCP1-dependent uncoupling through patch clamp studies on proton leakage (Bertholet et al., 2017). These findings all hint at a functional heterogeneity among each adipocyte type, which scRNA-seq has begun to clarify.

A recent study by Rajbhandari et al. attempted to identify the adipocyte population that responds to Il10 (Rajbhandari et al., 2018) through thermogenesis by utilizing single-nuclei adipocyte sequencing (SNAP) to determine the heterogeneity in subcutaneous fat (Rajbhandari et al., 2019). They found 14 distinct populations of adipocytes, with diverse transcriptomic profiles landing on spectra of fatty acid metabolism, insulin signaling, hypoxia, angiogenesis, hormone response, and thermogenesis potentials. By performing SNAP-seq on mice facing cold stress and adrenergic challenge, Rajbhandari et al. identified a 'type-9' cluster of adipocytes highly responsive to both conditions as well as to Il10. Interestingly, this population was enriched for thermogenesis genes compared to other adipocytes, confirming their hypothesis that a specific subset of differentiated adipocytes responds to Il10 to induce thermogenesis, but also for the first time revealing their single-cell profiles. This division of labor for thermogenesis also exists in

brown fat, which was previously thought to be a homogenous population. To address the aforementioned idea that brown adipocytes may vary in UCP1 content and function, Song et al. performed scRNA-seq on adult brown fat (Song et al., 2020). Indeed, brown adipocytes funneled into two major populations, one with high thermogenic capacity (BA-H) and one with low (BA-L), with distinct expression profiles of UCP1, ADIPOQ, and CIDEA. Song et al. found BA-L to be extremely low in lipolysis, oxidative phosphorylation, and glycolysis, indicating they are metabolically inactive and low in classic thermogenesis compared to BA-H. Interestingly, BA-L had higher fatty acid uptake and futile-cycle thermogenesis through creatine metabolism, affirming prior evidence that certain adipocytes generate heat in the absence of UCP-1 (Bertholet et al., 2017). Isolating these novel cell subsets, Song et al. confirmed that BA-H have higher oxygen consumption rate than BA-L. These functionally important subsets of brown adipocytes are able to interconvert, as Song et al. show through LacZ tracing of gene markers. The BA-L appear to switch to BA-H in cold stress situations, and this process is reduced with age, potentially explaining the decline of brown thermogenesis in adults. These landmark scRNA-seq studies have demonstrated its potential to dissect the heterogeneity of fully-differentiated adipocytes. In confirming the specialization of function of these cells, we now better understand that their purpose reaches far beyond lipid storage and thermogenesis, and even these classic roles are divided among subsets.

White adipose tissue maintains a high level of plasticity, capable of drastically expanding in states of metabolic excess. This prevents ectopic lipid storage which may be detrimental to organ function (Lee et al., 2019; Shao et al., 2018; Sun et al., 2013). It is understood that hypertrophy of adipocytes, or growth in cell size, is maladaptive and contributes to metabolic disease. Conversely hyperplasia of adipocytes, or differentiation of more adipocyte progenitors, is the physiological mechanism for this expansion (Carobbio et al., 2017). The transcriptional pathways mediating these decisions are poorly understood primarily due to the diversity of adipocyte progenitors in the stromal population (Berry and Rodeheffer, 2013; Hepler et al., 2017; Ross et al., 2000; Sebo and Rodeheffer, 2019). Further complicating this diversity is the amount of fates that these progenitors can assume. Finally, the differentiation of these progenitors is a dynamic process with multiple intermediate transcriptional states (Gupta et al., 2012; Lee et al., 2012; Tang et al., 2008; Vishvanath et al., 2016).

ScRNA-seq allows for precise determination of these transcriptional states and identification of key intermediates in the differentiation of adipocytes. To focus on early developing adipocyte stages, Merrick et al. performed scRNA-seq on subcutaneous fat of p12 mice, identifying a highly proliferative progenitor population marked by DPP4 (Merrick et al., 2019). This multi-lineage DPP4 population demonstrated a high proliferative capacity and ability to differentiate into the ICAM1 and CD142 progenitors. These ICAM1 and CD142 intermediates were more committed to adipogenesis than the DPP4 progenitors, at last establishing a lineage hierarchy for adipocyte development. Indeed, the committed ICAM1 and CD142 progenitors had lower proliferative capacity, and were less suppressed to differentiate by TGFβ, than the DPP4 cells. Tracing studies confirmed DPP4 cells can progress into ICAM1 and CD142 progenitors, and interestingly, that the DPP4 mesenchymal progenitor pool is depleted in obesity, indicating they are an important precursor population involved in disease. Other single-cell studies concurrently demonstrated evidence for the progenitor pools in this hierarchy. Burl et al. isolated Lin-populations from mice treated with and without CL to stimulate proliferation and differentiation of the supposed progenitor populations. ScRNA-seq of these populations revealed two major progenitor populations, ASC1 and ASC2, in which ASC2 highly resembled the DPP4 population (Burl et al., 2018). Likewise, the ASC1 population which correlated the ICAM1 cells had higher adipogenesis potential. By determining the transcriptional signature of these progenitors, we now also can utilize marker genes to localize these progenitors in the tissue. Interestingly, these novel progenitor populations were found to be exhausted in obesity, indicating their depletion portends metabolic pathology. Future studies utilizing scRNA-seq may continue to refine our understanding of the adipogenesis pathway, eventually yielding interventions that direct healthier adipocyte hyperplasia in metabolic disease.

**Reprogramming of immune cells in metabolic disease**

An undeniable aspect of metabolic disease is the contributions from immune cells. Each metabolic tissue comprises a repertoire of resident immune cells including B cells, T cells, antigen-presenting dendritic cells, and the homeostatic resident macrophages (Krenkel and Tacke, 2017; Robinson et al., 2016). This immune landscape is drastically altered in metabolic disease, in which tissue inflammation is a classic pathogenic hallmark. Inflammatory

macrophages and T cells infiltrate adipose and liver to reconcile the excessive lipid accumulation in tissue, which leads to tissue inflammation and classic type 2 diabetes (Diehl and Day, 2017; Samuel and Shulman, 2018; Weisberg et al., 2003; Xu et al., 2003). In obesity, the resident adipose tissue macrophages (ATMs) accumulate around the pathogenic lipid droplets to contain them in the classic crown-like structures (Cho et al., 2014; Lumeng et al., 2007; Morris et al., 2013). Similarly, pathologic lipid accumulation in steatotic liver induces infiltration and localization of inflammatory macrophages (Krenkel et al., 2019a; Ritz et al., 2018), likely attempting to scavenge and clear the lipid droplets (Remmerie and Scott, 2018).

Given the similarities between liver and adipose tissue in NASH and obesity, respectively, it is somewhat unsurprising that the immune milieu undergoes similar transformations between them. ScRNA-seq studies in the NASH and cirrhotic liver has revealed a novel NASH-associated macrophage population (NAM). By performing scRNA-seq on the non-parenchymal fraction of NASH mouse livers, Xiong et al. identified a population marked by expression of the TREM2 gene, which resembles the liver-resident Kupffer cells and only arises in disease (Xiong et al., 2019). These NAMs' transcriptional profiles include marker genes such as GPNMB and CD9 which are highly specific among macrophages in the liver. The profile of NAMs speaks to a high capacity for lipid scavenging, extracellular matrix remodeling, and antigen presentation, indicating they likely play a homeostatic role in disease resolution. Xiong et al. found that beyond their functional implications, the differentiation of NAMs strongly correlated with the severity of disease, implying the population may be a useful marker for disease. These findings were subsequently corroborated in a single-cell study on human cirrhotic livers, which classified the subset as 'Scar Associated Macrophages (SAMac)' (Ramachandran et al., 2019). Initial studies have suggested that some of the key markers on this population such as TREM2 may play a protective role in chemical-induced liver injury (Perugorria et al., 2018). Although this promising finding implies a homeostatic role for NAMs, the exact function of the cell population remains unknown.

Interestingly, an analogous subset of TREM2-high ATMs was found in adipose tissue during obesity (Jaitin et al., 2019). ScRNA-seq profiling showed TREM2 deficient ATMs lost their unique transcriptional signature and were unable to congregate and form crown-like structures

following high-fat diet challenge, supporting the notion that these NAMs likely play a key role in scavenging of aberrant lipid accumulation. Furthermore, it draws a connection between TREM2 ablation and function of NAMs, as it would seem that this and other studies have found that knockout of TREM2 reduces the ability for macrophages to even differentiate into NAMs (Keren-Shaul et al., 2017). Future studies are called for to elucidate the role this cell population plays in pathogenesis. Moreover, it would seem that these disease macrophages appear even outside of metabolic disease. Studies in various non-metabolic tissue have identified transcriptionally identical macrophage populations to NAMs in other inflammatory conditions of lung (Sharif et al., 2014; Wu et al., 2015) and most notably, the brain (Keren-Shaul et al., 2017). Similar to studies in ATMs, the brain-resident microglial cells are reliant on the TREM2 expression to gain the entire 'Disease-Associated Macrophage (DAM)' profile (Keren-Shaul et al., 2017). Similar to in adipose tissue, multiple groups have found that this loss of DAM signature and ablation of TREM2 expression is detrimental to the ability to effectively clear amyloid plaques in Alzheimer's disease (Wang et al., 2015b; Zhou et al., 2020).

These numerous studies in independent resident macrophage populations throughout the body suggest a central lineage pathway that macrophages undergo in tissue inflammatory conditions. These TREM2-hi macrophage populations seem to appear in any inflammatory condition. Given this global potential, it is likely that these disease-associated macrophages derive from the hematopoietic monocyte population rather than the final resident macrophage populations which they resemble. Clarification as to the exact origins of these universal cells will be needed. More importantly, the ubiquity of these TREM2-high cells indicates they are critical for physiological response to disease. Their importance in clearance of amyloid plaques and maintenance of lipid droplet size in adipose implies they play a crucial role in clearance of aberrant material, likely lipid droplets in the NASH liver. These suggest it will be crucial to dissect their exact role in NASH and obesity for developing future therapeutics.

Another key facet of the inflammatory response in metabolic disease is their eventual progression to cancer. Chronic inflammation and repeated cell turnover results in mutations and oncogenesis, as in the case of NASH-associated hepatocellular carcinoma (HCC) (Anstee et al., 2019; Kutlu et al., 2018). HCC is a heterogeneous malignancy, with few notable unifying

mutations in the cells of origin, which are accepted to be the hepatocytes (Cancer Genome Atlas Research Network. Electronic address and Cancer Genome Atlas Research, 2017; Chen et al., 2018). ScRNA-seq on human HCC has confirmed this (Zheng et al., 2018). This heterogeneity implies that the primary 'hit' that contributes to the NASH-HCC axis is not the hepatocyte itself, but the injurious immune cells in NASH. An early study profiled T-cells at a single-cell level to determine their contributions to the HCC patient (Zheng et al., 2017), identifying enriched subsets of Treg and exhausted CD8+ T cells. Zheng et al. demonstrated the potential for checkpoint therapy in T cells in alleviating NASH and HCC, an already active field of study. A more expansive study of immune cells in HCC later identified important antigen-presenting cell populations in the tumor microenvironment, including dendritic cells (Zhang et al., 2019). Interestingly, they found a subset of tumor-associated macrophages highly reminiscent of NAMs by transcriptomic signature, which were strongly associated with poor HCC prognosis, further supporting the importance of NAMs in disease progression. ScRNA-seq has been used to shed light on the complex inflammatory landscape that contributes to chronic disease progression.

**Shaping of tissue metabolism by non-parenchymal cells**

To this point, we have shown how single-cell transcriptomics can map the function and development of different cell types in metabolic tissue. The depth of modern sequencing has allowed these studies to include the less common non-parenchymal cell populations, leading to a complete picture of the cellular niches that comprise the tissue. Prior research has highly indicated that these non-parenchymal populations may potentially play significant roles in regulating the paracrine landscape and tissue metabolism. ScRNA-seq has shed light on the influence that these rarer cells have in their microenvironments. In adipose tissue, it had been theorized that stromal vascular populations interacted with critical immune-modulating populations such as Treg and innate lymphoid cells (Feuerer et al., 2009; Molofsky et al., 2013; Molofsky et al., 2015; Xu et al., 2003). It was previously known that Il33 acted on Treg populations in fat to inhibit inflammation (Molofsky et al., 2015; Vasanthakumar et al., 2015), however, the source of Il33 remained elusive. Spallanzani et al. utilized scRNA-seq to characterize a distinct subset of mesenchymal stromal cells responsible for production of Il33, a critical cytokine regulator of Treg cells, in visceral adipose tissue (Spallanzani et al., 2019). They distinguished these stromal cells to be of the mesothelial, and as having low adipogenesis

capacity compared to their non-mesothelial counterparts. Intriguingly, the crosstalk between these stromal cells and Treg is highly regulated with aging and metabolic disease. They have therefore demonstrated how non-parenchymal populations shape the metabolic profile of these tissues. The lymphocyte population itself is quite important for shaping adipose metabolism. The previously mentioned study on SNAP-seq of cold-stressed adipocytes utilized scRNA-seq connect Il10 with adipose metabolism. Sequencing demonstrated B and T cells to be the major local source for Il10 (Rajbhandari et al., 2019), thus lending to a direct paracrine interaction in which immune cells regulate the thermogenesis function of adipocytes.

In the context of liver, one vastly-underappreciated group of cells prior to scRNA-seq was the hepatic stellate cells. Studies on these cells have been confounded by the difficulty in isolation of this relatively sparse population (Mederacke et al., 2015). Originally discovered as vitamin A repositories (Wake, 1971), they are now known to be the major contributors of fibrosis in the liver (Friedman, 2008; Friedman et al., 1985; Mederacke et al., 2013). Single-cell studies have now uncovered that this population is, like hepatocytes and endothelial cells, quite heterogeneous. Utilizing carbon tetrachloride to stimulate stellate cells through liver injury, Krenkel et al. performed scRNA-seq on non-parenchymal cells gating out endothelial and immune cells. They found collagen-enriched stellate cells to be distinct from the myofibroblast population of the liver, and indicated novel markers for these stellate cells such as FCNA (Krenkel et al., 2019b). Importantly, in a parallel study Dobie et al. demonstrated a zonation of stellate cells and division of labor. Performing scRNA-seq on PDGFRβ positive cells, which enriches for myofibroblasts and stellate cells, they were able to subdivide the stellate cell population into two groups wherein comprising markers that localized to either the central or portal regions of the liver (Dobie et al., 2019). Mapping these two populations into their respective zones, Dobie et al. determined that the centri-lobular stellate cells are the ones producing extracellular matrix in response to chemical-induced injury. These findings demonstrate a spatial heterogeneity within even the hepatic stellate cell population, and that this zonation denotes function in response to injury.

Beyond just the collagen production, scRNA-seq in healthy and NASH livers has uncovered a remarkable amount of interaction the HSCs likely have on liver metabolism (Dobie et al., 2019;

Ramachandran et al., 2019; Xiong et al., 2019). In their study on liver non-parenchymal cells, Xiong et al. uncovered an incredibly diverse pool of stellate-cell specific endocrine factors. These 'stellakines' include paracrine factors that strongly associate with receptors on endothelial cells and macrophages (Xiong et al., 2019). In particular, a large portion of these stellakines were inflammatory cytokines known to stimulate and attract immune cells, such as CCL2 and CCL11 (Deshmane et al., 2009; Garcia-Zepeda et al., 1996). A proportion of these stellakines interact directly with Kupffer cells. It is likely that these HSC-macrophage links contribute to inflammation and NAM development, as the expression of these ligand-receptor pairs correlates with disease progression. Other major functions of stellakines appear to be regulation of vascular tone and extracellular matrix remodeling, all of these pathways which were found to be regulated in NASH. Most intriguing was the discovery Xiong et al. made that activation of this HSC secretome is induced by endocrine cues such as Il11 and notably, TGFβ. These findings open an entirely new field of investigation that expands on the classic dogma that TGFβ induction simply stimulates fibrogenesis by stellate cells. Rather, stellate cell activation contributes to a remodeling of the entire paracrine landscape of the liver, including actions on endothelial and immune cells. This axis begins with immune cues to the stellate-cells, establishing them as a mediator of tissue inflammation. ScRNA-seq has therefore demonstrated completely new roles for these non-parenchymal cells in regulating metabolic tissue.

**Landscape of intercellular crosstalk in metabolic tissues**

The readout from scRNA-seq with the greatest potential is specification of receptors and ligands to their native cell-type. The centrality of the endocrine and paracrine system in regulating energy homeostasis indicates how important it is to map the network of ligand-receptor pairs within the body. Initial whole-tissue studies could only determine trends in total production of secreted factors by organs. With scRNA-seq, we are now able to quantitatively map expression of ligands and their receptors to each of their respective cell types, thus constructing a signaling network of metabolic tissue. Many groups have now begun to utilize this powerful method to draw previously unknown cell-cell interactions within metabolic tissue (Hepler et al., 2018; Lawlor et al., 2017; Ramachandran et al., 2019; Segerstolpe et al., 2016; Spallanzani et al., 2019; Xiong et al., 2019; Zhang et al., 2019). An understanding of the communication between cell-

types leads to a clearer idea of how effects on one cell type may perturb an entire organ system and therefore, pathology.

The communication between cell types has even uncovered disease pathways in the pancreas. Dysfunction of the islets heavily associates with type 1 and type 2 diabetes. Chronic type 2 diabetes results in an insufficiency of beta cells with lower insulin production. The transition to this deleterious transcriptional state is poorly characterized at a molecular level, complicated by the heterogeneity of pancreatic islets. To these ends, scRNA-seq was used to profile the islet cell populations in type 2 diabetes, uncovering a potential role for the under-characterized endocrine cells such as delta and gamma cells (Lawlor et al., 2017; Segerstolpe et al., 2016). A body of receptors including leptin receptor Lepr were found to be enriched specifically in the somatostatin-producing delta cells, indicating that it is likely the delta cells that mediate many of the endocrine effects previously thought to act on the beta cells. Numerous other previously undiscovered ligand-receptor pairs were identified to be enriched in alpha, beta, or gamma cells. Some of these factors were differentially expressed between diabetic and non-diabetic states. Although validation was not assessed in these studies, they indicate that the less-common cells in the islet may contribute to crosstalk in the pancreas, and that there are many paracrine interactions that may regulate beta cell function. ScRNA-seq has determined that a better understanding of the network of communication between islet cells may clarify the role of the pancreas in diabetes and metabolic disease.

A common theme of recent scRNA-seq studies has been the observation that rarer, more difficult to isolate cell populations are key players in the metabolic paracrine network. With the capacity to visualize the transcriptional repertoire of these smaller subsets, scRNA-seq has found that they contribute just as many receptors and ligands, if not more, than the major parenchymal cell types. In the liver, hepatic stellate cells (HSCs) were classically believed to be responsible for storage of retinoid compounds and production of fibrotic extracellular matrix material in injury. ScRNA-seq of liver non-parenchymal cells unveiled a novel angle that HSCs actually contribute the greatest number of ligands to the liver secretome (Xiong et al., 2019). These 'stellakines' carry a great diversity in function ranging from immune cell modulation, mentioned above, to regulation of vascular tone. In their profiling of the liver stellate cells, Xiong et al. found enrichment of

vasoactive peptides and receptors EDNRA, AGTR1A, and VIPR. In vitro studies confirmed that stellate cells do indeed respond to the respective ligands for these receptors to regulate contraction and relaxation of the stellate cells. Many angiocrine factors of the liver were found to be expressed by the endothelial cells, suggesting a paracrine link between those and stellate cells (Ramachandran et al., 2019; Xiong et al., 2019). Furthermore, these groups concurrently demonstrated an enrichment for Notch and TGFβ family signals enriched within the endothelial and stellate populations, pathways important in angiocrine maintenance (Rafii et al., 2016). Both groups demonstrated a connection between these paracrine pathways and NASH pathology, indicating that this cross-talk is likely important for disease. It is apparent then that the HSC contribution to liver function goes far beyond extracellular matrix remodeling, future studies will determine how these pathways regulate pathogenesis of liver disease.

These findings paint a picture that all cell types are much more multi-dimensional than previously thought. Beyond paracrine connections, factors secreted by cells may also contribute to a much more local niche. The 3D microenvironment of extracellular matrix material not only provides structure for the cells to sit in, but also directly bears on the function of cells within. A well-known aspect of metabolic disease is the accumulation of matrix components resulting in fibrosis, which is a pathological hallmark of liver injury. ScRNA-seq has shed light on key players in the remodeling of extracellular matrix networks. In the liver, scRNA-seq confirmed the central role of HSCs in producing matrix components that contribute to scarring (Dobie et al., 2019; Ramachandran et al., 2019; Xiong et al., 2019). Interestingly, they also uncovered novel cell populations including disease-associated macrophages which functionally produce remodeling factors, such as matrix metalloproteases. This supports the notion that extracellular matrix state represents a constant flux of building versus remodeling, much like the classic setting of osteoblast production versus osteoclast reuptake in bone maintenance. Though the beneficence of this fibrotic remodeling is not well understood, it seems likely that the structure and rigidity of the microenvironment plays an important role in controlling cell localization and function. ScRNA-seq will help to clarify this complex new modality of 'indirect' communication between cells sharing a niche.

**Concluding remarks**

Here I have highlighted how modern technologies have allowed us to focus our studies on metabolism. Single-cell transcriptomics opens up numerous fields of investigation, by elucidating the function of individual cell types, determining their developmental trajectory, and importantly, mapping the intercellular cross talk between them. As our understanding of the field evolves, we may utilize the findings from single-cell sequencing to enrich our hypothesis development. In this thesis work, I utilized single-cell RNA sequencing to map the cellular landscape in NASH liver, and then highlight key findings in the immune landscape which we found in NASH. This includes the discovery that hepatic stellate cells contribute to immune response signaling. Following chapters will begin to attempt to dissect the role these immune cells play in NASH pathology, including the expansion of a novel macrophage population in NASH, and the functional exhaustion of CD8 positive T cells (Figure 1), with a final supplemental chapter highlighting the importance of endocrine interactions in regulating metabolism.
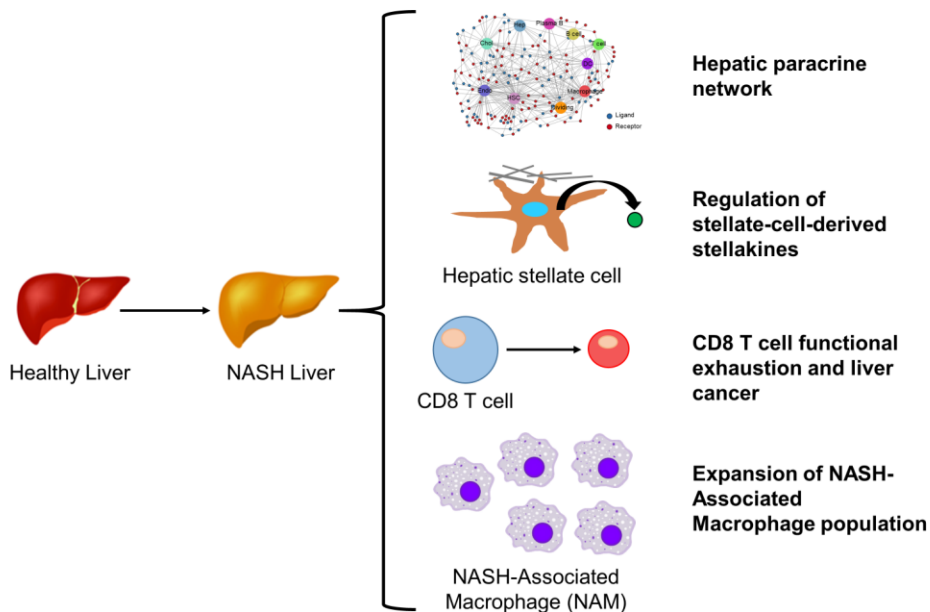


**Figure 1.1 Schematic of key findings of thesis studies**
In single-cell RNA sequencing of dietary NASH mouse model liver, in assembly of ligand-receptor network in liver, hepatic stellate cell secretion of stellakines, functional exhaustion of CD8 cytotoxic T cells and role in cancer, and emergence of novel disease-associated macrophage population.

**References**

Andersen, B., Zierz, S., and Jungermann, K. (1984). Alteration in zonation of succinate dehydrogenase, phosphoenolpyruvate carboxykinase and glucose-6-phosphatase in regenerating rat liver. Histochemistry *80*, 97-101.

Anstee, Q.M., Reeves, H.L., Kotsiliti, E., Govaere, O., and Heikenwalder, M. (2019). From NASH to HCC: current concepts and future challenges. Nat Rev Gastroenterol Hepatol *16*, 411-428.

Berry, R., and Rodeheffer, M.S. (2013). Characterization of the adipocyte cellular lineage in vivo. Nat Cell Biol *15*, 302-308.

Bertholet, A.M., Kazak, L., Chouchani, E.T., Bogaczynska, M.G., Paranjpe, I., Wainwright, G.L., Betourne, A., Kajimura, S., Spiegelman, B.M., and Kirichok, Y. (2017). Mitochondrial Patch Clamp of Beige Adipocytes Reveals UCP1-Positive and UCP1-Negative Cells Both Exhibiting Futile Creatine Cycling. Cell Metab *25*, 811-822 e814.

Braeuning, A., Ittrich, C., Kohle, C., Hailfinger, S., Bonin, M., Buchmann, A., and Schwarz, M. (2006). Differential gene expression in periportal and perivenous mouse hepatocytes. FEBS J *273*, 5051-5061.

Burl, R.B., Ramseyer, V.D., Rondini, E.A., Pique-Regi, R., Lee, Y.H., and Granneman, J.G. (2018). Deconstructing Adipogenesis Induced by beta3-Adrenergic Receptor Activation with Single-Cell Expression Profiling. Cell Metab *28*, 300-309 e304.

Byrnes, L.E., Wong, D.M., Subramaniam, M., Meyer, N.P., Gilchrist, C.L., Knox, S.M., Tward, A.D., Ye, C.J., and Sneddon, J.B. (2018). Lineage dynamics of murine pancreatic development at single-cell resolution. Nat Commun *9*, 3922.

Cancer Genome Atlas Research Network. Electronic address, w.b.e., and Cancer Genome Atlas Research, N. (2017). Comprehensive and Integrative Genomic Characterization of Hepatocellular Carcinoma. Cell *169*, 1327-1341 e1323.

Carobbio, S., Pellegrinelli, V., and Vidal-Puig, A. (2017). Adipose Tissue Function and Expandability as Determinants of Lipotoxicity and the Metabolic Syndrome. Adv Exp Med Biol *960*, 161-196.

Chechi, K., Carpentier, A.C., and Richard, D. (2013). Understanding the brown adipocyte as a contributor to energy homeostasis. Trends Endocrinol Metab *24*, 408-420.

Chen, J., Zaidi, S., Rao, S., Chen, J.S., Phan, L., Farci, P., Su, X., Shetty, K., White, J., Zamboni, F.*, et al.* (2018). Analysis of Genomes and Transcriptomes of Hepatocellular Carcinomas Identifies Mutations and Gene Expression Changes in the Transforming Growth Factor-beta Pathway. Gastroenterology *154*, 195-210.

Chen, Y., Ikeda, K., Yoneshiro, T., Scaramozza, A., Tajima, K., Wang, Q., Kim, K., Shinoda, K., Sponton, C.H., Brown, Z.*, et al.* (2019). Thermal stress induces glycolytic beige fat formation via a myogenic state. Nature *565*, 180-185.

Chen, Z., Wang, G.X., Ma, S.L., Jung, D.Y., Ha, H., Altamimi, T., Zhao, X.Y., Guo, L., Zhang, P., Hu, C.R.*, et al.* (2017). Nrg4 promotes fuel oxidation and a healthy adipokine profile to ameliorate diet-induced metabolic disorders. Mol Metab *6*, 863-872.

Cho, K.W., Morris, D.L., DelProposto, J.L., Geletka, L., Zamarron, B., Martinez-Santibanez, G., Meyer, K.A., Singer, K., O'Rourke, R.W., and Lumeng, C.N. (2014). An MHC II-dependent activation loop between adipose tissue macrophages and CD4+ T cells controls obesity-induced inflammation. Cell Rep *9*, 605-617.

Cohen, P., Levy, J.D., Zhang, Y., Frontini, A., Kolodin, D.P., Svensson, K.J., Lo, J.C., Zeng, X., Ye, L., Khandekar, M.J.*, et al.* (2014). Ablation of PRDM16 and beige adipose causes metabolic dysfunction and a subcutaneous to visceral fat switch. Cell *156*, 304-316.

Deshmane, S.L., Kremlev, S., Amini, S., and Sawaya, B.E. (2009). Monocyte chemoattractant protein-1 (MCP-1): an overview. J Interferon Cytokine Res *29*, 313-326.

Diehl, A.M., and Day, C. (2017). Cause, Pathogenesis, and Treatment of Nonalcoholic Steatohepatitis. N Engl J Med *377*, 2063-2072.

Dobie, R., Wilson-Kanamori, J.R., Henderson, B.E.P., Smith, J.R., Matchett, K.P., Portman, J.R., Wallenborg, K., Picelli, S., Zagorska, A., Pendem, S.V.*, et al.* (2019). Single-Cell Transcriptomics Uncovers Zonation of Function in the Mesenchyme during Liver Fibrosis. Cell Rep *29*, 1832-1847 e1838.

Feldmann, G., Scoazec, J.Y., Racine, L., and Bernuau, D. (1992). Functional hepatocellular heterogeneity for the production of plasma proteins. Enzyme *46*, 139-154.

Feuerer, M., Herrero, L., Cipolletta, D., Naaz, A., Wong, J., Nayer, A., Lee, J., Goldfine, A.B., Benoist, C., Shoelson, S.*, et al.* (2009). Lean, but not obese, fat is enriched for a unique population of regulatory T cells that affect metabolic parameters. Nat Med *15*, 930-939.

Friedman, S.L. (2008). Hepatic stellate cells: protean, multifunctional, and enigmatic cells of the liver. Physiol Rev *88*, 125-172.

Friedman, S.L., Roll, F.J., Boyles, J., and Bissell, D.M. (1985). Hepatic lipocytes: the principal collagen-producing cells of normal rat liver. Proc Natl Acad Sci U S A *82*, 8681-8685.

Garcia-Zepeda, E.A., Rothenberg, M.E., Ownbey, R.T., Celestin, J., Leder, P., and Luster, A.D. (1996). Human eotaxin is a specific chemoattractant for eosinophil cells and provides a new mechanism to explain tissue eosinophilia. Nat Med *2*, 449-456.

Gebhardt, R., and Matz-Soja, M. (2014). Liver zonation: Novel aspects of its regulation and its impact on homeostasis. World J Gastroenterol *20*, 8491-8504.

Gesta, S., Tseng, Y.H., and Kahn, C.R. (2007). Developmental origin of fat: tracking obesity to its source. Cell *131*, 242-256.

Guo, L., Zhang, P., Chen, Z., Xia, H., Li, S., Zhang, Y., Kobberup, S., Zou, W., and Lin, J.D. (2017). Hepatic neuregulin 4 signaling defines an endocrine checkpoint for steatosis-to-NASH progression. J Clin Invest *127*, 4449-4461.

Gupta, R.K., Mepani, R.J., Kleiner, S., Lo, J.C., Khandekar, M.J., Cohen, P., Frontini, A., Bhowmick, D.C., Ye, L., Cinti, S.*, et al.* (2012). Zfp423 expression identifies committed preadipocytes and localizes to adipose endothelial and perivascular cells. Cell Metab *15*, 230-239.

Halpern, K.B., Shenhav, R., Massalha, H., Toth, B., Egozi, A., Massasa, E.E., Medgalia, C., David, E., Giladi, A., Moor, A.E.*, et al.* (2018). Paired-cell sequencing enables spatial gene expression mapping of liver endothelial cells. Nat Biotechnol *36*, 962-970.

Halpern, K.B., Shenhav, R., Matcovitch-Natan, O., Toth, B., Lemze, D., Golan, M., Massasa, E.E., Baydatch, S., Landen, S., Moor, A.E.*, et al.* (2017). Single-cell spatial reconstruction reveals global division of labour in the mammalian liver. Nature *542*, 352-356.

Harms, M., and Seale, P. (2013). Brown and beige fat: development, function and therapeutic potential. Nat Med *19*, 1252-1263.

Hepler, C., Shan, B., Zhang, Q., Henry, G.H., Shao, M., Vishvanath, L., Ghaben, A.L., Mobley, A.B., Strand, D., Hon, G.C.*, et al.* (2018). Identification of functionally distinct fibro-inflammatory and adipogenic stromal subpopulations in visceral adipose tissue of adult mice. Elife *7*.

Hepler, C., Vishvanath, L., and Gupta, R.K. (2017). Sorting out adipocyte precursors and their role in physiology and disease. Genes Dev *31*, 127-140.

Hoehme, S., Brulport, M., Bauer, A., Bedawy, E., Schormann, W., Hermes, M., Puppe, V., Gebhardt, R., Zellmer, S., Schwarz, M.*, et al.* (2010). Prediction and validation of cell alignment along microvessels as order principle to restore tissue architecture in liver regeneration. Proc Natl Acad Sci U S A *107*, 10371-10376.

Jaitin, D.A., Adlung, L., Thaiss, C.A., Weiner, A., Li, B., Descamps, H., Lundgren, P., Bleriot, C., Liu, Z., Deczkowska, A.*, et al.* (2019). Lipid-Associated Macrophages Control Metabolic Homeostasis in a Trem2-Dependent Manner. Cell *178*, 686-698 e614.

Jungermann, K., Heilbronn, R., Katz, N., and Sasse, D. (1982). The glucose/glucose-6-phosphate cycle in the periportal and perivenous zone of rat liver. Eur J Biochem *123*, 429-436.

Jungermann, K., and Katz, N. (1982). Functional hepatocellular heterogeneity. Hepatology *2*, 385-395.

Jungermann, K., and Kietzmann, T. (1996). Zonation of parenchymal and nonparenchymal metabolism in liver. Annu Rev Nutr *16*, 179-203.

Keren-Shaul, H., Spinrad, A., Weiner, A., Matcovitch-Natan, O., Dvir-Szternfeld, R., Ulland, T.K., David, E., Baruch, K., Lara-Astaiso, D., Toth, B.*, et al.* (2017). A Unique Microglia Type Associated with Restricting Development of Alzheimer's Disease. Cell *169*, 1276-1290 e1217.

Khan, T., Muise, E.S., Iyengar, P., Wang, Z.V., Chandalia, M., Abate, N., Zhang, B.B., Bonaldo, P., Chua, S., and Scherer, P.E. (2009). Metabolic dysregulation and adipose tissue fibrosis: role of collagen VI. Mol Cell Biol *29*, 1575-1591.

Krenkel, O., Hundertmark, J., Abdallah, A.T., Kohlhepp, M., Puengel, T., Roth, T., Branco, D.P.P., Mossanen, J.C., Luedde, T., Trautwein, C.*, et al.* (2019a). Myeloid cells in liver and bone marrow acquire a functionally distinct inflammatory phenotype during obesity-related steatohepatitis. Gut.

Krenkel, O., Hundertmark, J., Ritz, T.P., Weiskirchen, R., and Tacke, F. (2019b). Single Cell RNA Sequencing Identifies Subsets of Hepatic Stellate Cells and Myofibroblasts in Liver Fibrosis. Cells *8*.

Krenkel, O., and Tacke, F. (2017). Liver macrophages in tissue homeostasis and disease. Nat Rev Immunol *17*, 306-321.

Kutlu, O., Kaleli, H.N., and Ozer, E. (2018). Molecular Pathogenesis of Nonalcoholic Steatohepatitis- (NASH-) Related Hepatocellular Carcinoma. Can J Gastroenterol Hepatol *2018*, 8543763.

Lawlor, N., George, J., Bolisetty, M., Kursawe, R., Sun, L., Sivakamasundari, V., Kycia, I., Robson, P., and Stitzel, M.L. (2017). Single-cell transcriptomes identify human islet cell signatures and reveal cell-type-specific expression changes in type 2 diabetes. Genome Res *27*, 208-222.

Lee, K.Y., Luong, Q., Sharma, R., Dreyfuss, J.M., Ussar, S., and Kahn, C.R. (2019). Developmental and functional heterogeneity of white adipocytes within a single fat depot. EMBO J *38*.

Lee, K.Y., Sharma, R., Gase, G., Ussar, S., Li, Y., Welch, L., Berryman, D.E., Kispert, A., Bluher, M., and Kahn, C.R. (2017). Tbx15 Defines a Glycolytic Subpopulation and White Adipocyte Heterogeneity. Diabetes *66*, 2822-2829.

Lee, M.J., Wu, Y., and Fried, S.K. (2013a). Adipose tissue heterogeneity: implication of depot differences in adipose tissue for obesity complications. Mol Aspects Med *34*, 1-11.

Lee, Y.H., Petkova, A.P., and Granneman, J.G. (2013b). Identification of an adipogenic niche for adipose tissue remodeling and restoration. Cell Metab *18*, 355-367.

Lee, Y.H., Petkova, A.P., Mottillo, E.P., and Granneman, J.G. (2012). In vivo identification of bipotential adipocyte progenitors recruited by beta3-adrenoceptor activation and high-fat feeding. Cell Metab *15*, 480-491.

Lumeng, C.N., Bodzin, J.L., and Saltiel, A.R. (2007). Obesity induces a phenotypic switch in adipose tissue macrophage polarization. J Clin Invest *117*, 175-184.

Mederacke, I., Dapito, D.H., Affo, S., Uchinami, H., and Schwabe, R.F. (2015). High-yield and high-purity isolation of hepatic stellate cells from normal and fibrotic mouse livers. Nat Protoc *10*, 305-315.

Mederacke, I., Hsu, C.C., Troeger, J.S., Huebener, P., Mu, X., Dapito, D.H., Pradere, J.P., and Schwabe, R.F. (2013). Fate tracing reveals hepatic stellate cells as dominant contributors to liver fibrosis independent of its aetiology. Nat Commun *4*, 2823.

Merrick, D., Sakers, A., Irgebay, Z., Okada, C., Calvert, C., Morley, M.P., Percec, I., and Seale, P. (2019). Identification of a mesenchymal progenitor cell hierarchy in adipose tissue. Science *364*.

Min, S.Y., Desai, A., Yang, Z., Sharma, A., DeSouza, T., Genga, R.M.J., Kucukural, A., Lifshitz, L.M., Nielsen, S., Scheele, C.*, et al.* (2019). Diverse repertoire of human adipocyte subtypes develops from transcriptionally distinct mesenchymal progenitor cells. Proc Natl Acad Sci U S A *116*, 17970-17979.

Molofsky, A.B., Nussbaum, J.C., Liang, H.E., Van Dyken, S.J., Cheng, L.E., Mohapatra, A., Chawla, A., and Locksley, R.M. (2013). Innate lymphoid type 2 cells sustain visceral adipose tissue eosinophils and alternatively activated macrophages. J Exp Med *210*, 535-549.

Molofsky, A.B., Van Gool, F., Liang, H.E., Van Dyken, S.J., Nussbaum, J.C., Lee, J., Bluestone, J.A., and Locksley, R.M. (2015). Interleukin-33 and Interferon-gamma Counter-Regulate Group 2 Innate Lymphoid Cell Activation during Immune Perturbation. Immunity *43*, 161-174.

Montague, C.T., Prins, J.B., Sanders, L., Zhang, J., Sewter, C.P., Digby, J., Byrne, C.D., and O'Rahilly, S. (1998). Depot-related gene expression in human subcutaneous and omental adipocytes. Diabetes *47*, 1384-1391.

Morris, D.L., Cho, K.W., Delproposto, J.L., Oatmen, K.E., Geletka, L.M., Martinez-Santibanez, G., Singer, K., and Lumeng, C.N. (2013). Adipose tissue macrophages function as antigen-presenting cells and regulate adipose tissue CD4+ T cells in mice. Diabetes *62*, 2762-2772.

Muraro, M.J., Dharmadhikari, G., Grun, D., Groen, N., Dielen, T., Jansen, E., van Gurp, L., Engelse, M.A., Carlotti, F., de Koning, E.J.*, et al.* (2016). A Single-Cell Transcriptome Atlas of the Human Pancreas. Cell Syst *3*, 385-394 e383.

Perugorria, M.J., Esparza-Baquer, A., Oakley, F., Labiano, I., Korosec, A., Jais, A., Mann, J., Tiniakos, D., Santos-Laso, A., Arbelaiz, A.*, et al.* (2018). Non-parenchymal TREM-2 protects the liver from immune-mediated hepatocellular damage. Gut.

Poisson, J., Lemoinne, S., Boulanger, C., Durand, F., Moreau, R., Valla, D., and Rautou, P.E. (2017). Liver sinusoidal endothelial cells: Physiology and role in liver diseases. J Hepatol *66*, 212-227.

Quistorff, B., and Grunnet, N. (1987). Dual-digitonin-pulse perfusion. Concurrent sampling of periportal and perivenous cytosol of rat liver for determination of metabolites and enzyme activities. Biochem J *243*, 87-95.

Rafii, S., Butler, J.M., and Ding, B.S. (2016). Angiocrine functions of organ-specific endothelial cells. Nature *529*, 316-325.

Rajbhandari, P., Arneson, D., Hart, S.K., Ahn, I.S., Diamante, G., Santos, L.C., Zaghari, N., Feng, A.C., Thomas, B.J., Vergnes, L.*, et al.* (2019). Single cell analysis reveals immune cell-adipocyte crosstalk regulating the transcription of thermogenic adipocytes. Elife *8*.

Rajbhandari, P., Thomas, B.J., Feng, A.C., Hong, C., Wang, J., Vergnes, L., Sallam, T., Wang, B., Sandhu, J., Seldin, M.M.*, et al.* (2018). IL-10 Signaling Remodels Adipose Chromatin Architecture to Limit Thermogenesis and Energy Expenditure. Cell *172*, 218-233 e217.

Ramachandran, P., Dobie, R., Wilson-Kanamori, J.R., Dora, E.F., Henderson, B.E.P., Luu, N.T., Portman, J.R., Matchett, K.P., Brice, M., Marwick, J.A.*, et al.* (2019). Resolving the fibrotic niche of human liver cirrhosis at single-cell level. Nature *575*, 512-518.

Remmerie, A., and Scott, C.L. (2018). Macrophages and lipid metabolism. Cell Immunol *330*, 27-42.

Ritz, T., Krenkel, O., and Tacke, F. (2018). Dynamic plasticity of macrophage functions in diseased liver. Cell Immunol *330*, 175-182.

Robinson, M.W., Harmon, C., and O'Farrelly, C. (2016). Liver immunology and its role in inflammation and homeostasis. Cell Mol Immunol *13*, 267-276.

Rodeheffer, M.S., Birsoy, K., and Friedman, J.M. (2008). Identification of white adipocyte progenitor cells in vivo. Cell *135*, 240-249.

Rosen, E.D., and MacDougald, O.A. (2006). Adipocyte differentiation from the inside out. Nat Rev Mol Cell Biol *7*, 885-896.

Ross, S.E., Hemati, N., Longo, K.A., Bennett, C.N., Lucas, P.C., Erickson, R.L., and MacDougald, O.A. (2000). Inhibition of adipogenesis by Wnt signaling. Science *289*, 950-953.

Saito, K., Negishi, M., and James Squires, E. (2013). Sexual dimorphisms in zonal gene expression in mouse liver. Biochem Biophys Res Commun *436*, 730-735.

Samuel, V.T., and Shulman, G.I. (2018). Nonalcoholic Fatty Liver Disease as a Nexus of Metabolic and Hepatic Diseases. Cell Metab *27*, 22-41.

Scavuzzo, M.A., Hill, M.C., Chmielowiec, J., Yang, D., Teaw, J., Sheng, K., Kong, Y., Bettini, M., Zong, C., Martin, J.F.*, et al.* (2018). Endocrine lineage biases arise in temporally distinct endocrine progenitors during pancreatic morphogenesis. Nat Commun *9*, 3356.

Schleicher, J., Tokarski, C., Marbach, E., Matz-Soja, M., Zellmer, S., Gebhardt, R., and Schuster, S. (2015). Zonation of hepatic fatty acid metabolism - The diversity of its regulation and the benefit of modeling. Biochim Biophys Acta *1851*, 641-656.

Schwalie, P.C., Dong, H., Zachara, M., Russeil, J., Alpern, D., Akchiche, N., Caprara, C., Sun, W., Schlaudraff, K.U., Soldati, G*., et al.* (2018). A stromal cell population that inhibits adipogenesis in mammalian fat depots. Nature *559*, 103-108.

Sebo, Z.L., and Rodeheffer, M.S. (2019). Assembling the adipose organ: adipocyte lineage segregation and adipogenesis in vivo. Development *146*.

Segerstolpe, A., Palasantza, A., Eliasson, P., Andersson, E.M., Andreasson, A.C., Sun, X., Picelli, S., Sabirsh, A., Clausen, M., Bjursell, M.K*., et al.* (2016). Single-Cell Transcriptome Profiling of Human Pancreatic Islets in Health and Type 2 Diabetes. Cell Metab *24*, 593-607.

Shao, M., Vishvanath, L., Busbuso, N.C., Hepler, C., Shan, B., Sharma, A.X., Chen, S., Yu, X., An, Y.A., Zhu, Y*., et al.* (2018). De novo adipocyte differentiation from Pdgfrbeta(+) preadipocytes protects against pathologic visceral adipose expansion in obesity. Nat Commun *9*, 890.

Sharif, O., Gawish, R., Warszawska, J.M., Martins, R., Lakovits, K., Hladik, A., Doninger, B., Brunner, J., Korosec, A., Schwarzenbacher, R.E*., et al.* (2014). The triggering receptor expressed on myeloid cells 2 inhibits complement component 1q effector mechanisms and exerts detrimental effects during pneumococcal pneumonia. PLoS Pathog *10*, e1004167.

Song, A., Dai, W., Jang, M.J., Medrano, L., Li, Z., Zhao, H., Shao, M., Tan, J., Li, A., Ning, T*., et al.* (2020). Low- and high-thermogenic brown adipocyte subpopulations coexist in murine adipose tissue. J Clin Invest *130*, 247-257.

Spallanzani, R.G., Zemmour, D., Xiao, T., Jayewickreme, T., Li, C., Bryce, P.J., Benoist, C., and Mathis, D. (2019). Distinct immunocyte-promoting and adipocyte-generating stromal components coordinate adipose tissue immune and metabolic tenors. Sci Immunol *4*.

Strauss, O., Phillips, A., Ruggiero, K., Bartlett, A., and Dunbar, P.R. (2017). Immunofluorescence identifies distinct subsets of endothelial cells in the human liver. Sci Rep *7*, 44356.

Sun, K., Tordjman, J., Clement, K., and Scherer, P.E. (2013). Fibrosis and adipose tissue dysfunction. Cell Metab *18*, 470-477.

Tabibian, J.H., Masyuk, A.I., Masyuk, T.V., O'Hara, S.P., and LaRusso, N.F. (2013). Physiology of cholangiocytes. Compr Physiol *3*, 541-565.

Tang, W., Zeve, D., Suh, J.M., Bosnakovski, D., Kyba, M., Hammer, R.E., Tallquist, M.D., and Graff, J.M. (2008). White fat progenitor cells reside in the adipose vasculature. Science *322*, 583-586.

Teutsch, H.F. (2005). The modular microarchitecture of human liver. Hepatology *42*, 317-325.

van Gurp, L., Muraro, M.J., Dielen, T., Seneby, L., Dharmadhikari, G., Gradwohl, G., van Oudenaarden, A., and de Koning, E.J.P. (2019). A transcriptomic roadmap to alpha- and beta-cell differentiation in the embryonic pancreas. Development *146*.

Vasanthakumar, A., Moro, K., Xin, A., Liao, Y., Gloury, R., Kawamoto, S., Fagarasan, S., Mielke, L.A., Afshar-Sterle, S., Masters, S.L.*, et al.* (2015). The transcriptional regulators IRF4, BATF and IL-33 orchestrate development and maintenance of adipose tissue-resident regulatory T cells. Nat Immunol *16*, 276-285.

Vishvanath, L., MacPherson, K.A., Hepler, C., Wang, Q.A., Shao, M., Spurgin, S.B., Wang, M.Y., Kusminski, C.M., Morley, T.S., and Gupta, R.K. (2016). Pdgfrbeta+ Mural Preadipocytes Contribute to Adipocyte Hyperplasia Induced by High-Fat-Diet Feeding and Prolonged Cold Exposure in Adult Mice. Cell Metab *23*, 350-359.

Wake, K. (1971). "Sternzellen" in the liver: perisinusoidal cells with special reference to storage of vitamin A. Am J Anat *132*, 429-462.

Wang, G.X., Zhao, X.Y., and Lin, J.D. (2015a). The brown fat secretome: metabolic functions beyond thermogenesis. Trends Endocrinol Metab *26*, 231-237.

Wang, G.X., Zhao, X.Y., Meng, Z.X., Kern, M., Dietrich, A., Chen, Z., Cozacov, Z., Zhou, D., Okunade, A.L., Su, X.*, et al.* (2014). The brown fat-enriched secreted factor Nrg4 preserves metabolic homeostasis through attenuation of hepatic lipogenesis. Nat Med *20*, 1436-1443.

Wang, Y., Cella, M., Mallinson, K., Ulrich, J.D., Young, K.L., Robinette, M.L., Gilfillan, S., Krishnan, G.M., Sudhakar, S., Zinselmeyer, B.H.*, et al.* (2015b). TREM2 lipid sensing sustains the microglial response in an Alzheimer's disease model. Cell *160*, 1061-1071.

Weisberg, S.P., McCann, D., Desai, M., Rosenbaum, M., Leibel, R.L., and Ferrante, A.W., Jr. (2003). Obesity is associated with macrophage accumulation in adipose tissue. J Clin Invest *112*, 1796-1808.

Wu, K., Byers, D.E., Jin, X., Agapov, E., Alexander-Brett, J., Patel, A.C., Cella, M., Gilfilan, S., Colonna, M., Kober, D.L.*, et al.* (2015). TREM-2 promotes macrophage survival and lung disease after respiratory viral infection. J Exp Med *212*, 681-697.

Xiong, X., Kuang, H., Ansari, S., Liu, T., Gong, J., Wang, S., Zhao, X.Y., Ji, Y., Li, C., Guo, L.*, et al.* (2019). Landscape of Intercellular Crosstalk in Healthy and NASH Liver Revealed by Single-Cell Secretome Gene Analysis. Mol Cell *75*, 644-660 e645.

Xu, H., Barnes, G.T., Yang, Q., Tan, G., Yang, D., Chou, C.J., Sole, J., Nichols, A., Ross, J.S., Tartaglia, L.A.*, et al.* (2003). Chronic inflammation in fat plays a crucial role in the development of obesity-related insulin resistance. J Clin Invest *112*, 1821-1830.

Zhang, Q., He, Y., Luo, N., Patel, S.J., Han, Y., Gao, R., Modak, M., Carotta, S., Haslinger, C., Kind, D.*, et al.* (2019). Landscape and Dynamics of Single Immune Cells in Hepatocellular Carcinoma. Cell *179*, 829-845 e820.

Zheng, C., Zheng, L., Yoo, J.K., Guo, H., Zhang, Y., Guo, X., Kang, B., Hu, R., Huang, J.Y., Zhang, Q.*, et al.* (2017). Landscape of Infiltrating T Cells in Liver Cancer Revealed by Single-Cell Sequencing. Cell *169*, 1342-1356 e1316.

Zheng, H., Pomyen, Y., Hernandez, M.O., Li, C., Livak, F., Tang, W., Dang, H., Greten, T.F., Davis, J.L., Zhao, Y.*, et al.* (2018). Single-cell analysis reveals cancer stem cell heterogeneity in hepatocellular carcinoma. Hepatology *68*, 127-140.

Zhou, Y., Song, W.M., Andhey, P.S., Swain, A., Levy, T., Miller, K.R., Poliani, P.L., Cominelli, M., Grover, S., Gilfillan, S.*, et al.* (2020). Human and mouse single-nucleus transcriptomics reveal TREM2-dependent and TREM2-independent cellular responses in Alzheimer's disease. Nat Med *26*, 131-142.

# Chapter 2
## Landscape of Intercellular Crosstalk in Healthy and NASH Liver Revealed by Single-Cell Secretome Gene Analysis

Adapted from:

## Abstract

Cell-cell communication via ligand-receptor signaling is a fundamental feature of complex organs. In addition to hepatocytes, the mammalian liver harbors diverse non-parenchymal cells (NPC) that are important for homeostasis and diseases such as nonalcoholic steatohepatitis (NASH). Despite this, the global landscape of intercellular signaling in the liver has not been comprehensively elucidated. Here we perform single-cell RNA sequencing and secretome gene analysis on liver NPC isolated from healthy and diet-induced NASH mice. Our study revealed highly restricted ligand and receptor gene expression at the single-cell level and a network of paracrine and autocrine signaling. Single-cell transcriptomic analysis revealed heterogeneity of liver endothelial cells and disruptions of the vascular signaling network during NASH pathogenesis. We uncovered the emergence of NASH-associated macrophages (NAM), which are marked by high expression of Triggering Receptor Expressed on Myeloid Cells 2 (Trem2), as a feature of mouse and human NASH that is strongly linked to disease progression and highly

responsive to pharmacological and dietary interventions. Finally, hepatic stellate cells (HSC) serve as a hub of intrahepatic signaling via HSC-derived stellakines, their responsiveness to vasoactive hormones and an IL11-mediated autocrine regulatory loop. These results provide unprecedented insights into the landscape of intercellular crosstalk and reprogramming of mammalian liver cells in health and disease.

## Introduction

The liver is the largest organ in the body that serves vital functions in nutrient and energy metabolism. Hepatocytes account for approximately 60% of the total cell population in human liver with non-parenchymal cells (NPC) constituting the rest, including liver sinusoidal endothelial cells (LSEC), the resident macrophage Kupffer cells (KC), hepatic stellate cells (HSC), cholangiocytes and diverse immune cell types (Friedman, 2008; Krenkel and Tacke, 2017; Poisson et al., 2017; Robinson et al., 2016; Tabibian et al., 2013). Dysregulations of hepatic metabolism contribute to the pathogenesis of type 2 diabetes, dyslipidemia and nonalcoholic fatty liver disease (NAFLD). NAFLD is characterized by excess fat accumulation in the liver and is strongly associated with obesity and metabolic syndrome. It has been estimated that approximately 25-30% of the adult population in the U.S. develops NAFLD, which may progress into nonalcoholic steatohepatitis (NASH), a more severe form of NAFLD that is characterized by chronic liver injury, fibrosis and inflammation (Cohen et al., 2011; Diehl and Day, 2017; Samuel and Shulman, 2018). NASH is emerging as a major cause of end-stage liver diseases, such as cirrhosis and hepatocellular carcinoma, and as a leading indication for liver transplantation (Diehl and Day, 2017; Pais et al., 2016).

Numerous ligand-receptor signaling modalities have been delineated among the cells in the liver that illustrate a critical role of intrahepatic crosstalk in tissue homeostasis and injury response (Friedman, 2008; Krenkel and Tacke, 2017). In addition, hepatokines are emerging as important regulators of nutrient metabolism and energy balance by acting on the central nervous system and other peripheral tissues (Meex and Watt, 2017; Wang et al., 2019). Despite these, the repertoire of secreted ligands and membrane receptors and the global landscape of intercellular signaling among liver cells have not been mapped at the single-cell resolution. Further, the

emergent nature of liver cell heterogeneity and reprogramming of intrahepatic paracrine crosstalk during NASH pathogenesis remain poorly understood.

Single-cell RNA sequencing (scRNA-seq) has emerged as a powerful tool to deconstruct the transcriptomes of complex tissues at the single-cell level (Gawad et al., 2016; Tanay and Regev, 2017). The advent of high-throughput single-cell profiling technologies provides a foundation for the Human Cell Atlas Project, an ambitious effort to define the molecular states of all human cell types in the body (Regev et al., 2017). Recent single-cell transcriptomic analysis of mouse tissues has revealed unprecedented molecular details on cellular heterogeneity (Han et al., 2018; Tabula Muris et al., 2018). In the liver, hepatocytes assume remarkably heterogeneous transcriptomic signatures that underlie zonation of diverse liver metabolic functions (Halpern et al., 2017). In this study, we performed single-cell RNA-seq and secretome analysis to dissect intercellular crosstalk in healthy and diet-induced NASH mouse livers. Our analyses revealed the landscape of intercellular crosstalk in mammalian liver and illustrated the complexity and richness of cell-cell signaling in liver physiology and disease. In addition, we uncovered the emergence of NASH-associated macrophages as a hallmark of mouse and human NASH that is strongly linked to disease progression and highly responsive to therapeutic interventions.

**Methods**

Mice

All animal studies were performed following procedures approved by the Institutional Animal Care & Use Committee at the University of Michigan. Mice were housed in pathogen-free facilities under 12-h light-dark cycles with free access to food and water. For standard chow feeding, mice were fed Teklad 5001 Laboratory Diet. For AMLN diet-induced NASH, C57/Bl6 mice were fed a diet containing 40% fat (of which 18% was trans-fat), 22% fructose, and 2% cholesterol (D09100301, Research Diets Inc.) for 20 weeks, as previously described (Clapper et al., 2013; Guo et al., 2017). In a separate diet-induced NASH model, C57/Bl6 mice were maintained on Choline-Deficient, Amino acid-defined HFD (45 kcal% fat) containing 0.1% methionine (CDAHFD, A06071309, Research Diets Inc.) for 6 weeks. In Elafibranor treated groups, C57/Bl6 mice were placed on CDAHFD and gavaged daily with 10mg Elafibranor/kg body weight in 1% CMC or vehicle for 24 days.

RNA extraction and analysis

Total RNA was extracted from frozen livers or harvested cell using Trizol (Alkali Scientific, TRZ-100). Quantitative RT-PCR gene expression analysis was performed as previously described (Guo et al., 2017; Wang et al., 2014). Liver RNA sequencing was performed using Illumina HiSeq 4000 at the University of Michigan DNA Sequencing Core.

Quantitative proteomic analysis

TMT experiments were performed as previously described (Zhao et al., 2017). Briefly, proteins were extracted from three pairs of chow and AMLN livers, reduced with 2 mM DTT for 10 min and alkylated with 50 mM iodoacetamide for 30 min in dark. Proteins were digested by Lys-C (Wako, at a 1:100 enzyme/protein ratio) for 2 hrs at RT followed by overnight digestion with trypsin (Thermo Fisher Scientific, at 1:100 enzyme/protein ratio). Peptides were desalted with Oasis HLB cartridges (Waters), resuspended in 200 mM HEPES (pH 8.5) to a final concentration of 1 □g/□L, and labeled with amine-based TMT six-plex reagents (Thermo Fisher Scientific). Three replicate samples were prepared for the control samples (TMT-126, -127 and -128), and the NASH samples (TMT-129, -130 and -131), respectively.

Samples were desalted and fractioned by bRPLC (basic pH reversed phase HPLC) on a ZORBAX 300 Extend-C18 column (Narrow Bore RR 2.1mm x 100 mm, 3.5 μm particle size, 300 Å pore size). Seventeen fractions were collected, which were lyophilized, desalted and analyzed by LC-MS/MS on a Thermo Orbitrap Elite mass spectrometer using a top 15 HCD method. MS/MS spectra were searched against a composite database of the mouse UniProt protein database and its reversed complement using the Sequest (Rev28) algorithm. Search parameters allowed for a static modification of 57.02146 Da on cystine (Carbamidomethyl), a variable modification of 15.994915 Da on methionine (oxidation), and a static modification of TMT labels (229.16293 Da) on peptide N-terminus and lysine. For TMT quantification, a 0.03 Th window was scanned around the theoretical m/z of each reporter ion (126:126.127725; 127:127.124760; 128:128.134433; 129:129.131468; 130:130.141141; 131:131.138176). The maximum intensity of each reporter ion was extracted, which was converted to signal-to-noise (S/N) ratios.

Isolation and scRNA-seq analysis of liver NPC

Liver NPC were isolated following a two-step protocol of pronase/collagenase digestion (Mederacke et al., 2015). Briefly, the liver was perfused in situ with calcium-free Hank's Balanced Salt Solution (HBSS) containing 0.2mg/ml EDTA, followed by sequential perfusion with 0.4mg/ml pronase (Sigma, P5147) and 0.2% collagenase type II (Worthington, LS004196). The liver was minced and further digested with HBSS containing 0.2% collagenase type II, 0.4 mg/ml pronase and 0.1mg/ml DNase I (Roche, R104159001) in 37 °C water bath with shaking for 20 min. Digestion was terminated with DMEM containing 10% serum. The resulting liver cell suspension was centrifuged at 50g for 3 min to remove hepatocytes and passed through 30μm nylon cell strainer followed by treatment with 0.8% NH4Cl to lyse red blood cells. This NPC suspension was centrifuged, resuspended in HBSS, and subjected to density gradient centrifugation using 20% Optiprep (Axis Shield, 1114542) to remove dead cells. Cell viability was confirmed by trypan blue exclusion. The resulting NPC were subjected to scRNA-seq analysis using 10X Genomics Chromium Single-Cell 3′ according to the manufacturer's instructions.

Data analysis

For total liver and LSEC RNA-seq, sequence reads were mapped to mouse genome mm10 using STAR. HTSeq was used to count the sequences that can be mapped to gene features. The raw read counts were normalized and processed for differential expression gene analysis using DESeq2. The significant expressed genes were determined by FDR less than 0.05. All RNA-seq data generated in this work have been deposited into the Gene Expression Omnibus (GEO) database (GSE119340, GSE129516).

For scRNA-seq, a total of 39,575 single cell NPC isolated from three chow and three NASH mice were processed using 10X Genomics CHROMIUM Single Cell 3' Solution. The libraries were sequenced using Illumina NextSeq High-Output, HiSeq 4000 and NovaSeq. We obtained a total of over 1.7 billion reads with an average of 43,122 reads per cell. Approximately 55.4% of the sequence reads can be confidently mapped to the mouse transcriptome. Seurat package (version 2.3.4) was used to analyze single cell RNA-seq data (Butler et al., 2018). After removing doublets and cells with low quality, 33,168 cells that expressed more than 500 genes

and 19,349 genes with transcripts detected in more than 3 cells were used for further analysis. Unique sequencing reads for each gene were normalized to total Unique Molecular Identifiers (UMIs) in each cell to obtain normalized UMI values. The top 1,000 highly variable genes were used for canonical correlation analysis (CCA) implemented in Seurat. Unsupervised clustering was applied after aligning the top 25 dimensions resulted from the CCA using a resolution of 0.07. The identity for each cluster was assigned based on the prior knowledge of marker genes. A higher resolution parameter was applied for sub-clustering of the endothelial and myeloid clusters. The t-SNE plots, violin plots, bar plots, circular plot, bubble plots, feature plots and heatmaps were generated by R and Java TreeView. Dot plot was generated using GraphPad.

Mouse secretome and network visualization

The mouse secretome database was compiled using gene lists obtained from Secreted Protein Database (SPD: http://spd.cbi.pku.edu.cn) (Chen et al., 2005) and IUPHAR database (http://www.iuphar-db.org/index.jsp), and manually curated to improve accuracy of gene annotation. Members of the solute carrier protein superfamily were not included in the current version. The secretome genes with normalized UMI values > 1.0 in any of the liver cell clusters were selected for construction of intrahepatic ligand-receptor signaling network. Ligand and receptor pairing dataset was obtained from Fantom5 (http://fantom.gsc.riken.jp), as recently described (Ramilowski et al., 2015). Network connectivity was visualized using Gephi graph tool (https://gephi.org).

LSEC RNA sequencing

LSEC were isolated from chow and AMLN mouse livers as previously described (Meyer et al., 2016). A combination of negative depletion with CD11b magnetic beads followed by positive-selection with CD146 magnetic beads was used to isolate LSEC from liver NPC suspension. Total RNA was isolated from purified LSEC for RNA sequencing (Beijing Genomics Institute, China). Twenty million reads were obtained using a paired-end 50bp module on BGISeq-500.

Flow cytometry

Flow cytometry analysis of sinusoidal endothelial cells was performed as we previously described (Ji et al., 2014; Ji et al., 2012). Briefly, hepatic NPC were collected as previously

described. The isolated cells were centrifuged at 1,000 rpm for 5 min. The cells were washed and re-suspended in cold staining buffer, followed by incubation with anti-CD16/CD32 antibody to block Fc receptors. For hepatic macrophages, liver samples were filtered through 100 um strainers in 1% BSA in PBS and centrifuged at 50x g for 3 minutes to remove hepatocytes. NPC were harvested as intermediate fraction following gradient centrifugation in 25% optiprep at 1500x g for 20 minutes. After wash, 1 x 106 cells were incubated with 100 □l of various antibodies diluted at optimal concentrations for 20 min at 4 °C. The fluorochrome-conjugated antibodies against CD45 (30-F1; Biolegend, 103130), CD146 (ME-9F1; Biolegend, 134711), CD36 (HM36; Biolegend, 102605), CD45 (I3/2.3; Biolegend, 147716), F4/80 (BM8; Biolegend, 123114), CD11b (M1/80; Biolegend, 101226), CD9 (MZ3; Biolegend, 124805), GPNMB (CSTREVL; Thermo Fisher, 50-5708-82), and CXCL9 (MIG-2F5.5; Biolegend, 515603), avidin-PerCP(Biolegend, 103130) were used. LSEC were gated as CD45-CD146+ cells, liver macrophages were gated as CD45+F4/80hiCD11bint or CD45+F4/80intCD11bhi for KC or MDM, respectively. For intracellular staining, the cells were fixed and permeabilized by BD Cytofix/Cytoperm Fixation/Permeabilization Kit per manufacturer's protocol. Samples were analyzed using BD LSR cell analyzer at the Vision Research Core Facility at the University of Michigan Medical School. Data were analyzed using the CellQuest software (BD Biosciences) and Flowjo (Flowjo.com).

Primary HSC isolation and cell lines

Mouse HSC were isolated from mouse livers by pronase/collagenase digestion followed by gradient centrifugation, as recently described (Mederacke et al., 2015). Briefly, NPC suspension was placed at the bottom of a four-layer OptiPrep gradient (1.034, 1.043, 1.058 and 1.085g/ml) and centrifuged at 1,500g for 30 min with the brake off. HSC were collected from the interface between two top layers (1.034 and 1.043g/ml) and cultured in DMEM containing 20% fetal bovine serum (FBS). Human HSC were purchased from ScienCell Research Laboratories and maintained in commercial HSC medium (ScienCell Research Laboratories, #5301). For immortalization of mouse HSC, isolated primary HSC were transduced with a recombinant retroviral vector expressing SV40 large T-antigen, followed by selection with G418. Immortalized HSC were maintained in DMEM containing 10% FBS.

Calcium imaging

The HSC cultures used for intracellular calcium imaging were within five passages following isolation. For calcium imaging, cells were seeded on cover glasses 2 days before loading with calcium indicator FURA-2AM (Thermo Fisher, F1201) and imaged with an inverted fluorescent microscope. Images were acquired every other second to monitor the dynamic changes in intracellular calcium levels in response to 100 nM ET-1 or Ang II alone or in combination with 100 nM PACAP.

Macrophage polarization index (MPI)

Macrophage polarization index was generated based on scRNA-seq profiles of polarized bone marrow-derived macrophages following LPS/cytokine stimulation (Li et al., 2019). Comparing M1 (LPS+IFNγ stimulation) and M2 (IL4+IL13 stimulation) profiles, gene with most significant changes were selected to calculate similarities of each cells to the whole population of M1 or M2 states. A linear regression line of all scRNA-seq profiles was generated and terms as "polarization axis" (https://macspectrum.uconn.edu). The projection of each cell on this axis was indexed as macrophage polarization index (MPI): higher MPI suggesting more "M1-like" (more inflammatory) states with lower MPI suggesting more "M2-like" (less inflammatory) states.

Immunofluorescence staining

Liver tissues were fixed in situ with 4% paraformaldehyde, incubated with 30% sucrose in PBS overnight, and embedded in OCT. Frozen sections were permeabilized with 0.3% Triton X-100 in PBS and then blocked in 5% BSA, followed by incubation in primary antibody solution overnight at 4 °C, and subsequently in secondary antibody solution at room temperature for one hour. Sections were mounted in VECTASHIELD Antifade Mounting Medium (Vector Laboratories, H-1000). Images were taken with Olympus fluorescence microscope.

Western Blot Analysis

Total liver protein extracts and cell lysates were prepared using a lysis buffer containing 50 mM Tris-HCl (pH = 7.5), 137 mM NaCl, 1 mM EDTA, 1% Triton X-100, 10% glycerol, 10 mM NaF, 10 mM Na4P2O7, 1 mM Na3VO4, and protease inhibitor cocktail. The lysates were

separated by SDS-PAGE and transferred to a PVDF membrane, followed by immunoblotting with primary antibodies and secondary antibodies.

Human NASH study

The study population consisted of 144 Mexican mestizo subjects (male and female) who underwent bariatric surgery for morbid obesity. A total of 82.6% were female and the mean age of the participants was $38.6 \pm 10.1$ years. Detailed characteristics of the study have been reported elsewhere (Gutierrez-Vidal et al., 2015; Leon-Mimila et al., 2015; Vega-Badillo et al., 2016). Liver biopsies were collected in RNAlater (Sigma, St. Louis, MO) during surgery and processed for RNA sequencing analyses as describe previously (Hui et al., 2018). This study was performed according to the principles of the Declaration of Helsinki and was approved by the institutional review boards of the National Institute of Genomic Medicine (Mexico) and the Hospital Dr. General Ruben Leñero. All participants provided written informed consent prior to their inclusion. Correlations of normalized values of RNA sequencing data with transaminase levels, steatosis, ballooning, inflammation and NAS score were evaluated using partial correlations adjusting for batch, age, sex, BMI and T2D status. The differences between groups were evaluated using ANCOVA adjusting for batch, age, sex, BMI and T2D status. Because transaminase levels were not normally distributed, the values were log transformed before performing statistical analyses.

**Results**

*RNA-seq and quantitative proteomic analyses of healthy and NASH mouse livers*

Previous studies have established a diet-induced mouse NASH model (Amylin diet, AMLN diet) that faithfully recapitulates key features of human NASH (Clapper et al., 2013; Guo et al., 2017; Xiong et al., 2019). To explore the pathogenic mechanisms underlying NASH progression, we performed RNA-sequencing (RNA-seq) analysis on the livers from mice fed standard chow or AMLN diet for 20 weeks. We detected 311 and 461 genes that exhibited more than 2-fold decrease or increase in mRNA expression, respectively (Figure 1A and Table S1). Many of these NASH-induced genes were also elevated in the livers from a cohort of human NASH patients, compared to non-NASH individuals (Figure 1B). In parallel, we performed quantitative proteomic analysis and compared mRNA and protein expression in chow and AMLN diet-

induced NASH livers. We observed remarkable concordance between RNA-seq and proteomic data (Figure 1C and S1A). As such, most of the NASH-induced genes revealed by RNA-seq exhibited increased protein expression, whereas downregulated genes were associated with reduced protein expression. Gene ontology analysis on these two differentially regulated gene sets revealed that the expression of genes involved in lipid metabolism and oxidative reactions was suppressed following diet-induced NASH in mice (Figure 1A). In contrast, NASH-induced genes were highly enriched for the pathways responsible for extracellular matrix (ECM) remodeling (Col1a1, Mmp12), cell adhesion, phagocytosis, and immune response (Ccr2, H2-ab1, Lcn2), core biological functions of liver NPC. These observations underscore a potentially important role of liver NPC in driving NASH pathogenesis.

*Single-cell RNA sequencing analysis of liver NPC*

To elucidate liver cell heterogeneity and their dynamic changes during NASH pathogenesis, we performed single-cell RNA sequencing (scRNA-seq) on liver NPC isolated from mice fed chow or AMLN diet. We obtained a total of 33,168 single-cell transcriptomes (17,788 chow; 15,380 NASH) from three pairs of mice. Compared to a recent hepatocyte scRNA-seq study illustrating metabolic zonation in the liver (Halpern et al., 2017), the coverage of the NPC population was vastly expanded in our dataset. T-distributed Stochastic Neighbor Embedding (t-SNE) visualization of the combined chow and NASH data revealed ten major clusters, which correspond to endothelial cells, macrophages, T cells, B cells, cholangiocytes, plasma B cells, dendritic cells (DC), HSC, hepatocytes, and a cluster representing dividing cells, based on marker gene expression (Figure 1D-F and Table S2). We examined the extent to which liver cell transcriptomes are conserved among species by integrating our dataset with a recent scRNA-seq study of human livers (MacParland et al., 2018). Correlation analysis indicated that major liver cell types displayed highly conserved transcriptomic signature and shared common sets of marker genes in mice and humans (Figure 1G and S1B).

All ten clusters contained cells derived from both chow and NASH mouse livers (Figure 1H and S1C-D). We observed that NASH livers accounted for over 77% of the cells in the macrophage cluster whereas chow endothelial cells disproportionally contributed to the endothelial cluster. The construction of single-cell transcriptome maps for different liver cell types allows us to

assign likely cellular sources for the genes differentially expressed in NASH (Figure 1A). Remarkably, genes most specific to macrophage and HSC clusters were primarily NASH-induced genes in the liver (Figure 1I). In contrast, most of the hepatocyte-enriched genes were downregulated in NASH livers. These observations strongly suggest that NASH pathogenesis is linked to cell type-specific reprogramming of the liver cell transcriptomes.

*Single-cell analysis of secretome and receptor gene expression in the liver*
Intercellular crosstalk via ligand and receptor signaling has been recognized to be a fundamental aspect of organ biology. Despite this, the repertoire of secreted ligands and membrane receptors and the global landscape of intercellular signaling among liver cells have not been mapped at the single-cell resolution. We next analyzed secretome gene expression in the liver cells to identify the cellular origins of ligands and receptors. We manually curated the mouse secretome gene list compiled from several available datasets (Wang et al., 2014). This list contained 1,272 and 755 genes that are predicted to encode secreted proteins and membrane receptors, respectively (Table S3). Among these, 305 secreted factors and 147 receptors had readily detectable mRNA expression (normalized UMI>1.0) in our scRNA-seq dataset (Table S4). Clustering analysis of the liver secretome genes revealed remarkably cell type-specific patterns of receptor and ligand gene expression (Figure 2A). For example, Kdr and Tek, which encode receptor tyrosine kinases important for vascular development and maintenance, were enriched in the endothelial cluster, whereas Csf1r is abundantly expressed in the macrophage cluster. Ccl5 and Spp1 marked the T cell and cholangiocyte clusters, respectively. Col1a1 and Dcn were abundantly expressed in HSC while Cd79b marked the B cell cluster (Figure 2b). Comparative analysis of secretome gene expression in mouse and human single-cell datasets revealed a highly conserved pattern of distribution among different liver cell types across species (Figure 2C and S2A). These results demonstrate that, compared to whole liver transcriptome analysis, scRNA-seq provides unparalleled sensitivity and accuracy in mapping ligand and receptor gene expression to specific cell types in the liver.

The notably restricted patterns of ligand and receptor expression illustrate potentially highly specific paracrine and autocrine connectivity in the mammalian liver. We next integrated our scRNA-seq data with a ligand-receptor interaction database (Ramilowski et al., 2015) to

construct an intercellular signaling map among the liver cells. We identified the HSC, endothelial and macrophage clusters as prominent hubs for paracrine and autocrine signaling (Figure 2D and S2B). A subset of ligands and receptors remained orphan and lacked their cognate partners in this network, reflecting their potential role in inter-tissue endocrine crosstalk. We next analyzed how NASH alters secretome gene expression in the liver. Not surprisingly, mRNA and protein expression for the secretome gene set were highly correlated (Figure 2E). Remarkably, many genes encoding HSC and macrophage-enriched secreted factors and membrane receptors exhibited increased expression at both mRNA and protein levels, whereas hepatocyte-enriched genes lacked this pattern of regulation. Together, this secretome gene analysis revealed a global landscape of ligand and receptor gene expression, connectivity and alterations in NASH at single-cell resolution.

*Vascular signaling and its dysregulation during NASH pathogenesis*

Endothelial cells represent the largest cluster within the NPC population, containing a total of 10,447 cells. At higher t-SNE resolution, this cluster can be further divided into four subclusters, representing periportal (Endo-pp) and pericentral (Endo-pc) endothelial cells and two clusters of liver sinusoidal endothelial cells (LSEC-1 and LSEC-2) that line the surface of liver sinusoids (Figure 3A). Clustering analysis of these four endothelial subtypes revealed unique transcriptomic signatures (Figure 3B-C and Table S5). Based on single molecule fluorescence in situ hybridization results reported in a recent study on liver endothelial zonation (Halpern et al., 2018), we identified a set of genes exhibiting Endo-pc enriched expression including Wnt9b, Rspo3, Cdh13 and Wnt2. Endo-pp expressed high levels of Ednrb, Jag1, Lrg1, Efnb1, Ltbp4 and Adgrg6, whereas LSEC-1 and LSEC-2 were marked by abundant expression of Fcgr2b and Gpr182, known LSEC markers (Poisson et al., 2017). While the LSEC transcriptomes appeared similar overall, a subset of genes exhibited enriched expression in a cluster-specific manner. These results support the notion of liver endothelial zonation and functional specialization in a manner resembling zonation of hepatocytes in the liver (Halpern et al., 2017).

To explore how NASH alters liver endothelial function, we analyzed chow and NASH endothelial transcriptomes in the scRNA-seq dataset and performed RNA-seq on LSEC isolated from chow and AMLN diet-fed mouse livers. The scRNA-seq and total RNA-seq datasets

obtained for endothelial cells were remarkably consistent (Figure 3D). Compared to control, endothelial cells derived from NASH livers exhibited increased expression of genes involved in lipid metabolism, antigen presentation and chemokine release. In contrast, significant downregulation of genes involved in vascular development and homeostasis was observed in NASH liver. These NASH-induced alterations of gene expression appeared to occur in all four endothelial subclusters (Figure S3A-B). We further confirmed these findings using flow cytometry and observed that endothelial cell expression of Cxcl9 and BODIPY staining, a marker for cellular lipid accumulation, were strongly increased in LSEC isolated from NASH mouse livers (Figure 3E). This reprogramming of the endothelial transcriptome was linked to a profound disruption of the sinusoidal capillaries in the liver during diet-induced NASH (Figure 3F). Immunofluorescence staining of LSEC using polyclonal FCGR2B antibodies indicated that NASH mice had apparently lower abundance and altered histological integrity of the liver sinusoids.

As shown above, endothelial cells express a large number of membrane receptors and adhesion proteins and also secrete a number of angiocrine factors. Analysis of the endothelial secretome revealed that this cluster exhibited abundant expression of many membrane receptors for ligands important for vascular development and homeostasis, including Notch1, VEGF receptors (Kdr, Flt1, Flt4, Nrp1, Nrp2), TGF β receptors (Tgfbr2, Tgfbr3, Bmpr2, Eng), Ephrin B receptor (Ephb4), and receptor tyrosine kinase (Tek, Tie1) and phosphatase (Ptprb) signaling pathways (Figure 3G). To delineate the paracrine and/or autocrine signaling network that acts on liver endothelial cells, we analyzed scRNA-seq data to identify the cellular sources of the putative ligands for these receptors. Remarkably, several ligands within this paracrine network were found to originate from the HSC, endothelial and cholangiocyte clusters. Dll4, a ligand for Notch1, Bmp2 and Efnb2 were highly expressed by endothelial cells and therefore considered angiocrine factors (Rafii et al., 2016), whereas Gdf2, Gdf10 and Bmp5 secretion appears to be restricted to HSC. Vegfa expression was most abundantly expressed by cholangiocytes. Comparative analysis of mouse and human scRNA-seq datasets revealed that the cellular sources of these ligands were highly conserved in these two species (Figure S3C).

The endothelial cluster exhibited abundant expression of several GPCRs (Calcrl, Ramp2, Gpr182), adhesion GPCRs (Adgrf5, Adgrl4), and cytokine receptors (Il6st, Lifr) (Figure 3G). Calcrl and Ramp2 form a receptor complex for adrenomedullin, a peptide hormone that exerts pleiotropic effects on endothelial cells (Geven et al., 2018), suggesting that hepatic vascular system may be highly responsive to vasoactive endocrine hormones. Notably, mRNA expression of endothelial receptors and angiocrine factors, ligands secreted by endothelial cells, was significantly downregulated during diet-induced NASH (Figure 3H). To determine whether the disruptions of liver vascular function also occur during human NASH pathogenesis, we analyzed a published microarray dataset containing samples from 24 healthy, 20 NAFLD, and 19 NASH patients (GSE89632) (Arendt et al., 2015). Similar to mouse NASH, transcript abundance for CXCL9 and FABP4 was significantly increased in human NASH livers (Figure 3I). Compared to healthy control, the expression of BMP2, NRP1 and VEGFA was downregulated in the livers from NAFLD and NASH patients. These results illustrate profound disruptions of vascular and angiocrine signaling during NASH pathogenesis that is conserved in mice and humans.

*Emergence of NASH-associated macrophage and its molecular signature*

A prominent feature of the macrophage cluster is its marked expansion during diet-induced NASH (Figure 4A). This cluster can be further divided into two groups of cells representing Kupffer cells and monocyte-derived macrophages (MDM) based on their marker gene expression profile (Figure 4B). KCs were characterized by high expression of Adgre1 (encoding F4/80) and Clec4f, whereas MDM exhibited high expression of Itgam (Cd11b) and Ccr2, a chemokine receptor important for infiltration of circulating monocytes (Krenkel and Tacke, 2017). In contrast, Csf1r expression was observed in both KC and MDM subclusters. We compared our scRNA-seq data with a public microarray dataset on sorted KCs and MDMs (GSE98782) (Krenkel et al., 2018). We observed a remarkable concordance of gene expression profile using these two methods (Figure S4A), illustrating high accuracy of transcriptomic analysis based on scRNA-seq data. Clustering analysis indicated that both KC and MDM transcriptomes were altered following diet-induced NASH (Figure S4B). To determine how NASH alters the functional properties of liver macrophage populations, we developed a method to quantitatively evaluate macrophage polarization based on their gene expression signatures at the single cell level (Li et al., 2019). Here, a higher macrophage polarization index (MPI) reflects

a more proinflammatory phenotype. This analysis indicated that KCs and MDMs from NASH livers exhibited a notable shift towards a proinflammatory phenotype (Figure 4C), consistent with induction of a proinflammatory environment during NASH pathogenesis.

We next analyzed macrophage heterogeneity and observed two KC populations marked by low and high Trem2 mRNA expression (Trem2lo and Trem2hi, respectively). Trem2 is a scavenger receptor required for phagocytosis and clearance of apoptotic cells and has been implicated in several disease conditions, including Alzheimer's disease and liver injury (Deczkowska et al., 2018; Perugorria et al., 2018). Remarkably, while both chow and NASH livers harbored Trem2lo KC, over 93% of Trem2hi KC were derived from NASH livers, indicating that this is a unique population of macrophages associated with NASH pathogenesis (Figure 4D). As such, we termed this Trem2hi KC population "NASH-associated macrophages" (NAM). In addition to Trem2, NAM also exhibited abundant expression of Gpnmb and Cd9, all of which were induced during NASH (Figure 4E). Importantly, hepatic Trem2 and Gpnmb mRNA expression was strongly associated with liver injury and fibrosis in a cohort of mice with varying NASH severity (Xiong et al., 2019) (Figure 4F and S4C). To confirm the emergence of NAM during NASH pathogenesis, we performed flow cytometry using GPNMB and CD9 antibodies to detect this macrophage population (Figure 4G). Consistent with single-cell analysis, we observed a marked expansion of KC in NASH livers. While GPNMB+ CD9+ double positive KC were rarely detected in chow livers, they represented over 60% of KC obtained from NASH livers.

To further investigate the dynamic changes of liver macrophages during NASH pathogenesis, we performed studies in mice fed chow or CDAHFD, a choline-deficient, L-amino acid defined HFD that contains 0.1% methionine. This diet was recently shown to induce robust NASH pathologies in mice within six weeks (Matsumoto et al., 2013). As expected, CDAHFD feeding markedly elevated plasma ALT and AST levels, induced fibrotic and inflammatory gene expression and expanded macrophage population in the liver (Figure S5A-C). In addition, hepatic Trem2 and Gpnmb mRNA expression was drastically increased in the livers from mice fed CDAHFD. Flow cytometry analysis indicated that while GPNMB+ NAM were essentially absent in chow livers, this population represented over 70% of KC in the liver following CDAHFD-induced NASH (Figure 4H). GPNMB is a transmembrane protein and has been

41

shown to undergo cleavage to release the extracellular domain into circulation (van der Lienden et al., 2018). We performed ELISA to measure the concentrations of GPNMB in plasma from healthy and NASH mice. Plasma GPNMB levels were significantly elevated in both AMLN diet and CDAHFD-induced NASH (Figure 4I), suggesting that it may provide a potential biomarker for NASH.

The emergence of NASH-specific macrophages in the liver suggests that NAM may play an important role in the pathogenesis of disease. To examine the molecular properties of NAM, we binned chow and NASH KC (25 cells per bin) into respective Trem2-negative, Trem2-low, and Trem2-high subgroups (Figure 5A). We identified a cluster of genes exhibiting a high degree of correlation with Trem2 expression (Table S6). Gene ontology analysis indicated that Trem2-high macrophages had enriched expression for genes involved in endocytosis, lysosomal degradation, MHC class II antigen presentation and extracellular matrix remodeling. Macrophages express a large number of scavenger receptors including Trem2, which are responsible for the clearance of apoptotic cells and extracellular matrix during tissue injury. These results illustrate that liver resident macrophages undergo both marked expansion and functional reprogramming during NASH pathogenesis.

*Dynamic regulation of NAM in human NASH and during NASH resolution*
We next explored whether human NASH is associated with induction of NAM. Analysis of a microarray dataset indicated that TREM2 mRNA expression was increased in the livers from patients with hepatic steatosis and NASH (Figure 5B). We further examined the association between hepatic TREM2 gene expression and NASH parameters in an independent cohort of 144 NASH patients (Hui et al., 2018; Vega-Badillo et al., 2016). We observed a remarkable association between TREM2 expression and plasma markers of liver injury (Figure 5C). In addition, hepatic TREM2 expression was strongly associated with the severity of steatosis, inflammation, hepatocyte ballooning, liver fibrosis and NAFLD activity score (NAS) (Figure 5D). Hepatic GPNMB mRNA expression was also associated with these NASH pathologies (Figure S4D). These results indicate that the induction of NAM gene signature is a common feature of mouse and human NASH pathogenesis. Further, we have demonstrated the potential for using NAM markers as a diagnostic biomarker for NASH.

Key aspects of NASH pathologies are largely reversible in response to pharmacological and/or dietary interventions (Romero-Gomez et al., 2017). We next examined whether NASH reversal is linked to reduction of Trem2hi KC and attenuation of NAM gene signature in the liver. In the first set of studies, we treated mice fed CDAHFD with Elafibranor, a dual agonist for PPAR α and PPARδ that has been shown to be effective in reversing NASH pathologies in mice (Staels et al., 2013). Compared to vehicle, Elafibranor treatment potently lowered plasma AST and ALT levels and markedly reduced the abundance of NAM in the liver, as revealed by GPNMB flow cytometry (Figure 5E-F). Hepatic gene expression analysis indicated that Elafibranor stimulated mRNA expression of genes involved in fatty acid β -oxidation (Acadm, Acox1) while attenuating expression of Trem2, Gpnmb, Tnf and Col1a1 (Figure 5G). Consistently, hepatic GPNMB protein expression and plasma GPNMB levels were also reduced following Elafibranor treatments in mice fed CDAHFD (Figure 5H-I). We previously demonstrated that dietary switch from AMLN diet to chow for eight weeks resulted in marked improvements of NASH pathologies in mice (Xiong et al., 2019). In this model, we also observed significantly reduced expression of Trem2, Gpnmb and Cd9 following dietary switch (Figure 5J). Compared to AMLN group, plasma GPNMB concentrations were also lower following the AMLN to chow dietary switch (Figure 5K). These results demonstrate that NAM and their associated gene signature are highly responsive to pharmacological and dietary interventions that reverse NASH pathologies.

*The hepatic stellate cell ligand-receptor signaling network*
We obtained single-cell transcriptome data for a total of 272 cells in the HSC cluster. The HSC secretome was prominent in its diversity, containing 27 and 99 genes encoding membrane proteins and secreted factors, respectively (Table S7). As expected, a large number of proteins secreted by HSC correspond to the structural proteins of ECM including collagens and proteoglycans and those involved in ECM remodeling (Figure 6A). Analysis of liver RNA-seq data indicated that, compared to healthy control, expression of many of these genes was strongly increased in NASH livers, reflecting activation of the fibrosis gene program. We next constructed a ligand-receptor signaling network on the secretome genes exhibiting enriched expression in HSC, a unique set of secreted factors that we termed "stellakines" for their stellate cell origin. This analysis revealed that HSC secrete 21 stellakines that are predicted to act

primarily on endothelial and immune cells based on their receptor expression (Figure 6B). As such, mRNA expression of the receptors for WNT4, NTN1, EFNB1, BMP5, GDF2, GDF10 and SEMA3C was largely restricted to endothelial cells, while the cellular targets for CCL2, CCL11, CXCL10, CXCL12, CXCL16, CTGF and GAS6 were primarily immune cells, such as macrophage, DC, T and B cells. Whole liver RNA-seq analysis indicated that the expression of many of these HSC-derived ligands was elevated in NASH and associated with liver injury (Figure 6C and S6A), suggesting that increased stellakine secretion and action are linked to diet-induced NASH pathogenesis.

The HSC-enriched receptors (27) can be divided into three broad categories based on their known biological functions: ECM biology and fibrosis, cytokine signaling and vasoactive receptors (Figure 6D). A number of HSC receptors have been implicated in liver fibrosis, including Pdgfrb, Fgfr2, Ddr2, Ryk and Lrp1. For example, Discoidin domain receptor 2 (Ddr2) serves as a non-integrin collagen receptor that regulates HSC activation, ECM deposition and liver fibrosis (Leitinger, 2014). Interestingly, mRNA expression of many of these HSC receptors was altered in NASH livers (Figure S6B). We observed restricted HSC expression of p75 neurotrophin receptor (Ngfr), which promotes HSC apoptosis in response to Nerve growth factor (NGF) (Trim et al., 2000). Importantly, our scRNA-seq analysis revealed cholangiocytes and HSC as two major sources of NGF, supporting a dual paracrine and autocrine mechanism in mediating NGF-induced HSC cell death. Together, these results demonstrate that HSC are uniquely equipped to respond to diverse extracellular signals and serve as a hub for intrahepatic signaling by secreting stellakines.

*Vasoactive hormone signaling in HSC*
HSC are known to harbor contractile apparatus and undergo contraction and relaxation to modulate liver sinusoidal blood flow (Friedman, 2008; Reynaert et al., 2008). We uncovered a surprisingly diverse set of vasoactive hormone-responsive receptors on HSC. Compared to other cell types, HSC exhibited enriched mRNA expression for Endothelin receptor type a (Ednra), Ednrb, Angiotensin II receptor type 1a (Agtr1a) and Adrenergic receptor α 2b (Adra2b), which promote HSC constriction upon activation (Reynaert et al., 2008). mRNA transcripts for several GPCRs targeted by vasorelaxation peptide hormones were also abundantly expressed by HSC,

including Ramp1, Calcrl, Pth1r and Vipr1. Ramp1 and Calcrl together form a receptor for Calcitonin gene-related peptide, a vasodilator, while PTH1R and VIPR1 are receptors for parathyroid hormone (PTH)/parathyroid hormone-related protein (PTHRP) and vasoactive intestinal peptide (VIP)/pituitary adenylate cyclase-activating peptide (PACAP), respectively. Importantly, HSC-enriched expression for Ednrb, Adra2b, Vipr1, Pth1r and Ramp1 was observed in both mice and humans (Figure 6E), illustrating likely functional conservation of vasoactive hormone signaling in HSC.

We confirmed VIPR1 protein expression in HSC using double immunofluorescence staining. As shown in Figure 6F, VIPR1-positive cells were also positive for Decorin (DCN), a collagen-binding protein produced by Desmin-positive HSC (Meyer et al., 1992). To confirm that these vasoactive receptors are functional in contractile signaling, we performed treatments on cultured mouse and human HSC. Activation of endothelin receptors and Agtr1a with their respective ligands (Endothelin 1, ET-1 and Angiotensin II, Ang II) triggered a rapid and robust increase of intracellular calcium levels in cultured primary mouse HSC (Figure 7A). Importantly, ET-1 and Ang II also potently stimulated the calcium response in primary human HSC (Figure 7B). The ability of ET-1 and Ang II to raise intracellular calcium was greatly diminished in the presence of PACAP, a physiological ligand of VIPR1 that promotes smooth muscle relaxation and gastrointestinal motility (Makhlouf and Murthy, 1997). Immunoblotting analysis using antibodies recognizing phosphorylated protein kinase A (p-PKA) substrates showed that PACAP induced robust PKA signaling, likely as a result of increased cAMP production in response to GPCR activation (Figure 7C and S6C). qPCR analysis revealed that hepatic Vipr1 mRNA expression was significantly reduced by NASH and negatively correlated with Col1a1 gene expression (Figure S6D-E). These functional studies demonstrate that HSC contraction and relaxation are likely balanced by the opposing action of physiological hormones. Surprisingly, we did not detect significant expression of Vip, Pacap, Pth and Pthrp transcripts in our scRNA-seq dataset, suggesting that their receptors likely respond to ligands of endocrine and/or neuroendocrine origins.

*Regulation of stellakine gene expression by autocrine IL11 signaling*

Expression of several receptors for the IL-6 family of cytokines was notable in the HSC cluster, including Lifr, Il11ra1 and Il6st; the latter encodes gp130, a signaling receptor shared by this family of cytokines (Sims and Walsh, 2010). Our analysis indicated that Il11ra1 mRNA expression was most abundant in HSC (Figure S7A). Il11ra1 encodes a co-receptor for IL11 and mediates IL11 signaling through gp130. To determine whether IL11 signaling may be altered during NASH, we analyzed hepatic Il11 mRNA expression in two models of diet-induced NASH. Interestingly, both AMLN diet and CDAHFD feeding robustly induced Il11 expression in mouse liver, coinciding with NASH pathogenesis (Figure 7D). We surveyed the source of Il11 expression and found that HSC displayed the highest mRNA expression among ten major liver cell types (Figure S7A). These results suggest that autocrine IL11 signaling may be augmented during NASH when HSC assume a more activated phenotype. In support of this, we found that TGF β strongly stimulated Il11 mRNA expression in immortalized mouse HSC (Figure 7E).

IL11 has been previously implicated in cardiac fibrosis (Obana et al., 2010; Schafer et al., 2017); however, its pathophysiological role and mechanism of action remain to be fully ascertained. To explore how IL11 signaling regulates HSC biology, we treated cultured mouse HSC with vehicle, TGF β or IL11 and analyzed expression of genes involved in fibrosis. As expected, TGF β treatment potently induced mRNA expression of Col1a1, Acta2 and Ctgf, known targets of TGF β signaling and HSC activation (Figure 7F). While IL11 robustly induced mRNA expression of Socs3, a target of cytokine signaling mediated by STAT3 activation, it failed to increase fibrosis gene expression in HSC. Instead, IL11 treatment stimulated the expression of a subset of stellakines including Cxcl1, Wnt4 and Ccl11, all of which exhibit increased expression in the liver in two models of diet-induced NASH (Figure 7G and S7B). The expression of Cxcl10 and Ntn1 remained largely unaltered in HSC treated with IL11, suggesting that they are likely regulated by other upstream signals. We next explored the signaling pathways that mediate IL11 induction of stellakine gene expression. IL11 treatment resulted in a rapid and robust increase in ERK and STAT3 phosphorylation (Figure 7H). Remarkably, inhibition of STAT3 activation by Stattic essentially abolished the induction of Cxcl1, Wnt4 and Ccl11 in response to IL11 (Figure 7I). In contrast, inhibition of ERK activation by U0126 failed to elicit similar effects. Together, these results illustrate a prominent role of autocrine IL11 signaling in HSC in the control of stellakine gene expression (Figure 7J).

46

**Discussion**

The mammalian tissues harbor diverse cell types that exhibit distinct molecular signatures and functional properties. While intercellular crosstalk has been recognized as a fundamental feature of tissue biology, the precise nature of these signaling modalities remains obscure due to limited cellular resolution of bulk transcriptomic and proteomic analyses. Using scRNA-seq based secretome analysis, we mapped the transcriptional landscape of secreted ligands and membrane receptors in major liver cell populations and constructed a ligand-receptor network that governs extensive autocrine and paracrine crosstalk in the liver. A notable advantage of single-cell transcriptome analysis is the unprecedented accuracy in delineating the cellular sources of secreted ligands and their potential target cell types. Beyond intrahepatic crosstalk via secreted factors, we observed abundant expression of endocrine and neuroendocrine receptors on liver NPC, such as endothelial cells and HSC, suggesting that extrahepatic ligands may serve an important role in shaping the biology of diverse cell types in the liver. Together, this work reveals a global map of secretome gene expression in the liver at single-cell resolution and provides a blueprint for deconstructing the dynamic nature of intercellular crosstalk in homeostasis and disease.

Comparative single-cell analysis of NPC from healthy and NASH livers revealed profound disruptions of the vascular and angiocrine signaling network. It is important to note that these disruptions of the cell-cell signaling network in the liver appear to be conserved pathophysiological features of NASH in both mice and humans. Unexpectedly, we observed a NASH-specific macrophage population that is marked by high levels of expression of Trem2. This unique hepatic macrophage population is analogous to the Trem2-positive microglial cells found in Alzheimer's Disease (Keren-Shaul et al., 2017), a neurodegenerative disorder causally linked to aberrant function of tissue-resident macrophages. To date, Trem2 mutations have been linked to Alzheimer's Disease, Nasu-Hakola disease, frontotemporal lobar degeneration, ALS and Parkinson's disease (Lill et al., 2015), suggesting Trem2 has a critical role in resident macrophage function in disease. While the precise mechanism through which Trem2 regulates disease pathogenesis in the brain remains poorly understood, several in vivo studies have begun to elucidate the importance of the Trem2-positive macrophage population. Of note, Trem2

deficiency in mice results in failure of microglia to proliferate and cluster around αβ plaques in a mouse model for Alzheimer's Disease (Wang et al., 2015). Overexpression of Trem2 in vitro has been found to increase microglial capacity for phagocytosis of apoptotic neurons and αβ plaques (Jiang et al., 2014). These findings strongly suggest a role for NAM in the clearance of apoptotic and lipid-laden hepatocytes in the NASH liver. In support of this, a recent study has shown that Trem2-deficient mice developed more severe immune-mediated liver injury (Perugorria et al., 2018). As such, the emergence of Trem2-positive macrophages likely serves an adaptive and protective role during diet-induced NASH.

A notable aspect of the HSC secretome is its dual role as a source of the ECM structural and remodeling proteins and diverse signaling ligands. The list of stellakines becomes even longer with a less stringent UMI cutoff, underscoring the prominent role of HSC as a signaling hub in the liver. Ligand receptor connectivity analysis of the stellakine signaling network highlights endothelial and immune cells as the primary cellular targets of stellakine action. These findings are consistent with the ability of HSC to engage immune cells and orchestrate tissue injury response and repair (Friedman, 2008). As expression of many stellakines is induced during NASH, it is likely that they may contribute to both adaptive and maladaptive HSC reprogramming in the context of chronic liver injury. The induction of stellakine expression is at least in part attributed to the IL11/IL11R α autocrine signaling loop driven by TGF β signaling in HSC. While the pathophysiological role of autocrine IL11 signaling remains unknown, our results strongly suggest that the dysregulations of stellakine secretion likely represent a key aspect of HSC biology during NASH pathogenesis.

A rather unexpected finding from the single-cell membrane receptor mapping is the identification of several GPCRs that respond to vasoactive hormones. For example, angiotensin and endothelin receptors are known to respond to Angiotensin and Endothelin 1, respectively, to trigger calcium response and contraction of smooth muscle cells. Similarly, activation of the α 2 adrenergic receptor promotes vasoconstriction. In contrast, several GPCRs responsive to vasorelaxing peptides including Pth1r, Vipr1, Ramp1, Ramp2 and Calcrl are also highly expressed on HSC. Importantly, our functional studies indicate that these vasoactive GPCRs are highly potent in triggering intracellular calcium responses, a prerequisite for cellular contractile

activities. These results strongly support the notion that HSC are capable of responding to diverse vasoactive hormones and likely play an important role in the control of intrahepatic vascular tone (Hellerbrand, 2013; Reynaert et al., 2008). Future work is needed to delineate the physiological role of vasoactive signaling in HSC in the control of hepatic blood flow and its potential contribution to the pathogenesis of portal hypertension.

While this work delineates the landscape of liver cell secretome gene expression and NASH-associated reprogramming, several key predictions require further functional validation. For example, it remains to be established whether hepatic vascular dysfunctions serve as a pathogenic factor that is causally linked to NASH progression. The emergence of TREM2-positive NAM in both mouse and human NASH is particularly intriguing. Future work is needed to establish the mechanisms underlying the induction of this unique macrophage population in NASH and how NAM contributes to tissue homeostasis in healthy and disease states. Finally, whether HSC functions as a gatekeeper of hepatic metabolism via the regulation of its contractility remains an important unanswered question. Nevertheless, our work provides strong support for the concept that non-parenchymal cell types in metabolic tissues play a more pervasive role in metabolic control and disease progression.

Author contributions

J.D.L., X.X., H.K. and J.L. conceived the project and designed research. X.X., H.K., X.Z., Y.J., J.G., Z.C., X.Z.X., L.G., S.L., L.Q., M.C. and K.K. performed the experiments and analyzed the

data. J.O. and R.L. performed scRNA-seq using the 10X Genomics platform. T.L., S.A. and J.D.L. performed sequencing data analyses. C.L. and B.Z. performed macrophage polarization analysis. F.C.P. and H.V.R. performed human sample collection and characterization. S.C.Q. performed genetic and biochemical characterization. A.J.L. and A.H.V. performed RNA-seq in human liver samples. P.L.M. performed statistical analyses of the human cohort.

Competing interests

The authors declare no competing interests.

**Figures**
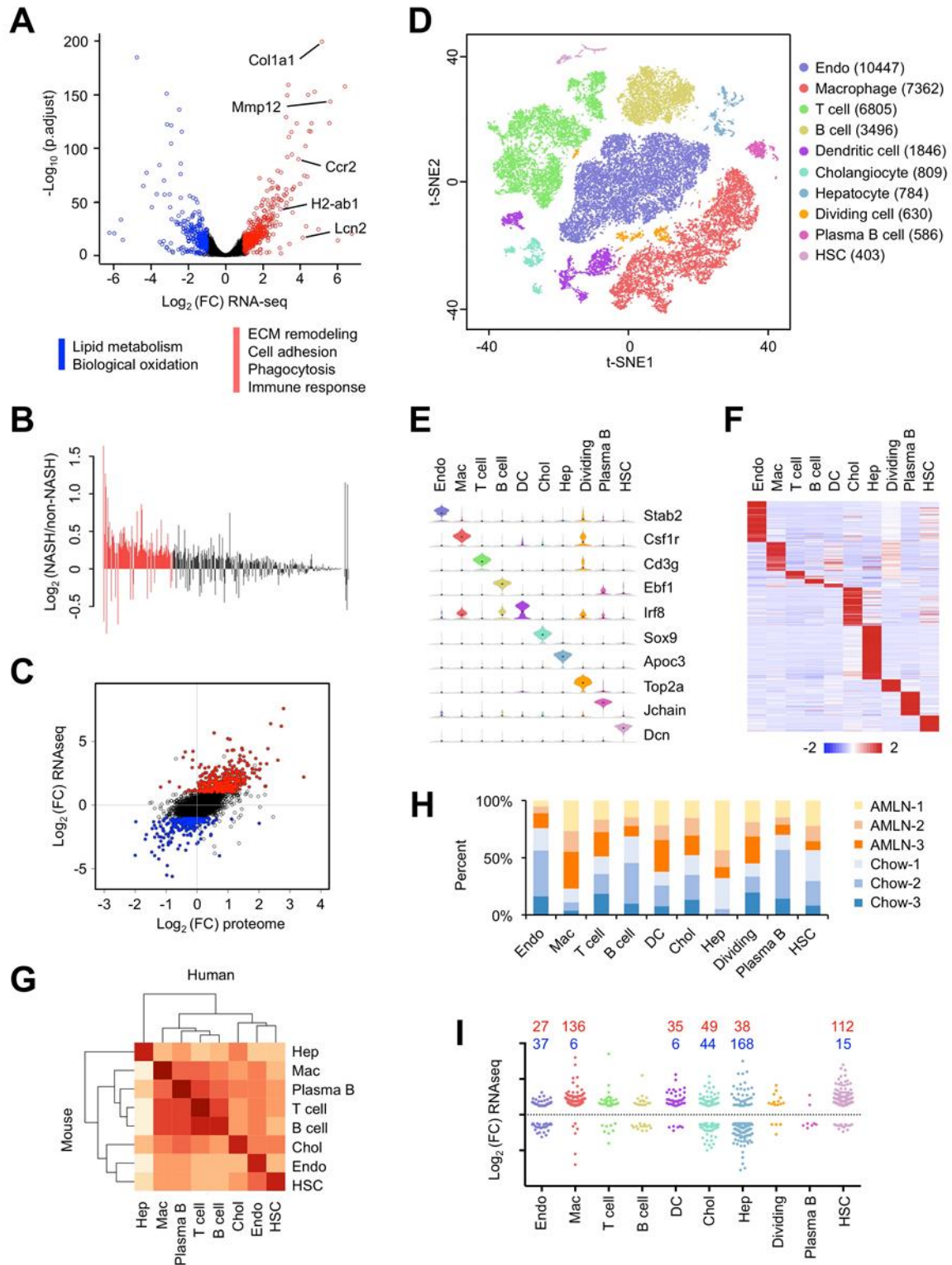


**Figure 2.1 Single-cell RNA-seq analysis of NPC isolated from healthy and NASH mouse livers.**
(A) Volcano plot of hepatic gene expression in chow and AMLN diet-fed mice analyzed by RNA-seq of total liver mRNA. Genes upregulated or downregulated by more than 2-fold are shown in red and blue, respectively.

(B) Bar graph of relative expression comparing NASH (NAS > 5.0) and non-NASH (NAS < 3.0) human livers for the list of genes upregulated in mouse NASH. Red bars denote genes differentially regulated in human NASH (FDR < 0.1).

(C) Correlation between RNA-seq and quantitative proteomic analyses. Shown is scatter plot of log-transformed fold change (FC) of mRNA (y-axis) and protein (x-axis) expression values comparing AMLN and chow livers. Genes upregulated or downregulated by more than 2-fold in RNA-seq are indicated in red and blue, respectively.

(D) t-SNE visualization of liver cell clusters based on 33,168 single cell transcriptomes. Cell counts for endothelial cells (Endo), macrophages, T cells, B cells, DC, cholangiocytes (Chol), hepatocytes (Hep), dividing cells, plasma B cells and HSC are indicated in parentheses.

(E) Violin plots showing representative marker gene expression for each cluster.

(F) Heat map of cluster marker genes.

(G) Correlation matrix between mouse and human liver cells. Normalized average UMI values for each cell type were used in the calculation of correlation coefficient values.

(H) Percent contribution of chow (blue) and AMLN (orange) mouse liver cells from in each cluster.

(I) Cell type distribution for upregulated (red) and downregulated (blue) genes in NASH mouse (A). Each gene was assigned a cluster based on the cell type with highest expression for that gene.
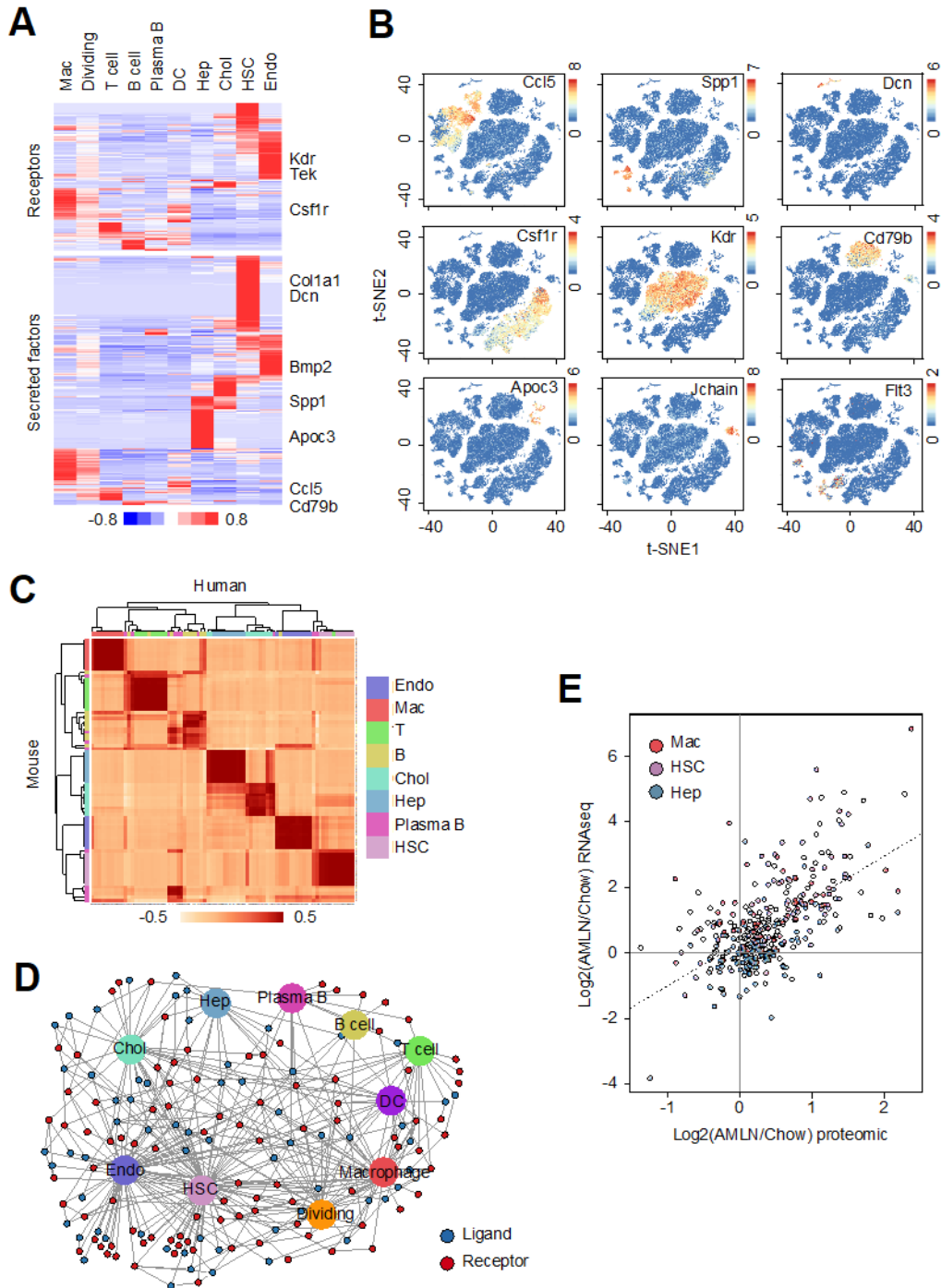
**Figure 2.2 Liver cell secretome gene analysis.**
(A) Heat map representation of genes expression for membrane receptors (top) and secreted factors (bottom) among liver cell types. Genes with normalized UMI values > 1.0 in at least one cluster were included in the analyses.
(B) Visualization of cell-type specific ligand and receptor gene expression.
(C) Correlation of ligand and receptor gene expression between mouse and human liver cells.
(D) Network visualization of ligand-receptor connectivity among different mouse liver cell types.

(E) Scatter plot of ligand and receptor gene expression based on RNA-seq and quantitative proteomic data. The genes with highest expression in HSC, macrophages and hepatocytes are indicated.
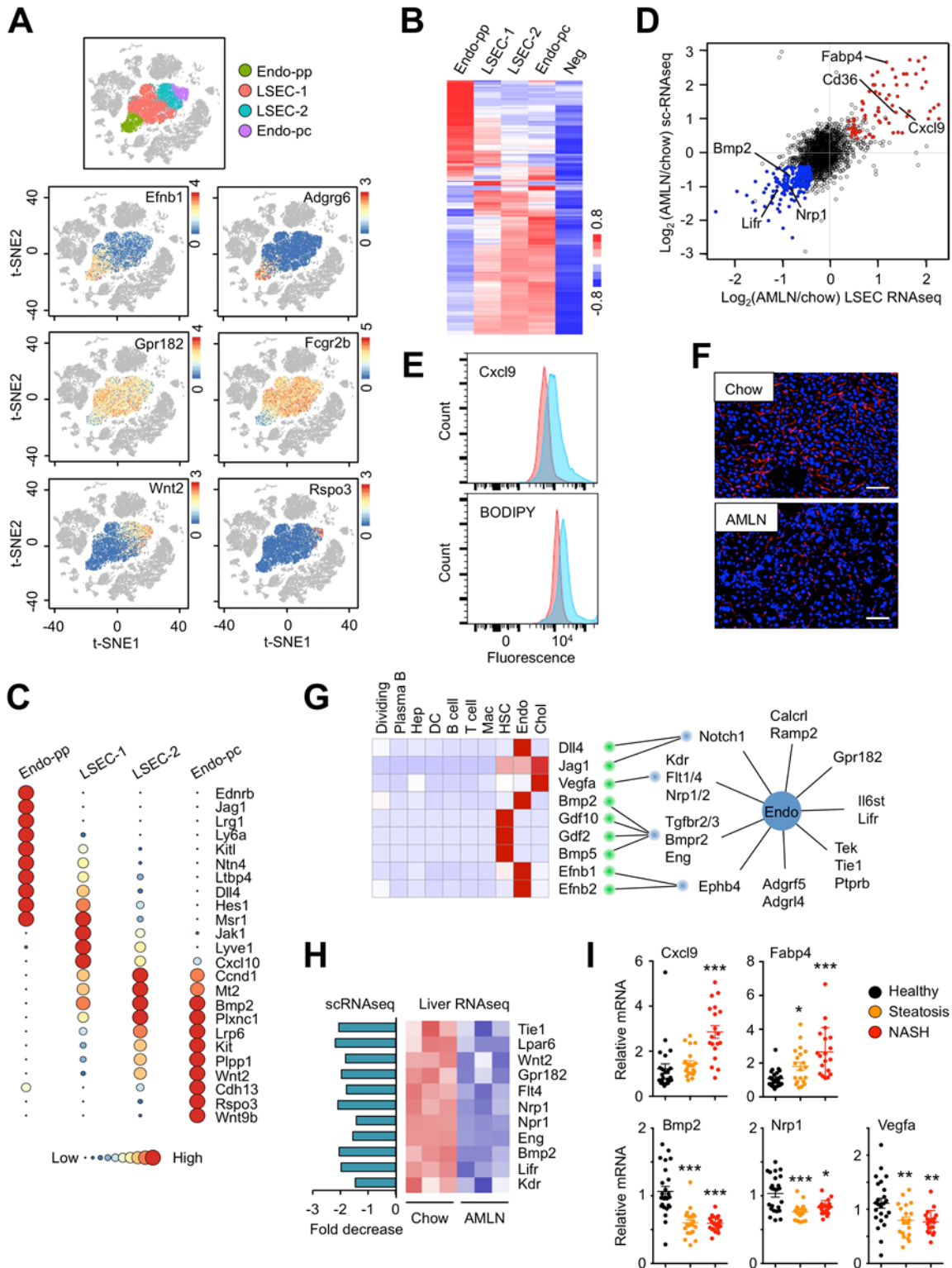
**Figure 2.3 Disruption of the hepatic vascular signaling network in NASH.**
(A) t-SNE visualization and marker gene expression in four liver endothelial subtypes.
(B) Clustering analysis and heat map of gene expression in four endothelial subtypes. Averaged expression values from non-endothelial clusters were used as negative background (Neg).
(C) Circle plots illustrating subtype-specific gene expression. Normalized average UMI values for each subcluster were represented by dot size and color intensity.

55

(D) Scatter plot of endothelial gene expression revealed by scRNA-seq of liver NPC (y-axis) and RNA-seq analysis of LSEC (x-axis) isolated from chow and AMLN mouse livers.

(E) Flow cytometry analysis of Cxcl9 and lipid accumulation (BODIPY) in gated LSEC from chow (red) and AMLN (blue) mouse livers.

(F) Anti-FCGR2B immunofluorescence staining of frozen liver sections from chow and AMLN mice (scale bar=100μm).

(G) The liver vascular signaling network. Shown are heat map of ligands (left) and expression of membrane receptors in the endothelial cluster (right). Red lines indicate predicted ligand-receptor pairs.

(H) Disruption of endothelial cell signaling network in NASH. Expression of angiocrine ligands and receptors in chow and AMLN mouse livers was analyzed by scRNA-seq (left) and liver RNA-seq (right).

(I) Dot plot of microarray expression values in a cohort of healthy individuals and patients with steatosis or NASH. Data were analyzed using one-way ANOVA. *p<0.05, ** p<0.01, *** p<0.001 vs. healthy.
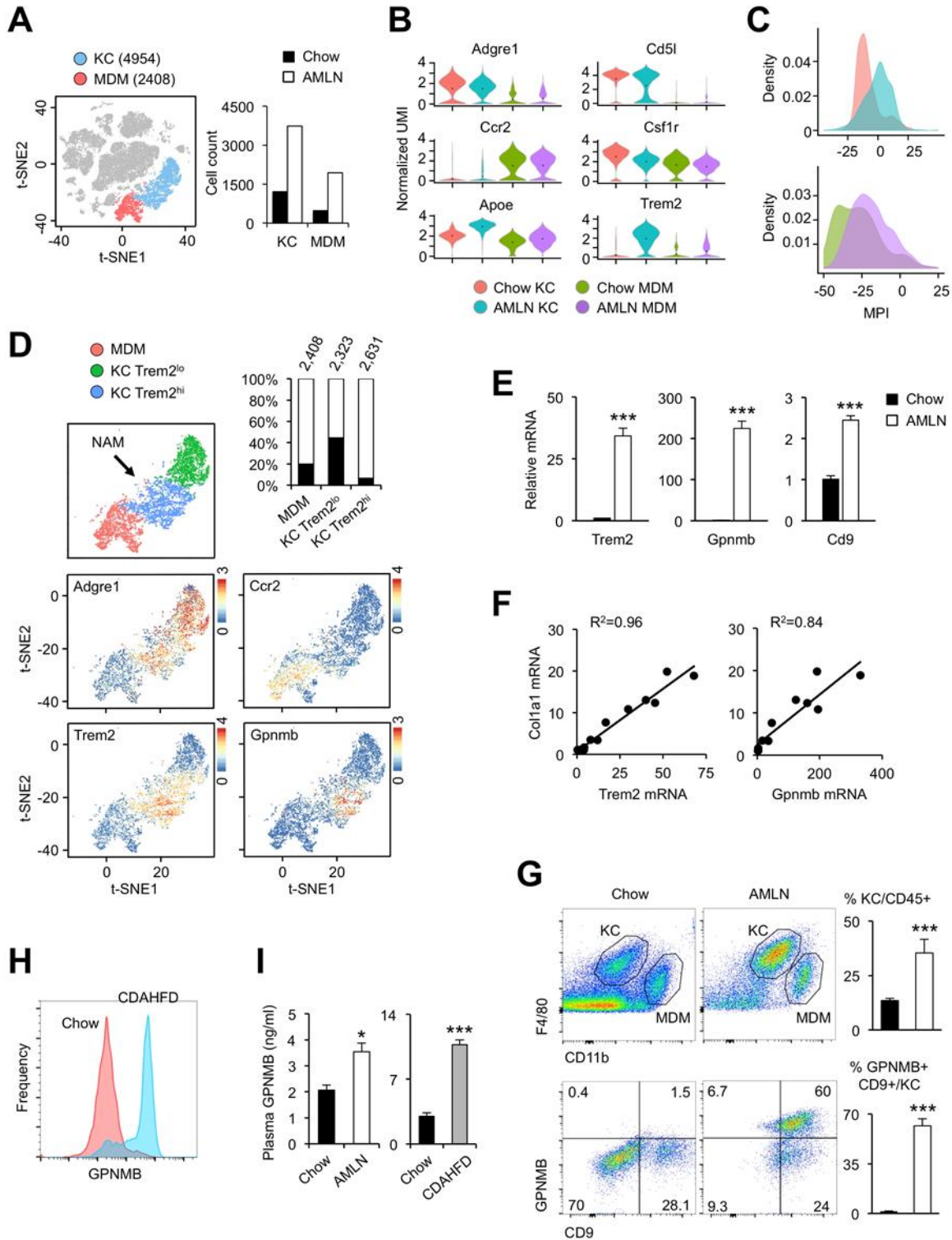
**Figure 2.4 Emergence of NASH-associated macrophages in the liver.**
(A) Illustration of tissue-resident Kupffer cells (KC, blue) and monocyte-derived macrophages (MDM, red). Total cell counts from chow and AMLN mouse livers for each subcluster are shown on the right (n=3).
(B) Violin plot of normalized UMI showing distribution of marker gene expression.
(C) Histogram of macrophage polarization index of liver macrophages. Cell types and diets are colored as in (B).

(D) t-SNE plot illustrating subpopulations of KC marked by low (green) and high (blue) Trem2 mRNA expression. Percentage contributions of chow (filled) and AMLN (open) macrophages to each subpopulation and total cell counts are indicated. Feature plots of marker gene expression are shown at the bottom.

(E) Whole liver qPCR analysis for NAM marker genes in mice fed chow or AMLN diet for 6 months (n=4).

(F) Correlation of liver gene expression in a cohort of mice fed AMLN diet for three months.

(G) Flow cytometry analysis of liver cells. Percentage of KC in CD45+ cells (top) and GPNMB+ CD9+ KC in mice fed chow or AMLN diet are shown (n=3).

(H) Histogram of GPNMB flow cytometry analysis of KC subpopulation in mice fed chow (red) or CDAHFD (blue) for 4 weeks (n=3).

(I) Plasma GPNMB levels measured by ELISA comparing chow with AMLN mice (n=10) or chow with CDAHFD mice (n=5). Data in (E), (G), and (I) represent mean ± SEM. *$p<0.05$, **$p<0.01$, ***$p<0.001$ vs. chow; two-tailed unpaired Student's t-test.
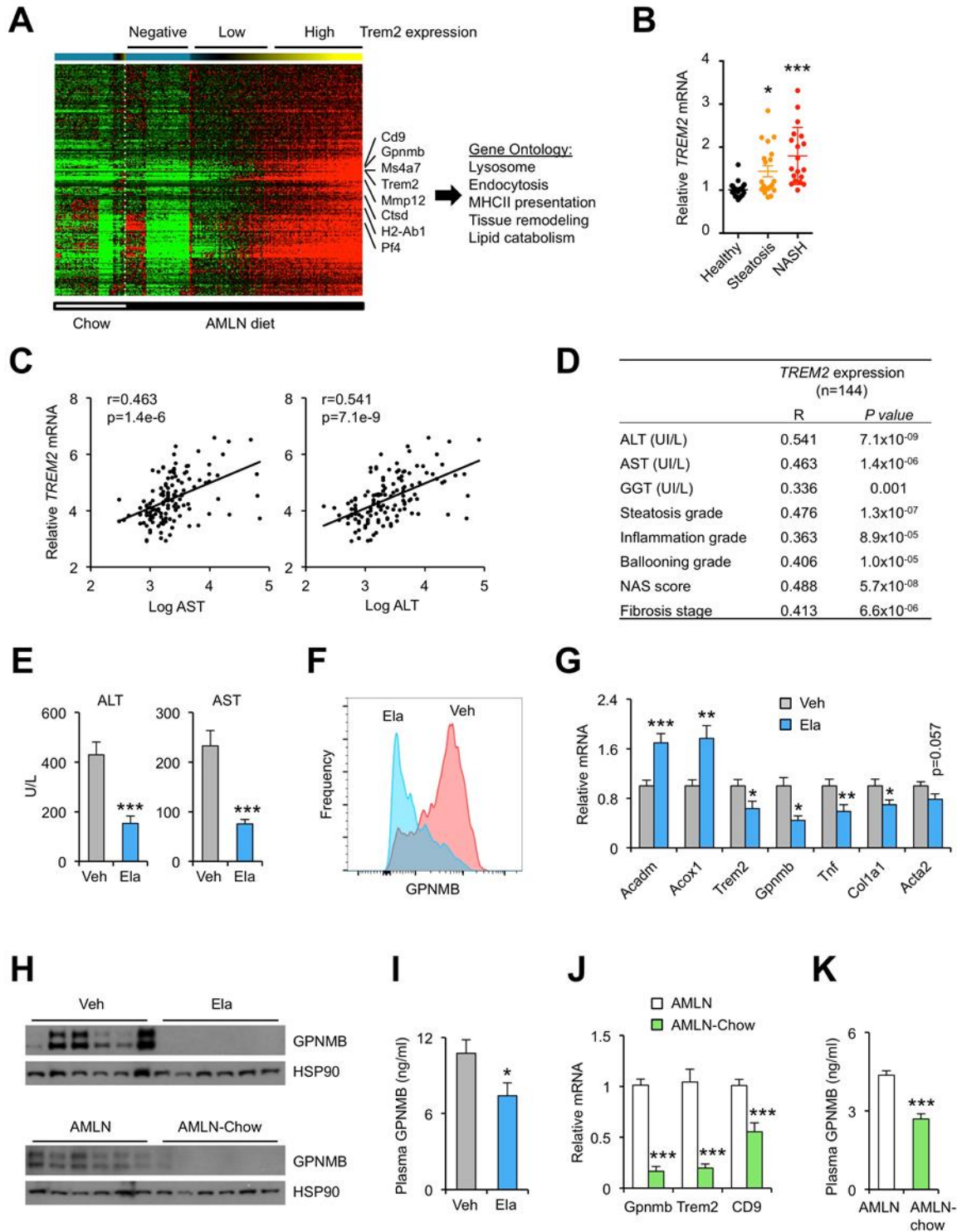
**Figure 2.5 Dynamic regulation of NAM in human NASH and during NASH resolution.**
(A) Heat map representation of macrophage gene expression. Cells were ordered by increasing Trem2 expression and binned per 25 cells for analysis. A cluster of genes positively correlated with Trem2 is shown.
(B) Dot plot of microarray expression values for Trem2 in a cohort of healthy individuals and patients with steatosis or NASH. Data represent mean ± SE and were analyzed using one-way ANOVA. *p<0.05, ** p<0.01, *** p<0.001.

(C) Association between liver TREM2 mRNA expression and plasma AST and ALT levels in a cohort of 144 NASH patients.

(D) Association between liver TREM2 mRNA expression and NASH parameters in the human patient cohort.

(E) Plasma ALT and AST concentrations in CDAHFD-fed mice gavaged daily with vehicle (Veh) or Elafibranor (Ela) for 24 days (n=10).

(F) Flow cytometry analysis of GPNMB expression in KC isolated from treated mice (n=3).

(G) qPCR analysis of liver gene expression.

(H) Immunoblots of whole liver extracts in mice from (E) (top) and extracts from mice fed AMLN diet for six months (AMLN) or four months followed by chow for two months (AMLN-chow) (bottom).

(I) Plasma GPNMB levels.

(J) qPCR analysis of liver gene expression in mice fed AMLN diet for six months (AMLN) or four months followed by chow for two months (NASH-chow).

(K) Plasma GPNMB levels in mice from J. Data in (E), (G) and (I-K) represent mean ± SEM. *p<0.05, **p<0.01, ***p<0.001 vs. chow; two-tailed unpaired Student's t-test.

**A**

Chow   NASH

**ECM**
| | |
|---|---|
| Col1a1 | Fbln1 |
| Col1a2 | Fbln5 |
| Col3a1 | Lamb1 |
| Col6a2 | Mgp |
| Col14a1 | Smoc2 |
| Dpt | Sparc |
| Ecm1 | Sparcl1 |
| Eln | |

**ECM remodeling**
| | |
|---|---|
| Adamts2 | Loxl1 |
| Adamtsl2 | Pcolce |
| Adamts5 | Timp1 |
| Aebp1 | Timp2 |
| Htra3 | Wfdc1 |

**Proteoglycan**
| | |
|---|---|
| Bgn | Dcn |
| Fmod | Ogn |
| Lum | Srpx2 |

-1   0   1

**D**

| ECM Fibrosis | Cytokine Signaling | HSC Contraction |
|---|---|---|
| Pdgfra | Tnfrsf1a | Ednra |
| Pdgfrb | Tnfrsf21 | Ednrb |
| Fgfr2 | Igf1r | Adra2b |
| Ddr1 | Ngfr | Agtr1a |
| Ddr2 | Axl | Vipr1 |
| Ryk | Ifnar2 | Pth1r |
| Tgfbr3 | Il6st | Ramp1 |
| Robo2 | Lifr | Ramp2 |
| Eng | Il11ra1 | Calcrl |
| Lrp1 | Il1r1 | |
| Bmpr2 | Axl | |
| Bmpr1a | Ackr3 | |

**B**

Receptor (blue) / Ligand (orange)

**E**

Plasma B, Hep, B cell, T cell, Mac, HSC, Endo, Chol

EDNRB, ADRA2B, VIPR1, PTH1R, RAMP1, RAMP2, CALCRL

Mouse / Human

**C**

HSC ligands

Log2(AMLN/chow)

Up in AMLN / Down in AMLN

Tnfrsf11b, Cxcl12, Ctgf, Bmp5, Gdf2, Efnb1, Ntn1, App, Csf1, Ccl11, Cxcl1, Postn, Ngf, Gdf10, Gas6, Cxcl10, Cxcl16, Wnt4, Fstl1, Cxcl14, Ccl2

**F**

Desmin DCN   VIPR1 DCN

Merged

**Figure 2.6 Landscape of the HSC signaling network.**
(A) Heat map representation of HSC-enriched secretome genes using liver RNA-seq data from chow and AMLN mice. Genes encoding structural proteins of ECM and those involved in ECM remodeling are indicated.
(B) The HSC secretome. Ligands exhibiting > 3-fold enriched expression in the HSC cluster are shown in orange with their known receptors indicated in blue. The ligand-receptor pairs are shown when receptor expression was observed in at least one cluster (normalized UMI>1.0) based on the scRNA-seq dataset.

61

(C) Regulation of stellakine gene expression in NASH. Average expression values from chow and AMLN liver RNA-seq dataset were used.
(D) The HSC-enriched membrane receptors.
(E) Circle plot of receptor gene expression in mouse and human liver cells.
(F) Immunofluorescence staining of frozen liver sections using antibodies indicated at the top. Nuclei were stained using DAPI (blue). Arrows indicate co-localization of protein expression in HSC (scale bar=50μm).
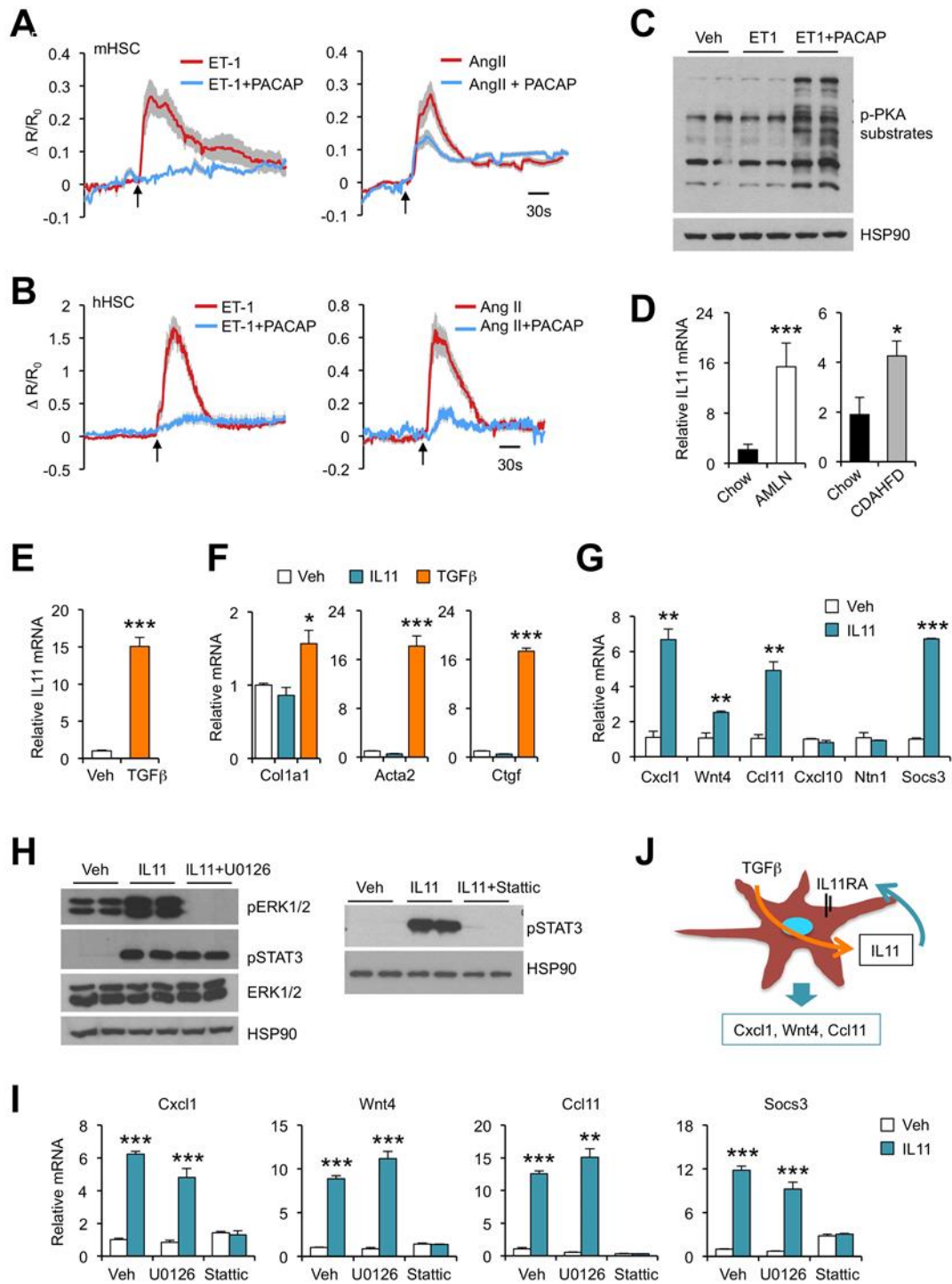
**Figure 2.7 Functional analysis of vasoactive hormone signaling and the autocrine IL11 loop in HSC.**
(A) Averaged intracellular calcium traces of primary mouse HSC treated with 100 nM of ET-1 (n=14), ET-1 plus 100 nM of PACAP (n=30), 100 nM of Ang II (n=25) or Ang II plus PACAP (n=41).
(B) Averaged intracellular calcium traces of primary human HSC treated with 100 nM ET-1 (n=23), ET-1 plus 100 nM of PACAP (n=16), 100 nM of Ang II (n=21) or Ang II plus PACAP (n=21). Arrows indicate initiation of treatments. Data represent mean ± SD.

(C) Immunoblots of mouse HSC lysates treated with vehicle (Veh), ET-1 or ET-1 plus PACAP for 10 min.

(D) qPCR analysis of liver Il11 expression in mice fed chow (n=4) or AMLN diet (n=4) for six months. A separate cohort of mice was fed chow (n=5) or CDAHFD (n=5) for four weeks.

(E) qPCR analysis of Il11 expression in immortalized mouse HSC treated with Veh or TGFβ (5 ng/ml) for 24 hrs.

(F) qPCR analysis of gene expression in immortalized mouse HSC treated with Veh, IL11 (100 ng/ml) or TGFβ (5 ng/ml) for 24 hrs.

(G) qPCR analysis of gene expression in immortalized mouse HSC treated with Veh or IL11 (100 ng/ml) for 4 hrs.

(H) Immunoblots of total lysates from immortalized mouse HSC treated for 10 min.

(I) qPCR analysis of gene expression in immortalized mouse HSC treated with Veh or IL11 without or with U0126 (20 nM) or Stattic (20 μM).

(J) Regulation of stellakine gene expression by autocrine IL11 signaling in HSC.
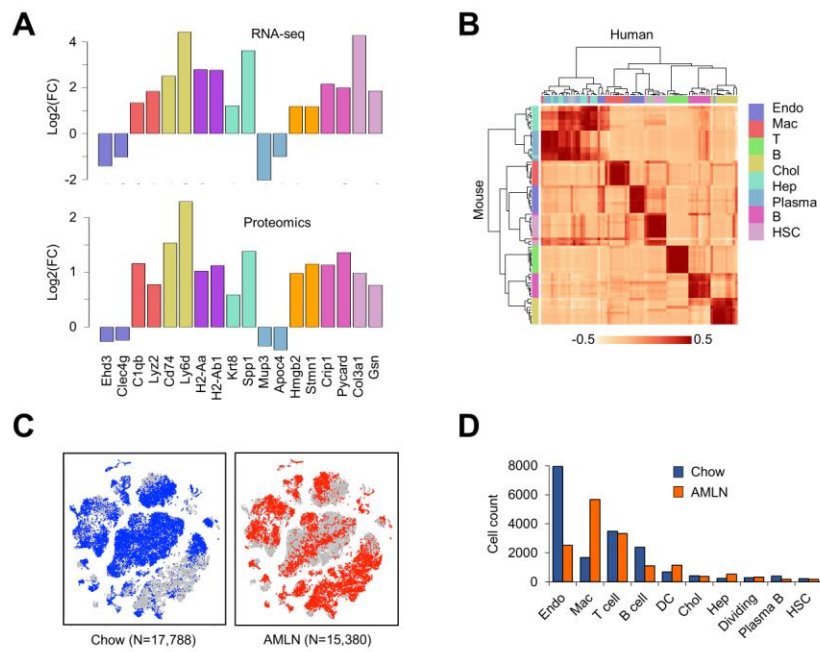


**Figure 2.8 Supplementary Figure S1. Single-cell analysis of liver NPC from healthy and NASH mice.**

(A) Relative mRNA and protein expression for a subset of genes in chow or AMLN livers.

(B) Correlation matrix between mouse and human liver cells. Normalized UMI average of 10 marker genes for each cell type was used for calculation of correlation coefficients.

(C) Mapping of sequenced single cells from three pairs of chow and AMLN mice to the master t-SNE plot.

(D) Cell count for each cluster.
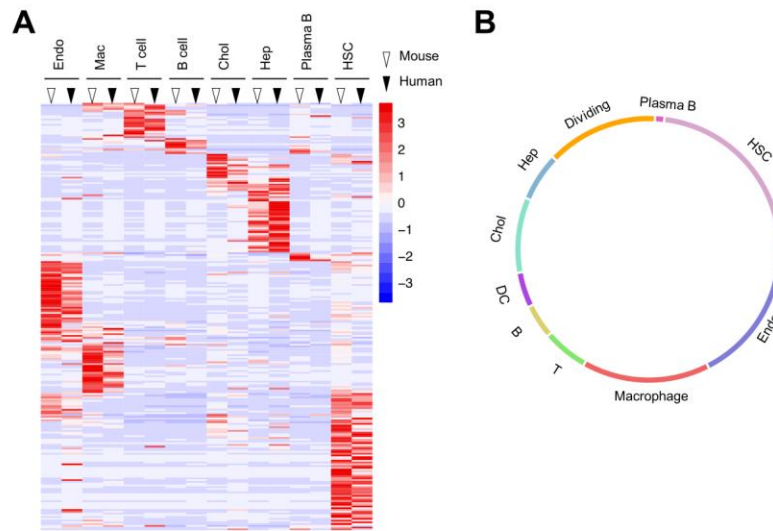
**Figure 2.9 Supplementary Figure S2. Secretome gene analysis of liver cells.**
(A) Heat map of ligand and receptor gene expression in mouse (open triangle) and human (filled triangle) liver cells. The mouse and human expression matrices are scaled separately. Note that cell type-restricted expression patterns are highly conserved between mouse and human.
(B) Consolidated network visualization of liver cell crosstalk. Colored lines indicate predicted ligand and receptor pairs among different cell types.
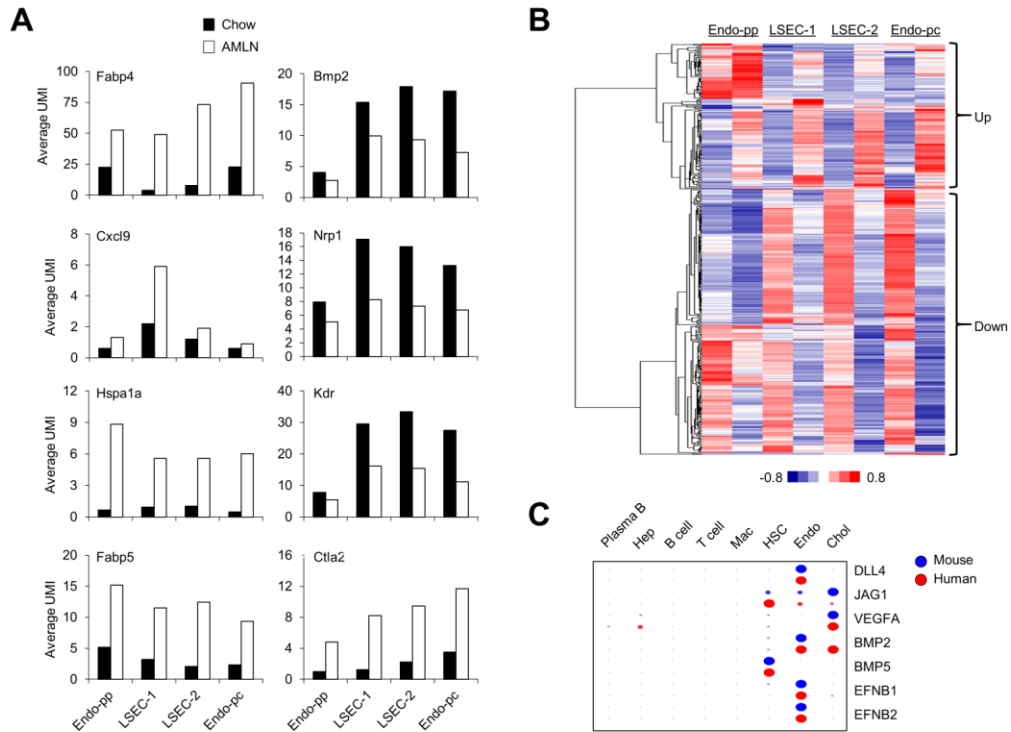
**Figure 2.10 Supplementary Figure S3. Disruption of vascular signaling in the liver during NASH.**
(A) Normalized UMI values for the indicated genes in endothelial subclusters from chow and NASH mice.
(B) Hierarchical clustering of differentially expressed genes in chow and AMLN endothelial subclusters. Genes with normalized UMI values > 1.0 in at least one subcluster and differential expression of more than 2-fold were shown.
(C) Dot plot of ligand gene expression in mouse and human liver cells. Higher expression values are indicated by larger size and higher color saturation.
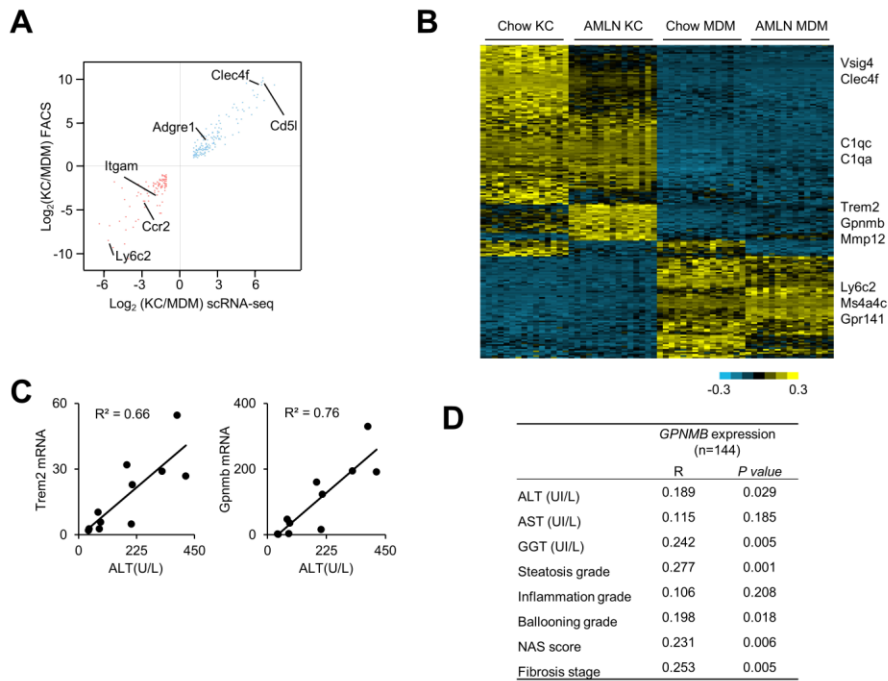
**Figure 2.11 Supplementary Figure S4. Emergence of NASH-associated macrophage in the liver.**
(A) Correlation of log fold enrichment of genes in KC (blue) versus MDM (red) cluster for FACS sorted macrophage microarray (GSE98782) data compared with scRNA-seq data.
(B) Heat map highlighting differentially expressed genes in chow and NASH KC and MDM populations. Cells within each cluster were binned (25 cells per bin) and averaged UMI values were used for clustering analysis.
(C) Correlation between plasma ALT and hepatic Trem2 and Gpnmb mRNA expression in a cohort of mice fed AMLN diet for three months.
(D) Association between liver *GPNMB* mRNA expression and NASH parameters in a cohort of NASH patients.
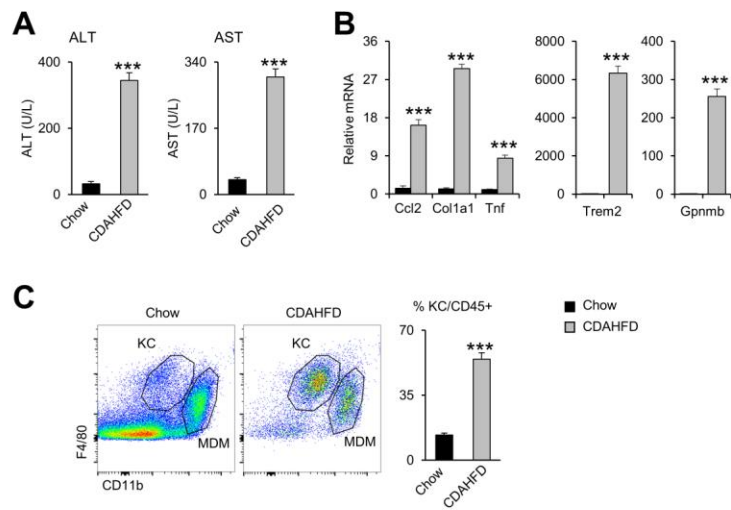
**Figure 2.12 Supplementary Figure S5. Induction of NAM and its associated genes during CDAHFD-induced NASH.**
Mice were fed chow (filled, n=5) or CDAHFD (grey, n=5) for 4 weeks.
(A) Plasma ALT and AST concentrations.
(B) qPCR analysis of liver gene expression.
(C) Flow cytometry analysis of liver macrophages in mice fed chow or CDAHFD diet (n=3). Data represent mean ± SEM. ***$p<0.001$ vs. chow; two-tailed unpaired Student's t-test.
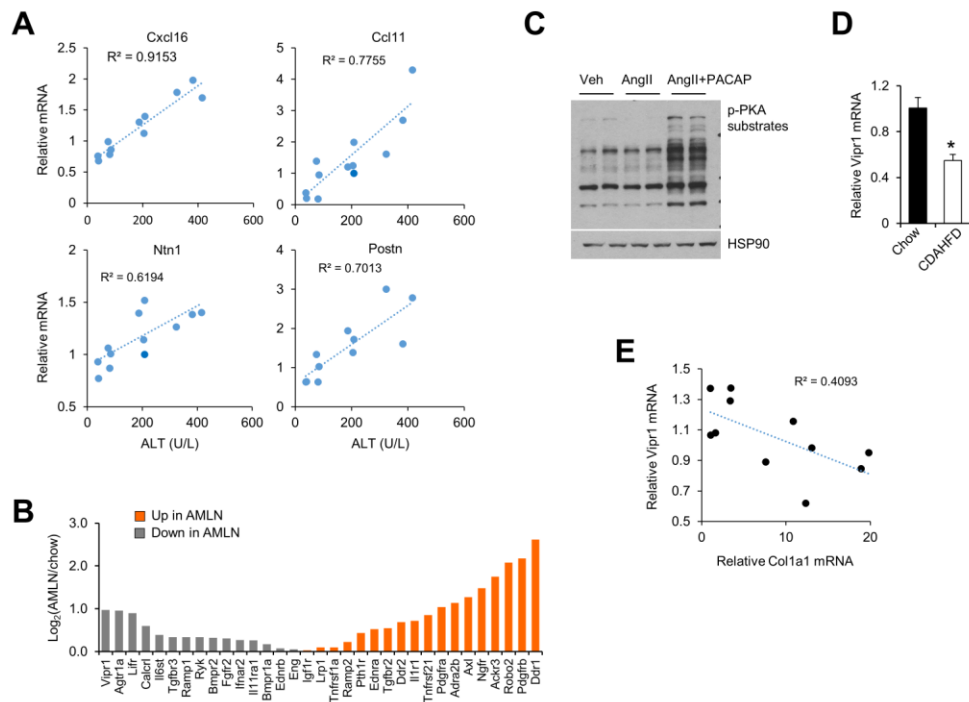
**Figure 2.13 Supplementary Figure S6. HSC secretome and receptor gene expression.**
(A) Correlation between plasma ALT levels and stellakine gene expression in a cohort of mice fed AMLN for three months.
(B) Regulation of HSC receptor gene expression in NASH. Averaged RNA-seq expression values from chow and NASH livers were used.
(C) Immunoblots of mouse HSC lysates treated with vehicle (Veh), Ang II or Ang II plus PACAP for 10 min.
(D) qPCR analysis of Vipr1 gene expression in mice fed chow (n=4) or AMLN diet (n=4) for five months.
(E) Correlation between Vipr1 and Col1a1 gene expression in a cohort of mice fed AMLN diet for three months.
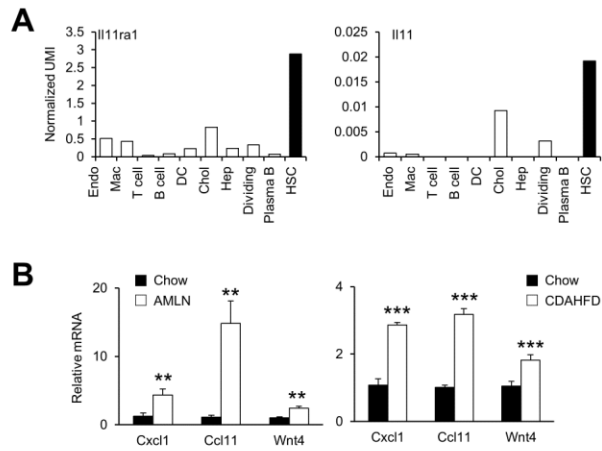
**Figure 2.14 Supplementary Figure S7. Regulation of stellakine gene expression by autocrine IL11 signaling in HSC.**
(A) Bar graphs showing relative expression of Il11ra1 and Il11 among different cell types in mouse liver. Normalized UMI values were shown.
(B) qPCR analysis of stellakine gene expression in mice fed chow (n=4) or AMLN diet (n=4) for five months. A separate cohort of mice was fed chow (n=5) or CDAHFD diet (n=5) for four weeks. Data represent mean ± SEM. **p<0.01, ***p<0.001 vs. chow; two-tailed unpaired Student's t-test.

## References

Arendt, B.M., Comelli, E.M., Ma, D.W., Lou, W., Teterina, A., Kim, T., Fung, S.K., Wong, D.K., McGilvray, I., Fischer, S.E., et al. (2015). Altered hepatic gene expression in nonalcoholic fatty liver disease is associated with lower hepatic n-3 and n-6 polyunsaturated fatty acids. Hepatology 61, 1565-1578.

Butler, A., Hoffman, P., Smibert, P., Papalexi, E., and Satija, R. (2018). Integrating single-cell transcriptomic data across different conditions, technologies, and species. Nat Biotechnol 36, 411-420.

Chen, Y., Zhang, Y., Yin, Y., Gao, G., Li, S., Jiang, Y., Gu, X., and Luo, J. (2005). SPD--a web-based secreted protein database. Nucleic Acids Res 33, D169-173.

Clapper, J.R., Hendricks, M.D., Gu, G., Wittmer, C., Dolman, C.S., Herich, J., Athanacio, J., Villescaz, C., Ghosh, S.S., Heilig, J.S., et al. (2013). Diet-induced mouse model of fatty liver disease and nonalcoholic steatohepatitis reflecting clinical disease progression and methods of assessment. Am J Physiol Gastrointest Liver Physiol 305, G483-495.

Cohen, J.C., Horton, J.D., and Hobbs, H.H. (2011). Human fatty liver disease: old questions and new insights. Science 332, 1519-1523.

Deczkowska, A., Keren-Shaul, H., Weiner, A., Colonna, M., Schwartz, M., and Amit, I. (2018). Disease-Associated Microglia: A Universal Immune Sensor of Neurodegeneration. Cell 173, 1073-1081.

Diehl, A.M., and Day, C. (2017). Cause, Pathogenesis, and Treatment of Nonalcoholic Steatohepatitis. N Engl J Med 377, 2063-2072.

Friedman, S.L. (2008). Hepatic stellate cells: protean, multifunctional, and enigmatic cells of the liver. Physiol Rev 88, 125-172.

Gawad, C., Koh, W., and Quake, S.R. (2016). Single-cell genome sequencing: current state of the science. Nat Rev Genet 17, 175-188.

Geven, C., Kox, M., and Pickkers, P. (2018). Adrenomedullin and Adrenomedullin-Targeted Therapy As Treatment Strategies Relevant for Sepsis. Front Immunol 9, 292.

Guo, L., Zhang, P., Chen, Z., Xia, H., Li, S., Zhang, Y., Kobberup, S., Zou, W., and Lin, J.D. (2017). Hepatic neuregulin 4 signaling defines an endocrine checkpoint for steatosis-to-NASH progression. J Clin Invest 127, 4449-4461.

Gutierrez-Vidal, R., Vega-Badillo, J., Reyes-Fermin, L.M., Hernandez-Perez, H.A., Sanchez-Munoz, F., Lopez-Alvarez, G.S., Larrieta-Carrasco, E., Fernandez-Silva, I., Mendez-Sanchez, N., Tovar, A.R., et al. (2015). SFRP5 hepatic expression is associated with non-alcoholic liver disease in morbidly obese women. Ann Hepatol 14, 666-674.

Halpern, K.B., Shenhav, R., Massalha, H., Toth, B., Egozi, A., Massasa, E.E., Medgalia, C., David, E., Giladi, A., Moor, A.E., et al. (2018). Paired-cell sequencing enables spatial gene expression mapping of liver endothelial cells. Nat Biotechnol 36, 962-970.

Halpern, K.B., Shenhav, R., Matcovitch-Natan, O., Toth, B., Lemze, D., Golan, M., Massasa, E.E., Baydatch, S., Landen, S., Moor, A.E., et al. (2017). Single-cell spatial reconstruction reveals global division of labour in the mammalian liver. Nature 542, 352-356.

Han, X., Wang, R., Zhou, Y., Fei, L., Sun, H., Lai, S., Saadatpour, A., Zhou, Z., Chen, H., Ye, F., et al. (2018). Mapping the Mouse Cell Atlas by Microwell-Seq. Cell 172, 1091-1107 e1017.

Hellerbrand, C. (2013). Hepatic stellate cells--the pericytes in the liver. Pflugers Arch 465, 775-778.

Hui, S.T., Kurt, Z., Tuominen, I., Norheim, F., R, C.D., Pan, C., Dirks, D.L., Magyar, C.E., French, S.W., Chella Krishnan, K., et al. (2018). The Genetic Architecture of Diet-Induced Hepatic Fibrosis in Mice. Hepatology 68, 2182-2196.

Ji, Y., Sun, S., Goodrich, J.K., Kim, H., Poole, A.C., Duhamel, G.E., Ley, R.E., and Qi, L. (2014). Diet-induced alterations in gut microflora contribute to lethal pulmonary damage in TLR2/TLR4-deficient mice. Cell Rep 8, 137-149.

Ji, Y., Sun, S., Xia, S., Yang, L., Li, X., and Qi, L. (2012). Short term high fat diet challenge promotes alternative macrophage polarization in adipose tissue via natural killer T cells and interleukin-4. J Biol Chem 287, 24378-24386.

Jiang, T., Tan, L., Zhu, X.C., Zhang, Q.Q., Cao, L., Tan, M.S., Gu, L.Z., Wang, H.F., Ding, Z.Z., Zhang, Y.D., et al. (2014). Upregulation of TREM2 ameliorates neuropathology and rescues spatial cognitive impairment in a transgenic mouse model of Alzheimer's disease. Neuropsychopharmacology 39, 2949-2962.

Keren-Shaul, H., Spinrad, A., Weiner, A., Matcovitch-Natan, O., Dvir-Szternfeld, R., Ulland, T.K., David, E., Baruch, K., Lara-Astaiso, D., Toth, B., et al. (2017). A Unique Microglia Type Associated with Restricting Development of Alzheimer's Disease. Cell 169, 1276-1290 e1217.

Krenkel, O., Puengel, T., Govaere, O., Abdallah, A.T., Mossanen, J.C., Kohlhepp, M., Liepelt, A., Lefebvre, E., Luedde, T., Hellerbrand, C., et al. (2018). Therapeutic inhibition of inflammatory monocyte recruitment reduces steatohepatitis and liver fibrosis. Hepatology 67, 1270-1283.

Krenkel, O., and Tacke, F. (2017). Liver macrophages in tissue homeostasis and disease. Nat Rev Immunol 17, 306-321.

Leitinger, B. (2014). Discoidin domain receptor functions in physiological and pathological conditions. Int Rev Cell Mol Biol 310, 39-87.

Leon-Mimila, P., Vega-Badillo, J., Gutierrez-Vidal, R., Villamil-Ramirez, H., Villareal-Molina, T., Larrieta-Carrasco, E., Lopez-Contreras, B.E., Kauffer, L.R., Maldonado-Pintado, D.G., Mendez-Sanchez, N., et al. (2015). A genetic risk score is associated with hepatic triglyceride

content and non-alcoholic steatohepatitis in Mexicans with morbid obesity. Exp Mol Pathol 98, 178-183.

Li, C., Menoret, A., Farragher, C., Ouyang, Z., Bonin, C., Holvoet, P., Vella, A.T., and Zhou, B. (2019). Single cell transcriptomics based-MacSpectrum reveals novel macrophage activation signatures in diseases. JCI Insight 5.

Lill, C.M., Rengmark, A., Pihlstrom, L., Fogh, I., Shatunov, A., Sleiman, P.M., Wang, L.S., Liu, T., Lassen, C.F., Meissner, E., et al. (2015). The role of TREM2 R47H as a risk factor for Alzheimer's disease, frontotemporal lobar degeneration, amyotrophic lateral sclerosis, and Parkinson's disease. Alzheimers Dement 11, 1407-1416.

MacParland, S.A., Liu, J.C., Ma, X.Z., Innes, B.T., Bartczak, A.M., Gage, B.K., Manuel, J., Khuu, N., Echeverri, J., Linares, I., et al. (2018). Single cell RNA sequencing of human liver reveals distinct intrahepatic macrophage populations. Nat Commun 9, 4383.

Makhlouf, G.M., and Murthy, K.S. (1997). Signal transduction in gastrointestinal smooth muscle. Cell Signal 9, 269-276.

Matsumoto, M., Hada, N., Sakamaki, Y., Uno, A., Shiga, T., Tanaka, C., Ito, T., Katsume, A., and Sudoh, M. (2013). An improved mouse model that rapidly develops fibrosis in non-alcoholic steatohepatitis. Int J Exp Pathol 94, 93-103.

Mederacke, I., Dapito, D.H., Affo, S., Uchinami, H., and Schwabe, R.F. (2015). High-yield and high-purity isolation of hepatic stellate cells from normal and fibrotic mouse livers. Nat Protoc 10, 305-315.

Meex, R.C.R., and Watt, M.J. (2017). Hepatokines: linking nonalcoholic fatty liver disease and insulin resistance. Nat Rev Endocrinol 13, 509-520.

Meyer, D.H., Krull, N., Dreher, K.L., and Gressner, A.M. (1992). Biglycan and decorin gene expression in normal and fibrotic rat liver: cellular localization and regulatory factors. Hepatology 16, 204-216.

Meyer, J., Lacotte, S., Morel, P., Gonelle-Gispert, C., and Buhler, L. (2016). An optimized method for mouse liver sinusoidal endothelial cell isolation. Exp Cell Res 349, 291-301.

Obana, M., Maeda, M., Takeda, K., Hayama, A., Mohri, T., Yamashita, T., Nakaoka, Y., Komuro, I., Takeda, K., Matsumiya, G., et al. (2010). Therapeutic activation of signal transducer and activator of transcription 3 by interleukin-11 ameliorates cardiac fibrosis after myocardial infarction. Circulation 121, 684-691.

Pais, R., Barritt, A.S.t., Calmus, Y., Scatton, O., Runge, T., Lebray, P., Poynard, T., Ratziu, V., and Conti, F. (2016). NAFLD and liver transplantation: Current burden and expected challenges. J Hepatol 65, 1245-1257.

Perugorria, M.J., Esparza-Baquer, A., Oakley, F., Labiano, I., Korosec, A., Jais, A., Mann, J., Tiniakos, D., Santos-Laso, A., Arbelaiz, A., et al. (2018). Non-parenchymal TREM-2 protects the liver from immune-mediated hepatocellular damage. Gut.

Poisson, J., Lemoinne, S., Boulanger, C., Durand, F., Moreau, R., Valla, D., and Rautou, P.E. (2017). Liver sinusoidal endothelial cells: Physiology and role in liver diseases. J Hepatol 66, 212-227.

Rafii, S., Butler, J.M., and Ding, B.S. (2016). Angiocrine functions of organ-specific endothelial cells. Nature 529, 316-325.

Ramilowski, J.A., Goldberg, T., Harshbarger, J., Kloppmann, E., Lizio, M., Satagopam, V.P., Itoh, M., Kawaji, H., Carninci, P., Rost, B., et al. (2015). A draft network of ligand-receptor-mediated multicellular signalling in human. Nat Commun 6, 7866.

Regev, A., Teichmann, S.A., Lander, E.S., Amit, I., Benoist, C., Birney, E., Bodenmiller, B., Campbell, P., Carninci, P., Clatworthy, M., et al. (2017). The Human Cell Atlas. Elife 6.

Reynaert, H., Urbain, D., and Geerts, A. (2008). Regulation of sinusoidal perfusion in portal hypertension. Anat Rec (Hoboken) 291, 693-698.

Robinson, M.W., Harmon, C., and O'Farrelly, C. (2016). Liver immunology and its role in inflammation and homeostasis. Cell Mol Immunol 13, 267-276.

Romero-Gomez, M., Zelber-Sagi, S., and Trenell, M. (2017). Treatment of NAFLD with diet, physical activity and exercise. J Hepatol 67, 829-846.

Samuel, V.T., and Shulman, G.I. (2018). Nonalcoholic Fatty Liver Disease as a Nexus of Metabolic and Hepatic Diseases. Cell Metab 27, 22-41.

Schafer, S., Viswanathan, S., Widjaja, A.A., Lim, W.W., Moreno-Moral, A., DeLaughter, D.M., Ng, B., Patone, G., Chow, K., Khin, E., et al. (2017). IL-11 is a crucial determinant of cardiovascular fibrosis. Nature 552, 110-115.

Sims, N.A., and Walsh, N.C. (2010). GP130 cytokines and bone remodelling in health and disease. BMB Rep 43, 513-523.

Staels, B., Rubenstrunk, A., Noel, B., Rigou, G., Delataille, P., Millatt, L.J., Baron, M., Lucas, A., Tailleux, A., Hum, D.W., et al. (2013). Hepatoprotective effects of the dual peroxisome

proliferator-activated receptor alpha/delta agonist, GFT505, in rodent models of nonalcoholic fatty liver disease/nonalcoholic steatohepatitis. Hepatology 58, 1941-1952.

Tabibian, J.H., Masyuk, A.I., Masyuk, T.V., O'Hara, S.P., and LaRusso, N.F. (2013). Physiology of cholangiocytes. Compr Physiol 3, 541-565.

Tabula Muris, C., Overall, c., Logistical, c., Organ, c., processing, Library, p., sequencing, Computational data, a., Cell type, a., Writing, g., et al. (2018). Single-cell transcriptomics of 20 mouse organs creates a Tabula Muris. Nature 562, 367-372.

Tanay, A., and Regev, A. (2017). Scaling single-cell genomics from phenomenology to mechanism. Nature 541, 331-338.

Trim, N., Morgan, S., Evans, M., Issa, R., Fine, D., Afford, S., Wilkins, B., and Iredale, J. (2000). Hepatic stellate cells express the low affinity nerve growth factor receptor p75 and undergo apoptosis in response to nerve growth factor stimulation. Am J Pathol 156, 1235-1243.

van der Lienden, M.J.C., Gaspar, P., Boot, R., Aerts, J., and van Eijk, M. (2018). Glycoprotein Non-Metastatic Protein B: An Emerging Biomarker for Lysosomal Dysfunction in Macrophages. Int J Mol Sci 20.

Vega-Badillo, J., Gutierrez-Vidal, R., Hernandez-Perez, H.A., Villamil-Ramirez, H., Leon-Mimila, P., Sanchez-Munoz, F., Moran-Ramos, S., Larrieta-Carrasco, E., Fernandez-Silva, I., Mendez-Sanchez, N., et al. (2016). Hepatic miR-33a/miR-144 and their target gene ABCA1 are associated with steatohepatitis in morbidly obese subjects. Liver Int 36, 1383-1391.

Wang, G.X., Zhao, X.Y., Meng, Z.X., Kern, M., Dietrich, A., Chen, Z., Cozacov, Z., Zhou, D., Okunade, A.L., Su, X., et al. (2014). The brown fat-enriched secreted factor Nrg4 preserves metabolic homeostasis through attenuation of hepatic lipogenesis. Nat Med 20, 1436-1443.

Wang, Q., Sharma, V.P., Shen, H., Xiao, Y., Zhu, Q., Xiong, X., Guo, L., Jiang, L., Ohta, K., Li, S., et al. (2019). The hepatokine Tsukushi gates energy expenditure via brown fat sympathetic innervation. Nature Metabolism 1.

Wang, Y., Cella, M., Mallinson, K., Ulrich, J.D., Young, K.L., Robinette, M.L., Gilfillan, S., Krishnan, G.M., Sudhakar, S., Zinselmeyer, B.H., et al. (2015). TREM2 lipid sensing sustains the microglial response in an Alzheimer's disease model. Cell 160, 1061-1071.

Xiong, X., Wang, Q., Wang, S., Zhang, J., Liu, T., Guo, L., Yu, Y., and Lin, J.D. (2019). Mapping the molecular signatures of diet-induced NASH and its regulation by the hepatokine Tsukushi. Mol Metab 20, 128-137.

Zhao, X., Huffman, K.E., Fujimoto, J., Canales, J.R., Girard, L., Nie, G., Heymach, J.V., Wistuba, II, Minna, J.D., and Yu, Y. (2017). Quantitative Proteomic Analysis of Optimal Cutting Temperature (OCT) Embedded Core-Needle Biopsy of Lung Cancer. J Am Soc Mass Spectrom 28, 2078-2089.

# Chapter 3
## NASH-Associated Macrophages in Disease Pathogenesis

**Introduction**

We seek to characterize the novel population of NASH-associated macrophages uncovered in our single-cell study (Xiong et al., 2019). From past results alone, it is clear that this population proliferates in disease and by its transcriptional signature, is implied to be a potentially important population interacting with disease pathogenesis. Major questions regarding the population are what the origin of the macrophages are, how they are regulated, and what their function is.

**NASH-Associated macrophages are hematopoietic in origin**

In our single-cell sequencing study, we noted that in their transcriptional state, the NAMs appeared to resemble the tissue-resident Kupffer cells more closely, as opposed to the infiltrating monocyte-derived macrophages. Classically, tissue-resident populations of macrophages, including Kupffer cells, develop from a self-proliferating progenitor population seeded at their respective tissue sites in the fetal stages (Gomez Perdiguero et al., 2015; Naito et al., 1997). In contrast, monocyte-derived macrophages differentiate after chemotactic processes from hematopoietic stem cell-derived monocytes in circulation (Italiani and Boraschi, 2014; Jakubzick et al., 2017). It has been previously shown that in the liver, these monocyte-derived macrophages are able to differentiate into a state which resembles the adult tissue-resident macrophages (Beattie et al., 2016; Scott et al., 2016; van de Laar et al., 2016). These 'Kupffer-like' cells are indistinguishable from resident-derived Kupffer cells. This developmental potential implies the possibility that NAMs may derive partially or entirely from the monocyte population as opposed to the resident progenitors.

To address this question, we performed lineage tracing in bone-marrow transplanted mice. After irradiation, CD45.2-positive C57BL/6J were transplanted with CD45.1 hematopoietic stem-cells from B6.SJL donors. In this model, all hematopoietic-origin cells are represented by CD45.1 whereas the liver resident population is represented by CD45.2 (Figure 1A). Any 'Kupffer-like'

cells that derive from hematopoietic progenitors would originate from CD45.1 cells (Scott et al., 2016). Following engraftment and 6 weeks of feeding CDA-HFD, we assessed the liver macrophage populations by flow cytometry. As expected, the monocyte population in the liver was entirely from CD45.1, indicating full engraftment and repopulation of the bone marrow with donor cells (Figure 1B-C). Interestingly, the majority of Kupffer cells were CD45.1 in NASH, indicating that the dramatic increase of Kupffer-like cells previously seen in NASH likely originates from hematopoietic sources. Strikingly, virtually all of the GPNMB+/CD9+ NAMs were CD45.1+ (Figure 1D-E), indicating that the disease-associated population derives entirely from infiltrating monocyte-derived macrophages (Figure 1F).

The notion that NAMs originate from hematopoietic sources raises further questions as to the developmental hierarchy dictating NAMs. From these results, it is unclear when in the development do macrophages obtain the NAM signature including genes such as Trem2 and Gpnmb. Given that there exists a naïve population of monocyte-derived macrophages in the liver that do not have a NAM signature, it seems likely that the transcriptional profile is not acquired until after chemotaxis and infiltration. However, it remains unclear if the macrophages first differentiate into a Kupffer-like state, or gain the NAM signature first. Given evidence also that the NAM population appears in various other tissue sites with nearly identical transcriptional profiles, such as in the brain microglia and lung alveolar macrophages (Sharif et al., 2014; Wang et al., 2015; Wu et al., 2015; Zhou et al., 2020), it is likely that they would all follow a similar developmental trajectory to the liver NAMs.

**Hematopoietic Trem2-high cells are ubiquitous among tissue-resident macrophage populations**

To further study the localization, development, and function of NAMs, we have developed a knock-in Trem2-Cre mouse line (Trem2Cre) with Cre recombinase coded following endogenous Trem2 expression (Figure 2A). This model allows targeted studies on the population of Trem2-high cells, with the caveat of Cre performing recombination if Trem2 is expressed at any point in a cell's developmental trajectory. To ensure the specificity of the Cre expression, we crossed the Trem2Cre line with lox tdTomato mice to visualize Trem2 expressing cells. Immunofluorescence indicates presence of tdTomato-positive cells in the livers of double-

transgenic mice, which are not present in tdTomato mice lacking Trem2Cre (Figure 2B). These Trem2 cells co-stained entirely with F4/80 in the liver, indicating specificity of the Cre for macrophages in the liver. Interestingly, we observed a redistribution of these Trem2 macrophages following acute injury to the liver. Injection with carbon tetrachloride (CCl4) to damage peri-central hepatocytes (Pellicoro et al., 2012; Ramachandran et al., 2012) resulted in a clustering of Trem2 macrophages around sites of injury (Figure 2C). As single-cell sequencing implied, the NAM signature precludes these cells to a high capacity for antigen presentation. Consistently, these Trem2 macrophages were positive for H2ab1 on immunofluorescence (Figure 2D). These cells were negative for desmin, indicating they are independent of hepatic stellate cells. Furthermore, the distribution of Trem2 macrophages within the vicinity of desmin around sites of injury indicates they are in a similar micro-niche to active stellate cells, supporting the notion that they are homeostatic in function and communicate with them. Interestingly, when we examined F4/80 positive Kupffer-like cells on flow cytometry in these mice following CCl4-induced injury, we observed presence of tdTomato positive macrophages, but they only partially overlapped with the GPNMB-positive population of Kupffer cells (Figure 2E). This indicates that in acute liver injury, there exist some Kupffer cells beginning to adapt the NAM transcriptional signature but do not express Trem2, and vice versa, some of the Trem2 macrophages have not adapted the NAM signature.

The ability for hematopoietic-derived macrophages to gain the Trem2 signature implies that macrophages in any tissue site can adopt this form. To verify the NAM signature in other macrophage populations, we surveyed multiple tissue sites in Trem2Cre mice crossed with flox tdTomato. Interestingly, every tissue site we surveyed including brain, heart, pancreas, kidney, quad, lung, brown adipose tissue, jejunum, and colon displayed a population of Trem2-expressing cells (Figure 3A). Consistently, these cells all co-stained with F4/80, confirming that Trem2 expression is highly specific to the macrophage population. This population also appeared in the adipose tissue (Figure 3B), suggesting that they are found among the adipose tissue macrophage (ATM) population. We confirmed that RFP fluorescence was present within the F4/80 positive ATM population by flow cytometry (Figure 3C). It would seem that this population is ubiquitous throughout the body even at baseline status, indicating they play some

homeostatic role in the body, or that Trem2 expression occurs at a common point in the development of tissue-resident macrophage populations.

**The role of Trem2 in macrophage function**

Our transcriptomic studies were indicative of an important function for the NAMs, in that they enrich for expression of genes for phagocytosis and antigen presentation (Xiong et al., 2019). This correlation was consistent with previous studies on Trem2 in other tissue sites. The greatest share of research on this macrophage population has been in Trem2-positive microglia of the brain (Keren-Shaul et al., 2017; Wang et al., 2015; Zhou et al., 2020). The exact role of Trem2 itself is suggested to be multi-faceted. Some research suggests Trem2, which lacks an intracellular domain, acts as a co-receptor with DAP12 to facilitate downstream signaling (Bouchon et al., 2001; Sessa et al., 2004; Shirotani et al., 2019). This signaling is leads to multiple functions such as increased proliferative capacity, phagocytosis, and antigen presentation (Forabosco et al., 2013; Hsieh et al., 2009; Kawabori et al., 2015; Leyns et al., 2017; Painter et al., 2015; Takahashi et al., 2005; Wang et al., 2015; Zheng et al., 2016; Zhong et al., 2015). Trem2 appears to be a promiscuous receptor, with evidence that it binds to multiple types of anionic molecules (Daws et al., 2003; Kober and Brett, 2017; N'Diaye et al., 2009; Quan et al., 2008). Importantly, these documented anions include fatty acids and lipoproteins (Atagi et al., 2015; Hsieh et al., 2009; Poliani et al., 2015; Shirotani et al., 2019; Yeh et al., 2016), indicating that the Trem2-high NAMs potentially interact with the excess lipid accumulation present in NASH. These interactions and signaling cascades have not yet been linked to the *in vivo* effects of Trem2, but the gene itself was shown to play a major role in physiology.

In the brain, Trem2 is critical for microglial clearance of amyloid plaques in murine Alzheimer's disease models. In genetic mouse models for disease, it was found that microglia increase Trem2 expression and adopt a NAM-like transcriptomic signature (Keren-Shaul et al., 2017; Wang et al., 2015). Consistently, Trem2 mutations in humans have been strongly associated with Alzheimer's disease (Guerreiro et al., 2013; Jonsson et al., 2013). In a whole-body Trem2 knockout mouse (Trem2 KO), murine models for Alzheimer's induction results in increased plaque formation and reduced inflammation from the microglia (Wang et al., 2015; Zhou et al., 2020). One possible mechanism proposed from these studies is that Trem2 seems to be critical for differentiation of the disease-associated macrophage (DAM) population, which highly

resembles our NAMs. In parallel single-cell sequencing studies, it was shown that Trem2 KO reduces the entire DAM transcriptomic signature, including expression of genes such as Gpnmb, Cd9 and Pf4 (Keren-Shaul et al., 2017; Zhou et al., 2020). It would seem that macrophages lacking Trem2 are unable to adopt the full identity of a DAM/NAM. This translating to inability to clear plaques indicates that it is the DAM population which is critical for clearance of debris and dead material. Interestingly, on the metabolic side, DAMs were identified among adipose tissue macrophage populations (Jaitin et al., 2019). The transcriptomic signature of ATMs, just like microglia, adapt a DAM profile in disease. These studies found similarly that in Trem2 KO there is a loss of the DAM profile as macrophages are unable to upregulate Gpnmb and other markers. Phenotypically, it appeared that under high-fat challenge, the adipose tissue in the mice grew larger lipid droplets and the ATMs were unable to form standard crown-like structures, characteristic of macrophage clearance of lipid droplets. This appeared to translate to overall worsened metabolic health through elevated serum cholesterol and insulin resistance. In addition to all this, Trem2 does appear to be active in the liver, as Trem2 KO affected the response to chemical-induced liver injury (Perugorria et al., 2018), wherein the chemical-induced fibrosis was increased. This led us to hypothesize that Trem2 may be potentially important for lipid clearance in the liver as well, and therefore play an important role in maintenance of liver health in the face of NASH.

**Effects of genetic Trem2 knockout in murine NASH model**

To assess the effect of Trem2 on NASH pathogenesis, we placed cohorts of wild type and Trem2 KO mice on Amylin NASH diet for 6 months. Trem2 loss-of-function appeared to have no effect on liver injury, indicated by no significant difference in plasma ALT or AST (Figure 4A). Liver weight was unaffected (Figure 4B), indicating there was unlikely to be a difference in steatosis. Similarly, gonadal adipose pad weight was unaffected (Figure 4C). Liver qPCR showed no major differences in markers for inflammation or fibrosis with genes such as Tnf, Il1b, Col1a1, and Acta2 showing no significant difference (Figure 4D). Interestingly, we did not observe a change in transcription of Gpnmb or Ms4a7, key markers of the NAM transcriptional signature, indicating that the NAM signature is maintained even in the absence of Trem2 in liver. This implies the Trem2 gene is not important for the NAM signature in liver, as it is for DAMs in microglia or ATMs. The mice maintained the same body weights throughout dietary feeding

(Figure 4E) and steatosis was unaffected, as liver triglycerides showed no significant difference in the Trem2 KO mice (Figure 4F). On histology, we similarly observed no significant difference in lipid accumulation or fibrosis as seen on Sirius red stain (Figure 4G). Under Amylin-diet induced NASH, macrophages marked by F4/80 expression appear to localize around lipid droplets similar to crown-like structures in adipose tissue (Figure 4G). This localization was not hindered as we expected, in the absence of Trem2.

Given the lack of observable differences Trem2 KO had on our Amylin diet NASH mouse model studies, we asked if Trem2 plays any role in diet-induced obesity or diabetes. We placed Trem2 KO cohorts on a standard 60% high-fat diet for 4 months to observe these effects. In contrast to the previous publication (Jaitin et al., 2019), we found Trem2 KO had minor effects on our physiologic readouts in diet-induced obesity. Liver injury by plasma ALT and AST was not affected (Figure 5A), and of plasma metabolites such as fatty acids, triglycerides, ketone bodies, and cholesterol were not significantly changed by knockout of Trem2 (Figure 5B-E). In stark contrast to prior work, body weight gain on high-fat diet was not significantly different between wild type control and Trem2 KO mice on a high-fat diet (Figure 5F), and we did not observe a significant difference in insulin sensitivity, assessed by intraperitoneal glucose tolerance and insulin tolerance tests (Figure 5G-H).

**Trem2 regulation of crown-like structure formation in adipose tissue macrophages**

This apparent lack of effects of Trem2 KO in the context of our dietary mouse models for NASH and obesity raised the question of what effect the Trem2 gene itself has on NAM function. As observed previously, Trem2 regulates the localization of ATMs around lipid droplets to create crown-like structures (Jaitin et al., 2019). Interestingly, we also observed these findings on H&E staining in the gonadal fat pad of our high-fat diet-fed mice (Figure 6A). Consistently, Trem2 KO mice were unable to form cellular structures around lipid droplets and they grew larger following high-fat diet challenge (Figure 6B). Also consistent with previous single-cell studies, we observed that the visceral adipose tissue had reduced expression of NAM signature genes including Gpnmb, Ms4a7, and Cd9 by qPCR (Figure 6C), indicating that ATMs were diminished in this transcriptional profile. This confirms that while Trem2 loss of function does not affect the development of NAMs in liver, it seems to be potentially important in the ATM population

during obesity. Correlated with this loss of NAM signature and adipocyte hypertrophy, we found overall increase in the metabolism of these adipocytes by qPCR. Genes involved in lipid droplets, lipid metabolism, and adipokines were significantly increased in these adipose tissue qPCR of Trem2 KO compared to wild type, suggesting that the adipose metabolic health was actually improved in light of this hypertrophy.

There has also been a body of work suggesting that Trem2 may act in an endocrine fashion. The extracellular domain of Trem2 can be cleaved and released into circulation, but whether it has a receptor elsewhere or simply acts as a decoy receptor for itself is unclear (Wu et al., 2015; Wunderlich et al., 2013). A body of research utilizes soluble Trem2 factors as markers for disease progression as well (Deming et al., 2019; Ewers et al., 2019; Zhong et al., 2019). To test if soluble Trem2 has some affect in biology, we produced AAV under the CAG promoter to induce ubiquitous expression of soluble, secreted mouse Trem2. This extracellular domain of Trem2 contained the native signal peptide and was fused with the IgG heavy chain Fc domain to maintain circulating levels of the peptide with reduced clearance (Figure 7A). This method of peptide fusion was used in a previous work, highlighted in Chapter 5 (Zhang et al., 2018). The mice were injected with the virus along with Fc-only AAV controls and placed on Amylin diet or high-fat diet to assess the role of soluble Trem2 on disease progression. We verified that the peptide was secreted in circulation by detecting the correctly sized Fc-fusion proteins on western blot of plasma (Figure 7B). No significant difference was observed for plasma ALT, AST, liver inflammation genes on qPCR, or fibrosis and steatosis by histology, in our Amylin diet cohorts (data not shown). Interestingly, as we had seen an adipose tissue phenotype in the Trem2 KO mice, we expected a difference in this case for high-fat diet mice. However, we did not observe any concordant transcriptional changes on qPCR in the visceral adipose of the mice (Figure 7C). Concurrently, the adipose tissue appeared to be the same size in the mice (Figure 7D). Similarly, we did not observe a difference in lipid droplet size or accumulation of crown-like structures in the adipose (Figure 7E), indicating that soluble Trem2 has minor effects on the function of Trem2 itself, as the phenotype did not match that of the Trem2 KO.

**Discussion**

Overall, these findings suggest that Trem2 is potentially important for some function of the NAM population, particularly in phagocytosis. We confirmed a prior study that in the absence of Trem2, ATMs are unable to form crown-like structures and maintain the size of growing lipid droplets. However, this did not translate to the whole-body metabolic difference the previous study had shown. It is quite possible that our phenotype did not match due to using different mouse lines for Trem2 KO (Kang et al., 2018; Wang et al., 2015). Although both lines are whole-body knockout, the method of knockout differs between the two mice. The group that identified a knockout utilized a frameshift in exons 3 and 4 that still results in some of the Trem2 protein being produced, which may confer some accessory function of unknown nature. Our Trem2 KO model utilized CRISPR to induce an early stop codon at residue 17 within the signal peptide sequence. Regardless of the mouse model, based on our own results, we conjecture that the Trem2 gene itself is important for some facets of NAM function, particularly phagocytosis. However, Trem2 itself may not be the only gene in regulating NAM function. Future studies on targeted ablation of the entire cell population will be more informative in studying the role of NAMs in disease. In future studies, we will cross our Trem2Cre model with diphtheria toxin receptor models to assess ablation of the entire cell population (Buch et al., 2005). By assessing the function of the cells as a whole, we can begin to elicit their role in disease. Furthermore, further in the future we may cross Trem2 Cre lines with other floxed genes in order to target pathways such as lipolysis and phagocytosis in the NAM population, thus dissecting the mechanism through which they carry out their role in disease.

It also seems that Trem2 is important for the differentiation of NAMs and the acquisition of a specific transcriptional profile. While we confirmed this in the gonadal adipose tissue following a high-fat diet, we interestingly did not observe this in the NASH liver. The regulation of the NAM profile and development from hematopoietic monocytes remains poorly resolved. Future *in vitro* studies can begin to clarify what signals mediate the development of NAMs, whether it is signals from damaged hepatocytes, cytokines or stellakines, or lipid droplets, we may now focus our studies on bone-marrow-derived macrophages. As it appears Trem2 positive macrophages are present in any tissue, there is likely some universal signal throughout the body that mediates their appearance. Furthermore, it is unclear when in the development of NAMs they gain their

signature profile of genes such as Gpnmb and Cd9. Our tdTomato mouse results indicate that it is not necessarily a set trajectory, as some Gpnmb-positive macrophages appear in acute injury without Trem2, indicating that some of the other genes may express before Trem2. Likewise, many Trem2 macrophages appear in injury without the other NAM genes. However, it is irresponsible to conclude these macrophages are Trem2-positive at the time of the injury, as our mouse model will have tdTomato signal if Trem2Cre expressed at any time in that cell's development, including in its original progenitors or during development. Our present findings in the liver only allow us to conclude that Trem2 is a marker for the NAM population. Lineage tracing studies with our Trem2Cre tdTomato model will help to elucidate the trajectory of these cells. Because Trem2 Cre has the caveat of expressing and recombining at any point in developmental trajectory, generating an inducible Cre-ERT system under the Trem2 promoter may help to pinpoint the period during development during which Trem2 actually expresses. We conclude that many questions still exist about this ubiquitous cell population that is clearly associated with disease. While Trem2 is the strongest correlated marker of this population, the function of the protein itself may not be as significant as we originally thought in the liver. More work will be needed to elucidate the true function of the protein. Further, our focus will remain on the cell population itself, not just one gene. We have developed novel and powerful mouse models that will begin to address these questions not just in liver disease, but in other systems as well including brain and adipose.

**Methods**

Mice

All animal studies were performed following procedures approved by the Institutional Animal Care & Use Committee at the University of Michigan. Mice were housed in pathogen-free facilities under 12-h light-dark cycles with free access to food and water. For standard chow feeding, mice were fed Teklad 5001 Laboratory Diet. For AMLN diet-induced NASH, C57/Bl6 mice were fed a diet containing 40% fat (of which 18% was trans-fat), 22% fructose, and 2% cholesterol (D09100301, Research Diets Inc.) for 20 weeks, as previously described (Clapper et al., 2013; Guo et al., 2017). In a separate diet-induced NASH model, C57/Bl6 mice were maintained on Choline-Deficient, Amino acid-defined HFD (45 kcal% fat) containing 0.1% methionine (CDAHFD, A06071309, Research Diets Inc.) for 6 weeks. For HFD feeding, mice

were fed a diet containing 60% of calories from fat (D12492, Research Diets). For carbon tetrachloride injury, mice were injected 2 uL/g with mineral oil for sham or 2 uL/g with 1:1 CCl4 (Fisher AC148170025) with mineral oil. For AAV studies, mice were tail-vein injected for virus induction at 8 weeks, dietary challenge was initiated at 10 weeks and HFD maintained for 12 weeks.

Data analysis

For total liver and RNA-seq, sequence reads were mapped to mouse genome mm10 using STAR. HTSeq was used to count the sequences that can be mapped to gene features. The raw read counts were normalized and processed for differential expression gene analysis using DESeq2. The significant expressed genes were determined by FDR less than 0.05. All RNA-seq data generated in this work have been deposited into the Gene Expression Omnibus (GEO) database (GSE119340, GSE129516).

Generation of mouse lines

Trem2Cre mouse line was generously created in the University of Michigan Diabetes Research Centers center for molecular genetics. Cre sequence was inserted by homologous recombination following exon 4 in after the stop sequence in exon 5, along with a P2A cleavage site.

Mouse genotyping

For genotyping, mouse ear snips were dissolved in 150 mM sodium hydroxide at 98C for 30 minutes before buffering with 100 mM Tris-HCl pH 7.5 (Invitrogen 15567027). Dissolved genomic DNA was reacted in PCR to assess for amplification. Trem2 KO primers include 5' TCA GGG AGT CAG TCA TTA ACC A, 3' wt AGT GCT TCA AGG CGT CAT AAG T, and 3' mutant knockout CAA TAA GAC CTG GCA CAA GGA. Trem2Cre forward and reverse primers are gcaggtttcatcctgtgggtc and AGACGGAAATCCATCGCTCG. For tdTomato flox, wild type primers are AAG GGA GCT GCA GTG GAG TA and CCG AAA ATC TGT GGG AAG TC. Mutant primers are GGC ATT AAA GCA GCG TAT CC and CTG TTC CTG TAC GGC ATG G.

Measurement of plasma parameters

Liver TAG was measured as described previously (Li et al., 2008; Meng et al., 2017). Plasma concentrations of ALT, AST, TAG, cholesterol, ketone, and NEFA were measured using commercial assay kits (Stanbio Laboratory). Mice were fasted overnight 16h for GTT or 4h for ITT and injected intraperitoneally with 1 g/kg of glucose or 1.2U/kg insulin respectively. Glucose measurements were taken with glucometer at time points.

Generation of AAV Trem2-Fc and Fc

The Trem2-Fc fusion construct contains an N-terminal signal peptide from native Trem2 followed by the extracellular domain of mouse Trem2 (amino acids 1-157 of mTREM2), a glycine-serine linker and human IgG1 Fc fragment (Fig. 7A). The construct cloned from mouse cDNA into an IgG1 Fc backbone which was synthesized by GeneArt (Thermo Fisher Scientific) and sub-cloned into pcDNA3 expression vector. For Fc fusion protein production, the same backbone was used with no Trem2 cDNA. For AAV8 transduction, Trem2-Fc and Fc constructs were cloned into AAV8 shuttle vector. Shuttle vector was co-transfected at 70 ug with 70 ug of RC2/9 plasmid and 200 ug of DF6 helper plasmid, under 2.5 mL PEI transfection in 30 25-cm plates of 293T cells. Cells were harvested 3 days post-transfection and virus was purified in 17/25/40/60% optiprep gradient ultracentrifugation. Briefly, cells were lysed by 3 cycles of freeze thaw in 5 mL of 150 mM NaCl, 20 mM Tris pH8.0 buffer. Lysate was supplemented with 5 uL of 1M MgCl2 and 5 ul 25KU/ml Benzonase (Sigma E8263-25KU). After incubating 37C for 30 minutes, lysate was spun 4000 rpm for 30 min at 4C, supernatant was placed on top of ultracentrifuge tube with 5 mL each layer of gradient, in 25 mM KCl, 100 mM MgCl2, and PBS in the noted Optiprep densities. Tubes were spun 2h40min at 53000 rpm at 14C, 40% layer was collected for virus and purified in 100K centrifugal filter in PBS, spinning 3500 rpm 5 min 3 times. AAV8-Fc or AAV8–mTrem2-Fc ($1 \times 10^{12}$ genome copies/mouse) was delivered by tail vein injection.

RNA extraction and analysis

Total RNA was extracted from frozen livers or adipose using Trizol (Alkali Scientific, TRZ-100). Quantitative RT-PCR gene expression analysis was performed as previously described (Guo et al., 2017; Wang et al., 2014). Liver RNA sequencing was performed using Illumina HiSeq 4000 at the University of Michigan DNA Sequencing Core.

Flow cytometry

Hepatic NPC were collected as previously described. The isolated cells were centrifuged at 1,000 rpm for 5 min. The cells were washed and re-suspended in cold staining buffer, followed by incubation with anti-CD16/CD32 antibody to block Fc receptors. For hepatic macrophages, liver samples were filtered through 100 um strainers in 1% BSA in PBS and centrifuged at 50x g for 3 minutes to remove hepatocytes. NPC were harvested as intermediate fraction following gradient centrifugation in 25% optiprep at 1500x g for 20 minutes. For stromal-vascular fraction of adipose tissue, adipose was minced briefly and immersed in 1 mL of 2 mg/mL collagenase 1 with 0.1 mg/mL DNaseI at 37C for 20 minutes with periodic agitation. 25 mL of cold 10% FBS was added, cell suspension was filtered through a 70 um strainer and spun at 500g for 12 min at 4C, washing once with 1% BSA. Cells were then treated with 0.8% NH4Cl for 5 minutes to lyse red blood cells. After wash, $1 \times 10^6$ cells were incubated with 100 ul of various antibodies diluted at optimal concentrations for 20 min at 4 °C. The fluorochrome-conjugated antibodies against CD45 (30-F1; Biolegend, 103130) F4/80 (BM8; Biolegend, 123114), CD11b (M1/80; Biolegend, 101226), CD9 (MZ3; Biolegend, 124805), GPNMB (CSTREVL; Thermo Fisher, 50-5708-82) liver macrophages were gated as CD45+F4/80hiCD11bint or CD45+F4/80intCD11bhi for KC or MDM, respectively. For intracellular staining, the cells were fixed and permeabilized by BD Cytofix/Cytoperm Fixation/Permeabilization Kit per manufacturer's protocol. Samples were analyzed using BD LSR cell analyzer at the Vision Research Core Facility at the University of Michigan Medical School. Data were analyzed using the CellQuest software (BD Biosciences) and Flowjo (Flowjo.com).

Bone-marrow transplant

Bone marrow cells were acquired from the femurs of donor (45.1) with Hank's buffered salt solution without calcium or magnesium, supplemented with 2% heat-inactivated calf serum (HBSS; Invitrogen). Cells were triturated and filtered through nylon screen (70 mm; Sefar America) to obtain a single-cell suspension. Recipient B6 mice (CD45.2) were irradiated in an Orthovoltage X-ray source delivering 300 rad min−1 in two equal doses of 540 rad, delivered 2 h apart. Cells were injected into intravenously through the tail. 6 weeks post-transplant blood was obtained from the tail veins of recipient mice, subject to ammonium-chloride potassium red cell

lysis, and stained to monitor engraftment with CD45.2 (104), CD45.1 (A20), Cd11b (M1/80), Gr-1 (8C5).

Immunofluorescence staining and histochemical studies

Liver tissues were fixed in situ with 4% paraformaldehyde, incubated with 30% sucrose in PBS overnight, and embedded in OCT. Frozen sections were permeabilized with 0.3% Triton X-100 in PBS and then blocked in 5% BSA, followed by incubation in primary antibody (F4/80 BioRad MCA497G, H2Ab1 eBio 114.15.2, Desmin Thermo RB-9014-P) solution overnight at 4 °C, and subsequently in secondary antibody solution at room temperature for one hour. Sections were mounted in VECTASHIELD Antifade Mounting Medium (Vector Laboratories, H-1000). Images were taken with Olympus fluorescence microscope. All H&E stains and paraffin embedding were performed at the University of Michigan tissue histology core. For adipose tissue stains, adipose tissue was directly immersed in 5% BSA PBS for 30 minutes prior to addition of primary antibody at room temperature for 1hr. Tissue were then washed 3 times 10 minutes in PBS before immersion in secondary antibody. After repeated wash tissue was immersed in DAPI before mounting on slides for visualization. For Sirius red stain, sections were rehydrated, stained in Picro-Sirius red solution (CI 35782) for 1 hour, washed in 1:200 glacial acetic acid in water, and dehydrated. For whole-mount staining, 1 cubic cm of adipose tissue was directly blocked in 5% BSA in PBS for 30 minutes at room temperature before immersion in x200 primary F4/80 antibody, washed 3 times in PBS for 10 minutes before immersion in x200 secondary antibody, repeated wash and immersed in DAPI before imaging directly.

Western Blot Analysis

Mouse plasma was diluted using a lysis buffer containing 50 mM Tris-HCl (pH = 7.5), 137 mM NaCl, 1 mM EDTA, 1% Triton X-100, 10% glycerol, 10 mM NaF, 10 mM Na4P2O7, 1 mM Na3VO4, and protease inhibitor cocktail. The lysates were separated by SDS-PAGE and transferred to a PVDF membrane, followed by immunoblotting with primary antibodies for human IgG (Thermo 31410).

Statistics

Statistical analysis was performed using GraphPad Prism 7. Statistical differences were evaluated using two-tailed unpaired Student's t-test or one-way analysis of variance (ANOVA) between test groups as indicated in figure legends. P value less than 0.05 (*p < 0.05) was considered statistically significant.
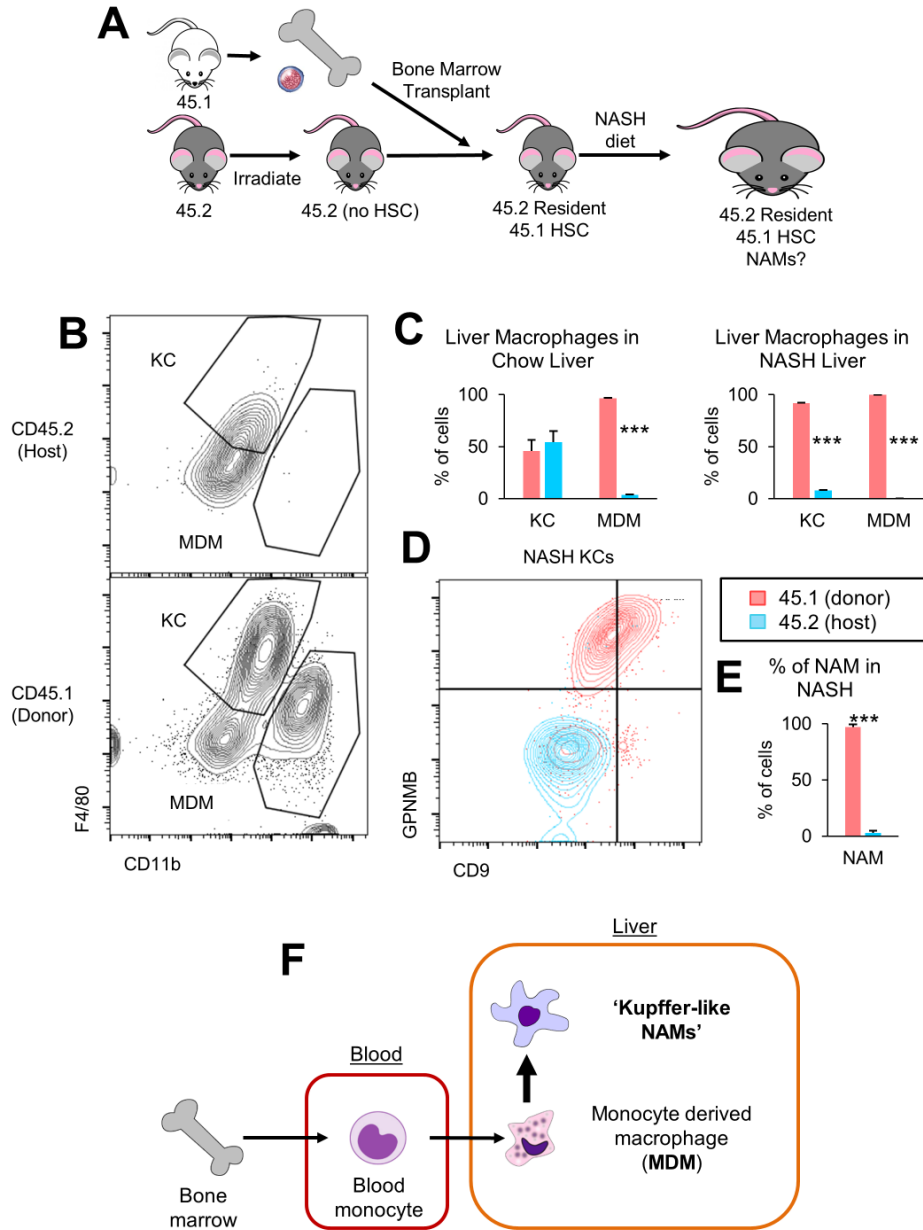
**Figure 3.1 Liver Trem2 expressing macrophages originate from hematopoietic sources**
(A) Schematic of bone marrow transplant study to trace Trem2 macrophage origins in NASH.

91

(B) Flow cytometry plots mapping CD45.2+ (top) and CD45.1+ (bottom) macrophages from NASH recipient mice following 6 weeks of CDA HFD. KC labeled as F4/80hiCD11bint MDM labeled as CD11bhi populations.
(C) Quantification of contributions to total KC and MDM pools from CD45.1 and CD45.2 populations for chow and NASH mice (n=3).
(D) Flow cytometry representative plot comparing GPNMB CD9 expression in CD45.1+F4/80hiCD11bint KCs with CD45.2+F4/80hiCD11bint KCs of transplant recipient mice following CDA HFD.
(E) Quantification for mice in (D) (n=3).
(F) Diagram highlighting proposed pathway for development of Trem2 macrophages.
Data represents mean ± SEM. *p<0.05, **p<0.01, ***p<0.001 vs. chow; two-tailed unpaired Student's t-test.
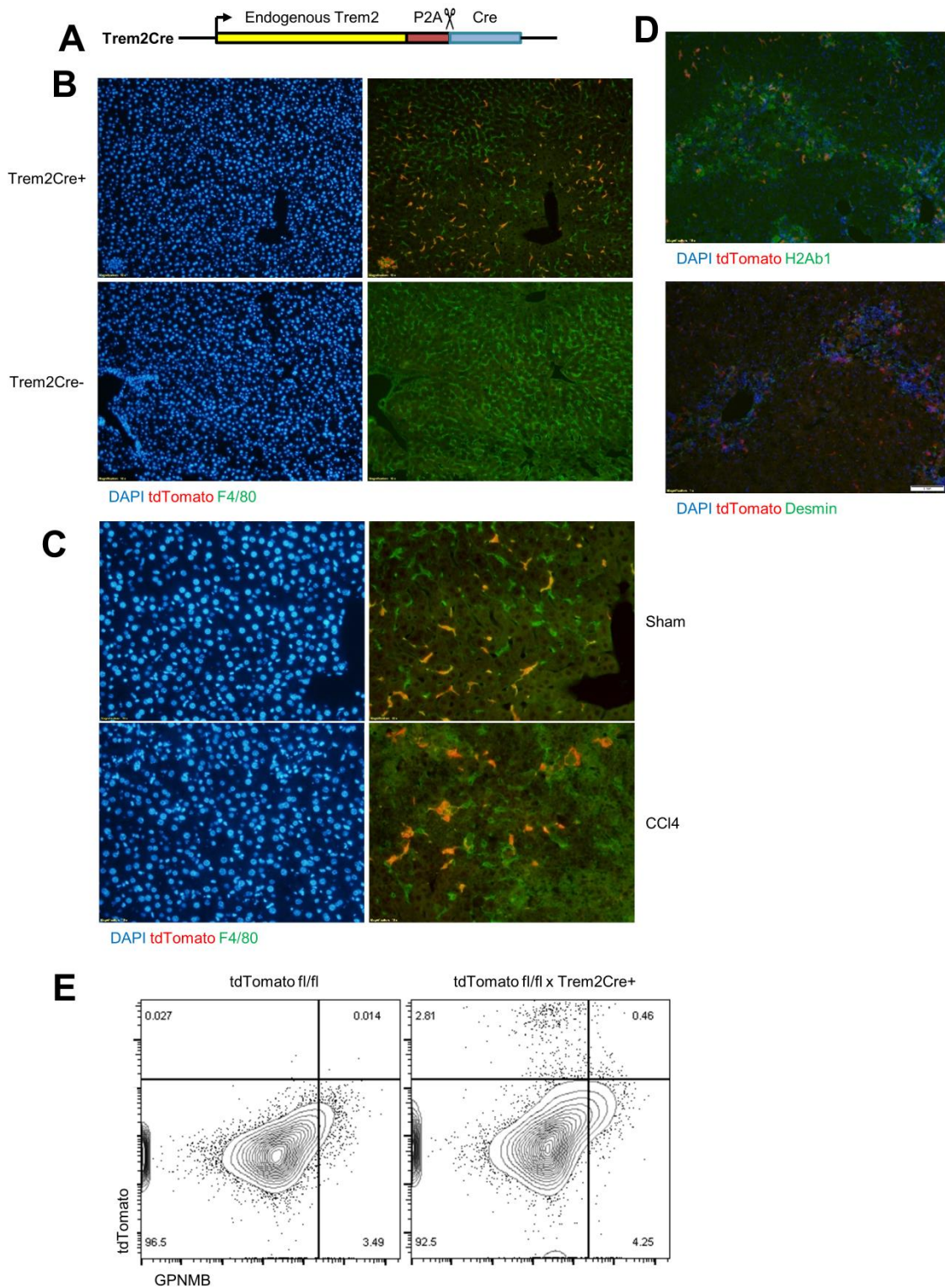
**Figure 3.2 Endogenous Trem2 Cre marks injury-associated Kupffer-like populations in liver**
(A) Diagram of Trem2Cre knock-in model with P2A cleavage following endogenous Trem2 gene.
(B) Immunofluorescence imaging of frozen liver sections with DAPI signal on left, overlay of F4/80 stained in FITC and tdTomato signal on right for liver sections of indicated mice in tdTomato flox background. Magnification 20x.

(C) Liver frozen section immunofluorescence of Trem2Cre positive tdTomato flox mice from (B) following 48 hours of acute CCl4 injury or sham oil treatment. Magnification 40x.

(D) Immunofluorescence images of liver from (C) treated with CCl4, with FITC channel indicated as stained for H2ab1 (top) or Desmin (bottom) overlaid with tdTomato signal and DAPI. Magnification 20x.

 (E) Flow cytometry plot of CD45+F4/80hiCD11bint KCs from mouse livers in (B), assessing tdTomato fluorescence against GPNMB expression. Relative proportion of parent populations shown.

**A** Kidney Pancreas Brain Quad Heart Lung Jejunum Colon BAT

tdTomato F4/80

**B** eWAT iWAT

tdTomato F4/80

**C**

tdTomato fl/fl        tdTomato fl/fl x Trem2Cre+
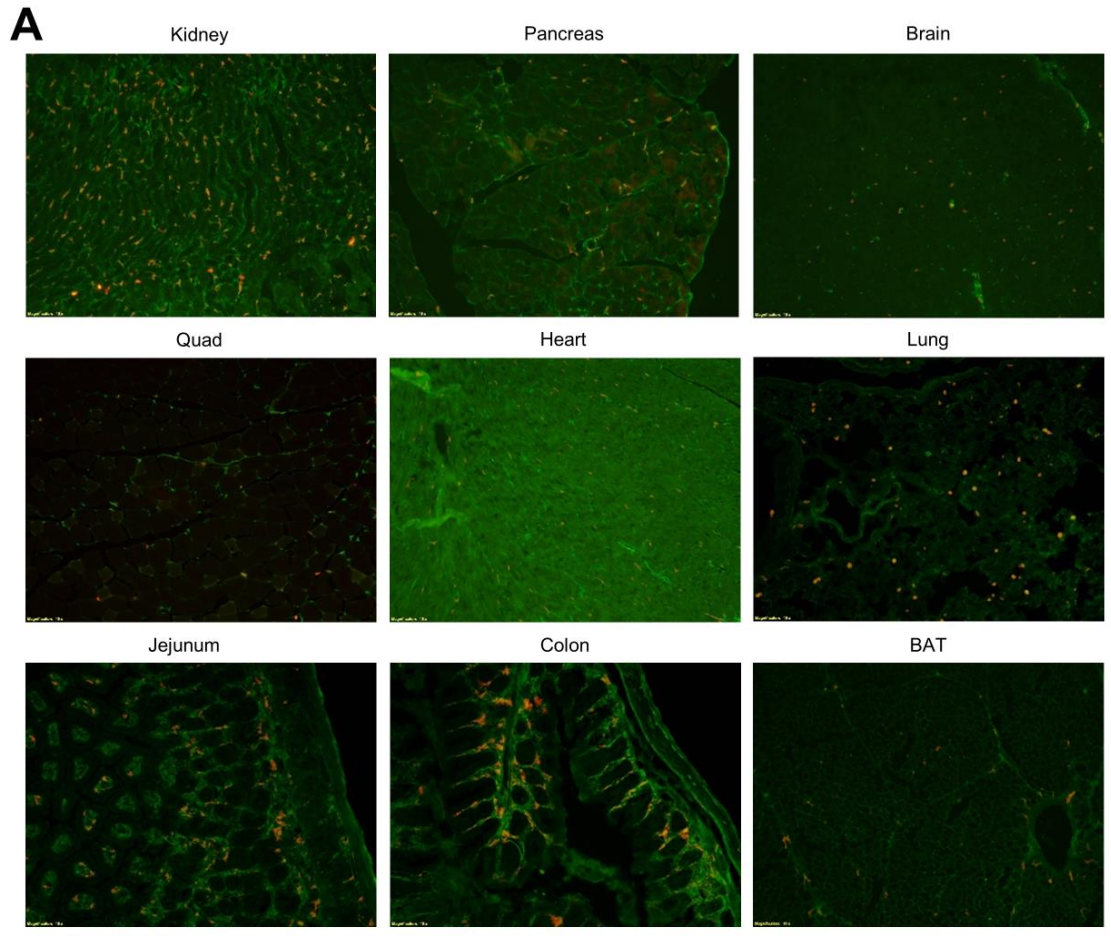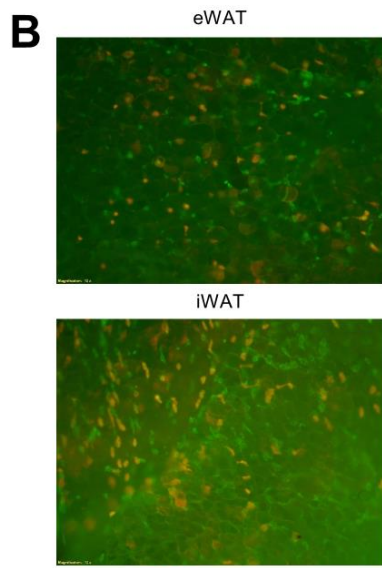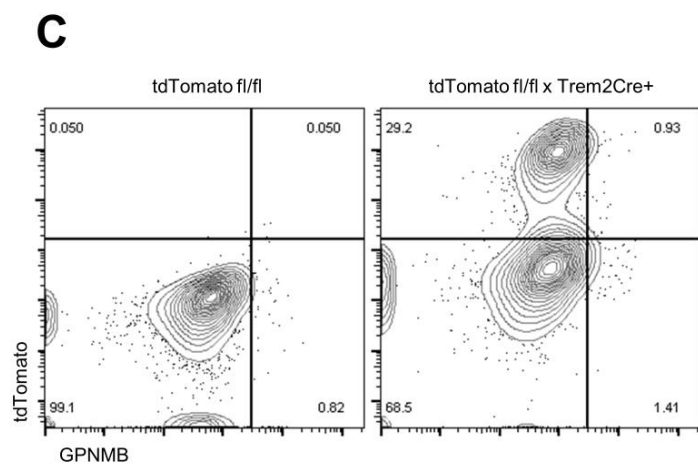
**Figure 3.3 Tissue profiling of Trem2Cre reveals ubiquitous distribution of Trem2 macrophages throughout body**

95

(A) Immunofluorescence imaging of frozen tissue sections with overlay of F4/80 stained in FITC and tdTomato signal for mice in Trem2Cre tdTomato flox background, of tissue indicated on top. Magnification 20x. BAT brown adipose tissue.

(B) Whole-mount staining images of indicated adipose tissue with overlay of F4/80 stained in FITC and tdTomato signal for mice in Trem2Cre tdTomato flox background, of tissue indicated on top. Magnification 40x. iWAT inguinal white adipose tissue, eWAT epididymal white adipose tissue.

(C) Flow cytometry plot of CD45+F4/80hiCD11bhi adipose tissue macrophages from inguinal subcutaneous fat stromal vascular fractions of indicated mice in (B), assessing tdTomato fluorescence against GPNMB expression. Relative proportion of parent populations shown.
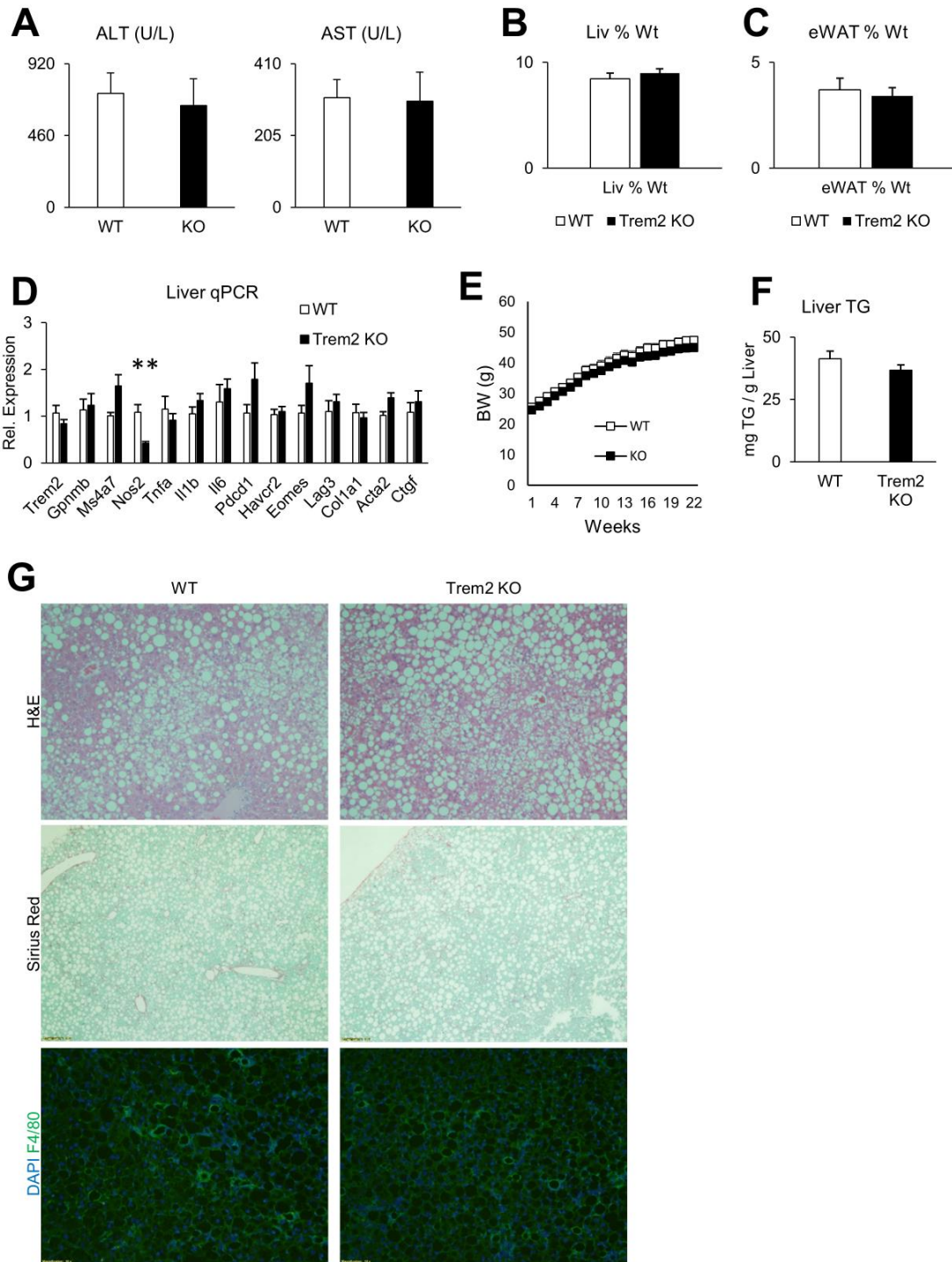
**Figure 3.4 In vivo effects of Trem2 on diet-induced NASH pathogenesis**

(A) Plasma ALT (left) and AST (right) levels in Amylin-diet fed mice following 24 weeks of dietary challenge comparing age-matched male wild type WT (n=9) to Trem2 knockout KO (n=12), dissected during *ad lib* conditions.
(B) Liver weight as proportion of total body weight of mice in (A).
(C) Gonadal visceral fat weight as proportion of total body weight of mice in (A).
(D) Whole-liver qPCR for indicated genes of mice in (A).
(E) Body weight growth of mice in (A) through course of dietary challenge.
(F) Liver triglyceride content of mice in (A).
(G) Representative H&E staining, Sirius Red staining of paraffin-embedded liver sections, and immunofluorescence staining of frozen liver sections, overlaying DAPI with F4/80 in FITC, of liver from mice in (A). Representative image, magnification 20x.
Data represents mean ± SEM. *p<0.05, **p<0.01, ***p<0.001 vs. chow; two-tailed unpaired Student's t-test.
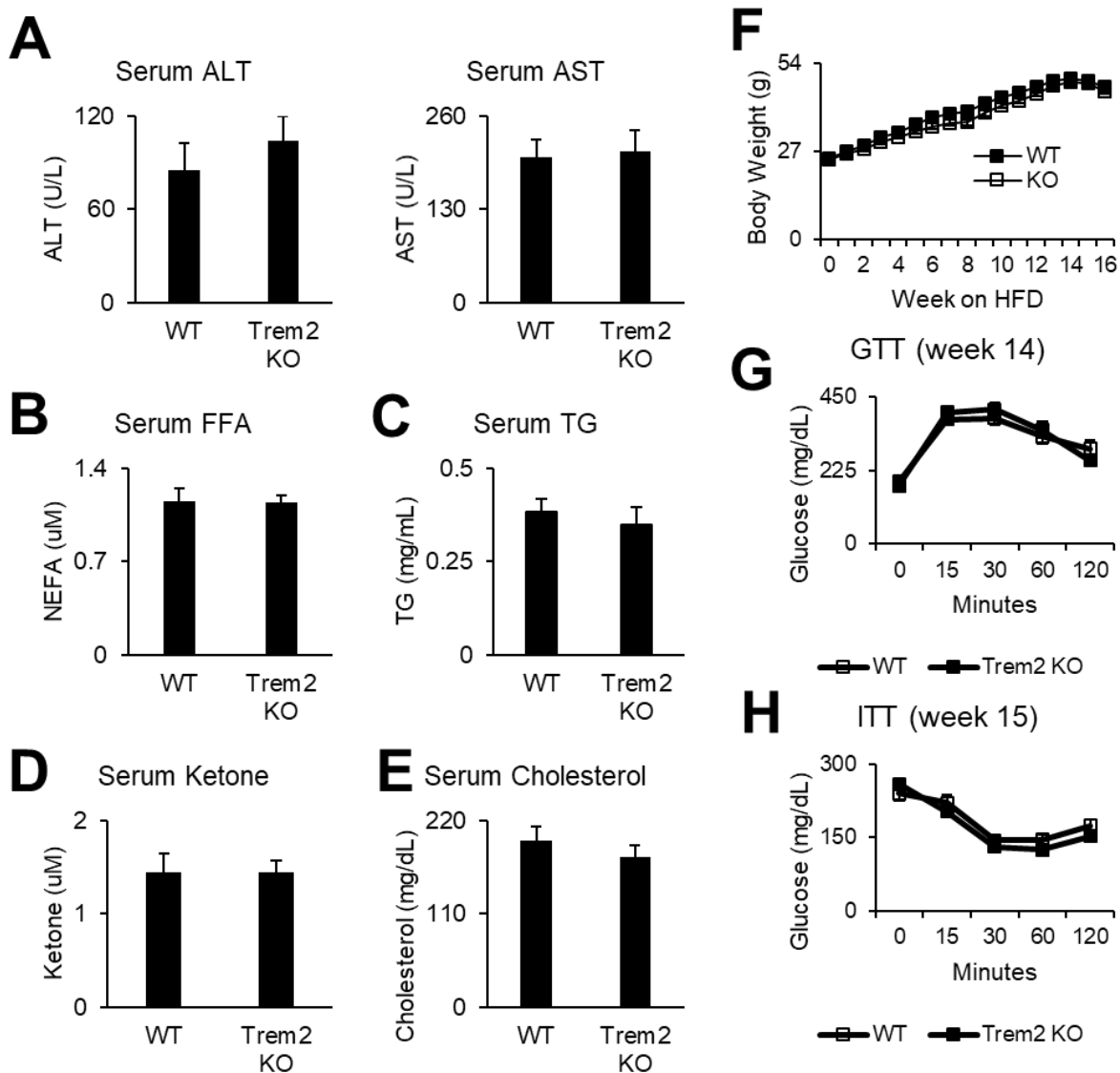
**Figure 3.5 Trem2 KO effects on peripheral whole-body metabolism in diet-induced obesity**
(A) Plasma ALT (left) and AST (right) levels in overnight fasted high-fat diet fed mice following 16 weeks of dietary challenge comparing age-matched male wild type WT (n=10) to Trem2 knockout KO (n=11).
(B) Plasma free fatty acid of mice in (A) measured by kit.
(C) Plasma triglycerides of mice in (A) measured by kit.
(D) Plasma ketone bodies of mice in (A) measured by kit.
(E) Plasma cholesterol levels of mice in (A) measured by kit.
(F) Body weight growth of mice in (A) through course of dietary challenge.
(G) Intraperitoneal glucose tolerance test of mice in (A) at 14 weeks of dietary challenge. Mice were overnight-fasted and injected intraperitoneally with 1 g/kg glucose in PBS and monitored for glucose by tail blood. Data for (G-H) represent mean $\pm$ SE and were analyzed using one-way ANOVA. *$p<0.05$, ** $p<0.01$, *** $p<0.001$.
(H) Intraperitoneal insulin tolerance test of mice in (A) at 15 weeks of dietary challenge. Mice were fasted 4 hours and injected intraperitoneally with 1.2 U/kg insulin in PBS and monitored for glucose by tail blood.
Data for (A-F) represents mean $\pm$ SEM. *$p<0.05$, **$p<0.01$, ***$p<0.001$ vs. chow; two-tailed unpaired Student's t-test.
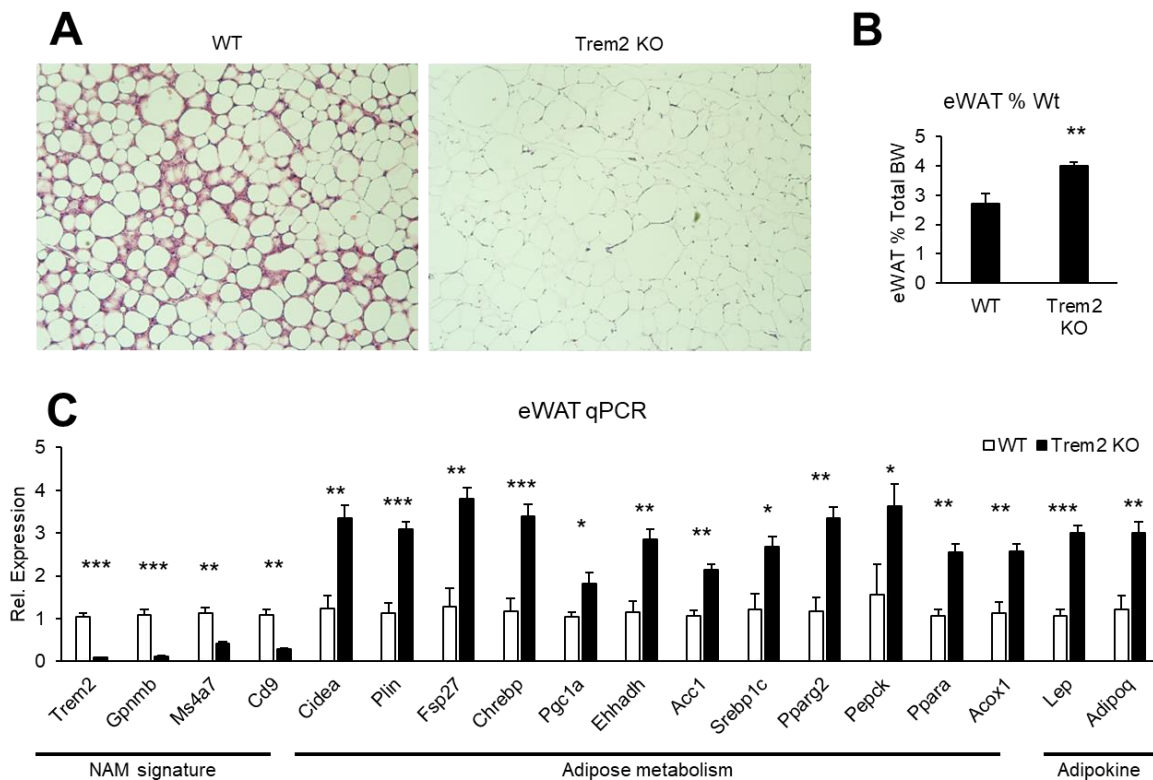
**Figure 3.6 Regulation of adipose tissue macrophage crown-like structure formation by Trem2**
(A) Representative H&E staining of epididymis visceral adipose tissue from overnight fasted high-fat diet fed mice following 16 weeks of dietary challenge comparing age-matched male wild type WT (n=10) to Trem2 knockout KO (n=11). Magnification 20x.
(B) Gonadal visceral fat weight as proportion of total body weight of mice in (A).
(C) Whole-adipose qPCR from epididymis depot for indicated genes of mice in (A).
Data for (B-C) represents mean ± SEM. *p<0.05, **p<0.01, ***p<0.001 vs. chow; two-tailed unpaired Student's t-test.
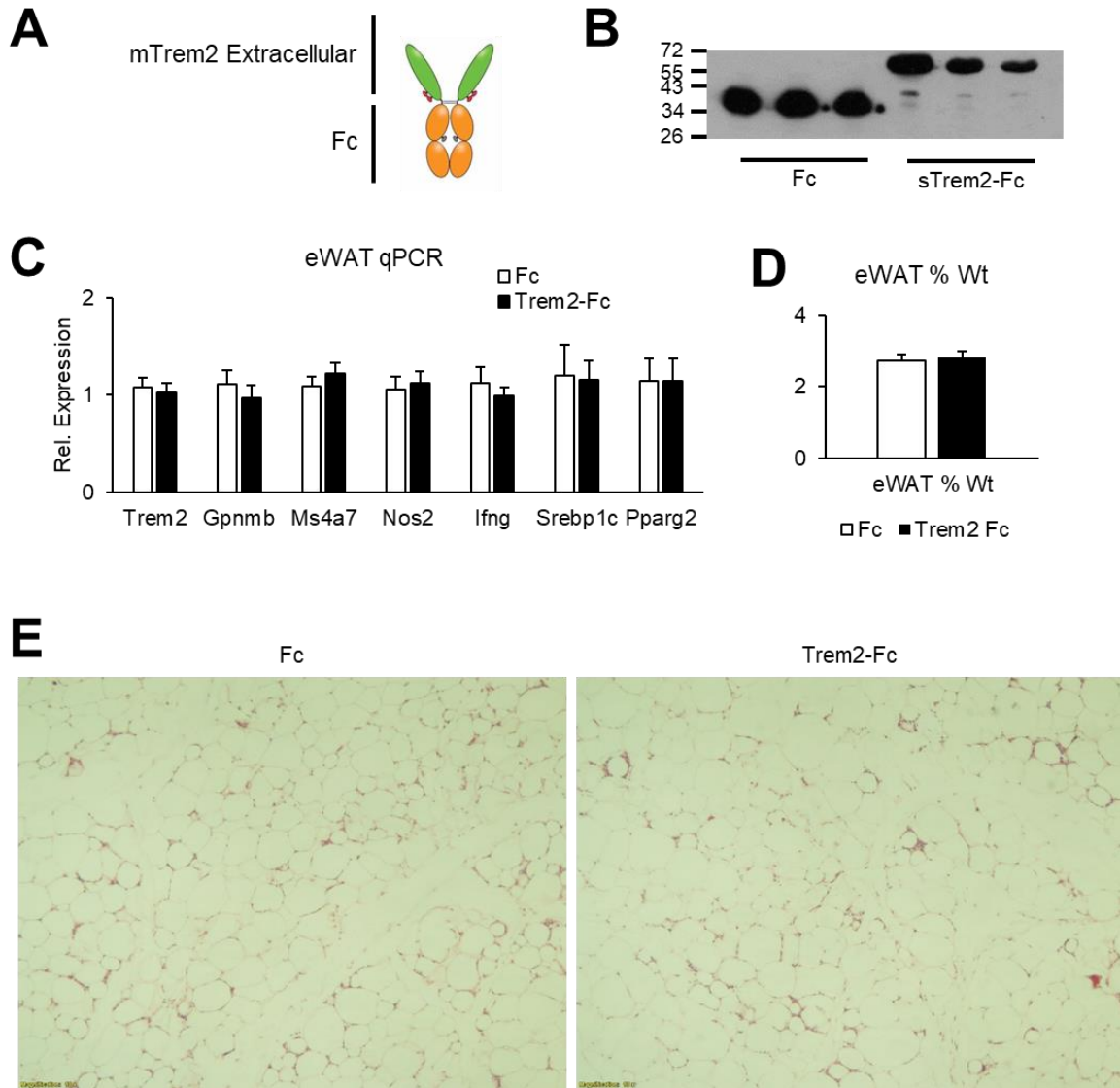
**Figure 3.7 Effects of soluble Trem2 in circulation on peripheral metabolism in diet-induced obesity**
(A) Diagram of soluble mTrem2-Fc construct overexpressed by AAV system.
(B) Representative western blot (n=3) against human IgG Fc fragment of cardiac-puncture plasma from mice at time of dissection following 12 week course of high-fat diet. Mice were induced with indicated virus for Fc (n=10) or sTrem2-Fc (n=10) at 8 weeks and initiated on diet at 10 weeks, overnight fasted before harvest.
(C) Whole-adipose qPCR from epididymis depot for indicated genes of mice in (B).
(D) Gonadal visceral fat weight as proportion of total body weight of mice in (B).
(E) Representative H&E staining of epididymis visceral adipose tissue from mice in (B). Magnification 20x.
Data for (C-D) represents mean ± SEM. *$p<0.05$, **$p<0.01$, ***$p<0.001$ vs. chow; two-tailed unpaired Student's t-test.

# References

Atagi, Y., Liu, C.C., Painter, M.M., Chen, X.F., Verbeeck, C., Zheng, H., Li, X., Rademakers, R., Kang, S.S., Xu, H., et al. (2015). Apolipoprotein E Is a Ligand for Triggering Receptor Expressed on Myeloid Cells 2 (TREM2). J Biol Chem 290, 26043-26050.

Beattie, L., Sawtell, A., Mann, J., Frame, T.C.M., Teal, B., de Labastida Rivera, F., Brown, N., Walwyn-Brown, K., Moore, J.W.J., MacDonald, S., et al. (2016). Bone marrow-derived and resident liver macrophages display unique transcriptomic signatures but similar biological functions. J Hepatol 65, 758-768.

Bouchon, A., Hernandez-Munain, C., Cella, M., and Colonna, M. (2001). A DAP12-mediated pathway regulates expression of CC chemokine receptor 7 and maturation of human dendritic cells. J Exp Med 194, 1111-1122.

Buch, T., Heppner, F.L., Tertilt, C., Heinen, T.J., Kremer, M., Wunderlich, F.T., Jung, S., and Waisman, A. (2005). A Cre-inducible diphtheria toxin receptor mediates cell lineage ablation after toxin administration. Nat Methods 2, 419-426.

Clapper, J.R., Hendricks, M.D., Gu, G., Wittmer, C., Dolman, C.S., Herich, J., Athanacio, J., Villescaz, C., Ghosh, S.S., Heilig, J.S., et al. (2013). Diet-induced mouse model of fatty liver disease and nonalcoholic steatohepatitis reflecting clinical disease progression and methods of assessment. Am J Physiol Gastrointest Liver Physiol 305, G483-495.

Daws, M.R., Sullam, P.M., Niemi, E.C., Chen, T.T., Tchao, N.K., and Seaman, W.E. (2003). Pattern recognition by TREM-2: binding of anionic ligands. J Immunol 171, 594-599.

Deming, Y., Filipello, F., Cignarella, F., Cantoni, C., Hsu, S., Mikesell, R., Li, Z., Del-Aguila, J.L., Dube, U., Farias, F.G., et al. (2019). The MS4A gene cluster is a key modulator of soluble TREM2 and Alzheimer's disease risk. Sci Transl Med 11.

Ewers, M., Franzmeier, N., Suarez-Calvet, M., Morenas-Rodriguez, E., Caballero, M.A.A., Kleinberger, G., Piccio, L., Cruchaga, C., Deming, Y., Dichgans, M., et al. (2019). Increased soluble TREM2 in cerebrospinal fluid is associated with reduced cognitive and clinical decline in Alzheimer's disease. Sci Transl Med 11.

Forabosco, P., Ramasamy, A., Trabzuni, D., Walker, R., Smith, C., Bras, J., Levine, A.P., Hardy, J., Pocock, J.M., Guerreiro, R., et al. (2013). Insights into TREM2 biology by network analysis of human brain gene expression data. Neurobiol Aging 34, 2699-2714.

Gomez Perdiguero, E., Klapproth, K., Schulz, C., Busch, K., Azzoni, E., Crozet, L., Garner, H., Trouillet, C., de Bruijn, M.F., Geissmann, F., et al. (2015). Tissue-resident macrophages originate from yolk-sac-derived erythro-myeloid progenitors. Nature 518, 547-551.

Guerreiro, R., Wojtas, A., Bras, J., Carrasquillo, M., Rogaeva, E., Majounie, E., Cruchaga, C., Sassi, C., Kauwe, J.S., Younkin, S., et al. (2013). TREM2 variants in Alzheimer's disease. N Engl J Med 368, 117-127.

Guo, L., Zhang, P., Chen, Z., Xia, H., Li, S., Zhang, Y., Kobberup, S., Zou, W., and Lin, J.D. (2017). Hepatic neuregulin 4 signaling defines an endocrine checkpoint for steatosis-to-NASH progression. J Clin Invest 127, 4449-4461.

Hsieh, C.L., Koike, M., Spusta, S.C., Niemi, E.C., Yenari, M., Nakamura, M.C., and Seaman, W.E. (2009). A role for TREM2 ligands in the phagocytosis of apoptotic neuronal cells by microglia. J Neurochem 109, 1144-1156.

Italiani, P., and Boraschi, D. (2014). From Monocytes to M1/M2 Macrophages: Phenotypical vs. Functional Differentiation. Front Immunol 5, 514.

Jaitin, D.A., Adlung, L., Thaiss, C.A., Weiner, A., Li, B., Descamps, H., Lundgren, P., Bleriot, C., Liu, Z., Deczkowska, A., et al. (2019). Lipid-Associated Macrophages Control Metabolic Homeostasis in a Trem2-Dependent Manner. Cell 178, 686-698 e614.

Jakubzick, C.V., Randolph, G.J., and Henson, P.M. (2017). Monocyte differentiation and antigen-presenting functions. Nat Rev Immunol 17, 349-362.

Jonsson, T., Stefansson, H., Steinberg, S., Jonsdottir, I., Jonsson, P.V., Snaedal, J., Bjornsson, S., Huttenlocher, J., Levey, A.I., Lah, J.J., et al. (2013). Variant of TREM2 associated with the risk of Alzheimer's disease. N Engl J Med 368, 107-116.

Kang, S.S., Kurti, A., Baker, K.E., Liu, C.C., Colonna, M., Ulrich, J.D., Holtzman, D.M., Bu, G., and Fryer, J.D. (2018). Behavioral and transcriptomic analysis of Trem2-null mice: not all knockout mice are created equal. Hum Mol Genet 27, 211-223.

Kawabori, M., Kacimi, R., Kauppinen, T., Calosing, C., Kim, J.Y., Hsieh, C.L., Nakamura, M.C., and Yenari, M.A. (2015). Triggering receptor expressed on myeloid cells 2 (TREM2) deficiency attenuates phagocytic activities of microglia and exacerbates ischemic damage in experimental stroke. J Neurosci 35, 3384-3396.

Keren-Shaul, H., Spinrad, A., Weiner, A., Matcovitch-Natan, O., Dvir-Szternfeld, R., Ulland, T.K., David, E., Baruch, K., Lara-Astaiso, D., Toth, B., et al. (2017). A Unique Microglia Type Associated with Restricting Development of Alzheimer's Disease. Cell 169, 1276-1290 e1217.

Kober, D.L., and Brett, T.J. (2017). TREM2-Ligand Interactions in Health and Disease. J Mol Biol 429, 1607-1629.

Leyns, C.E.G., Ulrich, J.D., Finn, M.B., Stewart, F.R., Koscal, L.J., Remolina Serrano, J., Robinson, G.O., Anderson, E., Colonna, M., and Holtzman, D.M. (2017). TREM2 deficiency attenuates neuroinflammation and protects against neurodegeneration in a mouse model of tauopathy. Proc Natl Acad Sci U S A 114, 11524-11529.

Li, S., Liu, C., Li, N., Hao, T., Han, T., Hill, D.E., Vidal, M., and Lin, J.D. (2008). Genome-wide coactivation analysis of PGC-1alpha identifies BAF60a as a regulator of hepatic lipid metabolism. Cell Metab 8, 105-117.

Meng, Z.X., Gong, J., Chen, Z., Sun, J., Xiao, Y., Wang, L., Li, Y., Liu, J., Xu, X.Z.S., and Lin, J.D. (2017). Glucose Sensing by Skeletal Myocytes Couples Nutrient Signaling to Systemic Homeostasis. Mol Cell 66, 332-344 e334.

N'Diaye, E.N., Branda, C.S., Branda, S.S., Nevarez, L., Colonna, M., Lowell, C., Hamerman, J.A., and Seaman, W.E. (2009). TREM-2 (triggering receptor expressed on myeloid cells 2) is a phagocytic receptor for bacteria. J Cell Biol 184, 215-223.

Naito, M., Hasegawa, G., and Takahashi, K. (1997). Development, differentiation, and maturation of Kupffer cells. Microsc Res Tech 39, 350-364.

Painter, M.M., Atagi, Y., Liu, C.C., Rademakers, R., Xu, H., Fryer, J.D., and Bu, G. (2015). TREM2 in CNS homeostasis and neurodegenerative disease. Mol Neurodegener 10, 43.

Pellicoro, A., Ramachandran, P., and Iredale, J.P. (2012). Reversibility of liver fibrosis. Fibrogenesis Tissue Repair 5, S26.

Perugorria, M.J., Esparza-Baquer, A., Oakley, F., Labiano, I., Korosec, A., Jais, A., Mann, J., Tiniakos, D., Santos-Laso, A., Arbelaiz, A., et al. (2018). Non-parenchymal TREM-2 protects the liver from immune-mediated hepatocellular damage. Gut.

Poliani, P.L., Wang, Y., Fontana, E., Robinette, M.L., Yamanishi, Y., Gilfillan, S., and Colonna, M. (2015). TREM2 sustains microglial expansion during aging and response to demyelination. J Clin Invest 125, 2161-2170.

Quan, D.N., Cooper, M.D., Potter, J.L., Roberts, M.H., Cheng, H., and Jarvis, G.A. (2008). TREM-2 binds to lipooligosaccharides of Neisseria gonorrhoeae and is expressed on reproductive tract epithelial cells. Mucosal Immunol 1, 229-238.

Ramachandran, P., Pellicoro, A., Vernon, M.A., Boulter, L., Aucott, R.L., Ali, A., Hartland, S.N., Snowdon, V.K., Cappon, A., Gordon-Walker, T.T., et al. (2012). Differential Ly-6C expression identifies the recruited macrophage phenotype, which orchestrates the regression of murine liver fibrosis. Proc Natl Acad Sci U S A 109, E3186-3195.

Scott, C.L., Zheng, F., De Baetselier, P., Martens, L., Saeys, Y., De Prijck, S., Lippens, S., Abels, C., Schoonooghe, S., Raes, G., et al. (2016). Bone marrow-derived monocytes give rise to self-renewing and fully differentiated Kupffer cells. Nat Commun 7, 10321.

Sessa, G., Podini, P., Mariani, M., Meroni, A., Spreafico, R., Sinigaglia, F., Colonna, M., Panina, P., and Meldolesi, J. (2004). Distribution and signaling of TREM2/DAP12, the receptor system mutated in human polycystic lipomembraneous osteodysplasia with sclerosing leukoencephalopathy dementia. Eur J Neurosci 20, 2617-2628.

Sharif, O., Gawish, R., Warszawska, J.M., Martins, R., Lakovits, K., Hladik, A., Doninger, B., Brunner, J., Korosec, A., Schwarzenbacher, R.E., et al. (2014). The triggering receptor expressed on myeloid cells 2 inhibits complement component 1q effector mechanisms and exerts detrimental effects during pneumococcal pneumonia. PLoS Pathog 10, e1004167.

Shirotani, K., Hori, Y., Yoshizaki, R., Higuchi, E., Colonna, M., Saito, T., Hashimoto, S., Saito, T., Saido, T.C., and Iwata, N. (2019). Aminophospholipids are signal-transducing TREM2 ligands on apoptotic cells. Sci Rep 9, 7508.

Takahashi, K., Rochford, C.D., and Neumann, H. (2005). Clearance of apoptotic neurons without inflammation by microglial triggering receptor expressed on myeloid cells-2. J Exp Med 201, 647-657.

van de Laar, L., Saelens, W., De Prijck, S., Martens, L., Scott, C.L., Van Isterdael, G., Hoffmann, E., Beyaert, R., Saeys, Y., Lambrecht, B.N., et al. (2016). Yolk Sac Macrophages, Fetal Liver, and Adult Monocytes Can Colonize an Empty Niche and Develop into Functional Tissue-Resident Macrophages. Immunity 44, 755-768.

Wang, G.X., Zhao, X.Y., Meng, Z.X., Kern, M., Dietrich, A., Chen, Z., Cozacov, Z., Zhou, D., Okunade, A.L., Su, X., et al. (2014). The brown fat-enriched secreted factor Nrg4 preserves metabolic homeostasis through attenuation of hepatic lipogenesis. Nat Med 20, 1436-1443.

Wang, Y., Cella, M., Mallinson, K., Ulrich, J.D., Young, K.L., Robinette, M.L., Gilfillan, S., Krishnan, G.M., Sudhakar, S., Zinselmeyer, B.H., et al. (2015). TREM2 lipid sensing sustains the microglial response in an Alzheimer's disease model. Cell 160, 1061-1071.

Wu, K., Byers, D.E., Jin, X., Agapov, E., Alexander-Brett, J., Patel, A.C., Cella, M., Gilfilan, S., Colonna, M., Kober, D.L., et al. (2015). TREM-2 promotes macrophage survival and lung disease after respiratory viral infection. J Exp Med 212, 681-697.

Wunderlich, P., Glebov, K., Kemmerling, N., Tien, N.T., Neumann, H., and Walter, J. (2013). Sequential proteolytic processing of the triggering receptor expressed on myeloid cells-2 (TREM2) protein by ectodomain shedding and gamma-secretase-dependent intramembranous cleavage. J Biol Chem 288, 33027-33036.

Xiong, X., Kuang, H., Ansari, S., Liu, T., Gong, J., Wang, S., Zhao, X.Y., Ji, Y., Li, C., Guo, L., et al. (2019). Landscape of Intercellular Crosstalk in Healthy and NASH Liver Revealed by Single-Cell Secretome Gene Analysis. Mol Cell 75, 644-660 e645.

Yeh, F.L., Wang, Y., Tom, I., Gonzalez, L.C., and Sheng, M. (2016). TREM2 Binds to Apolipoproteins, Including APOE and CLU/APOJ, and Thereby Facilitates Uptake of Amyloid-Beta by Microglia. Neuron 91, 328-340.

Zhang, P., Kuang, H., He, Y., Idiga, S.O., Li, S., Chen, Z., Yang, Z., Cai, X., Zhang, K., Potthoff, M.J., et al. (2018). NRG1-Fc improves metabolic health via dual hepatic and central action. JCI Insight 3.

Zheng, H., Liu, C.C., Atagi, Y., Chen, X.F., Jia, L., Yang, L., He, W., Zhang, X., Kang, S.S., Rosenberry, T.L., et al. (2016). Opposing roles of the triggering receptor expressed on myeloid cells 2 and triggering receptor expressed on myeloid cells-like transcript 2 in microglia activation. Neurobiol Aging 42, 132-141.

Zhong, L., Chen, X.F., Zhang, Z.L., Wang, Z., Shi, X.Z., Xu, K., Zhang, Y.W., Xu, H., and Bu, G. (2015). DAP12 Stabilizes the C-terminal Fragment of the Triggering Receptor Expressed on Myeloid Cells-2 (TREM2) and Protects against LPS-induced Pro-inflammatory Response. J Biol Chem 290, 15866-15877.

Zhong, L., Xu, Y., Zhuo, R., Wang, T., Wang, K., Huang, R., Wang, D., Gao, Y., Zhu, Y., Sheng, X., et al. (2019). Soluble TREM2 ameliorates pathological phenotypes by modulating microglial functions in an Alzheimer's disease model. Nat Commun 10, 1365.

Zhou, Y., Song, W.M., Andhey, P.S., Swain, A., Levy, T., Miller, K.R., Poliani, P.L., Cominelli, M., Grover, S., Gilfillan, S., et al. (2020). Human and mouse single-nucleus transcriptomics reveal TREM2-dependent and TREM2-independent cellular responses in Alzheimer's disease. Nat Med 26, 131-142.

## Chapter 4
## T Cell Landscape in Chronic Liver Injury and Hepatocellular Carcinogenesis

**Introduction to T-cell exhaustion**

In their classic settings, functional adult T cells are subdivided into the major CD4+ and CD8+ populations. CD4+ T cells mediate numerous processes involving activation of other immune cells as well as production of regulatory cytokines (Kumar et al., 2018). CD8+ T cells are generally thought to be the cytotoxic T cells. Educated T cells reach tissue sites of inflammation and receive their final activation signals from antigen-presenting cells (APCs) which allows them to perform their function (Kaech and Cui, 2012; Zhang and Bevan, 2011). In recent years, an evolving field of research has found that chronic inflammation results in a gradual loss of function in T cells. While T cells begin in an active state during acute inflammation, as they persist at these sites with prolonged injury, only a subset of them differentiate into memory T cells (Farber et al., 2014; Masopust and Schenkel, 2013). One major paradigm is that some T cells begin to accumulate classic markers of inhibitory receptors including PD1, LAG3, TIM3, and CD244 (Angelosanto et al., 2012; Doering et al., 2012; Jackson et al., 2013; Odorizzi and Wherry, 2012; Wherry, 2011; Wherry and Kurachi, 2015). Along with this classic suite of markers, the T cells lose their active function and enter a state referred to as 'exhaustion'. These T cells are noted to have lost the majority of their classic function, such as cytokine production of IFNγ, TNFα, and IL2 (Wherry, 2011). These exhausted T cells are also noted to have reduced proliferative potential and increased apoptosis (Akbar and Henson, 2011; Brenchley et al., 2003).

The effects of T cell exhaustion appears to be loss of cytotoxicity due to abrogated function of CD8+ cells (Akbar and Henson, 2011; Wirth et al., 2010). This results in reduced clearance of injured cells and foreign material. The *in vivo* effects here on viral infections will not be discussed. In the case of auto-inflammatory conditions, however, this reduction of cell clearance is known to clear a way for increased injury and carcinogenesis (Grosso et al., 2009; Matsuzaki et al., 2010). Indeed, exhausted T-cells have been found in many solid tumors and are now

believed to be a major player in tumor growth (Li et al., 2018; Pardoll, 2012; Pauken and Wherry, 2015; Schietinger and Greenberg, 2014). The characterization of these numerous exhausted T-cell populations remains incomplete, but it is believed that their loss-of-function state allows for tumor cells to expand unchecked, resulting in a worsened prognosis (Philips and Atkins, 2015). This exhausted state can be partially reversed through pharmacological blockade of their inhibitory receptors such as PD1. By blocking the progression of T cells to exhaustion, it is hoped that T cells remain functional and clear tumor cells, presenting a potential treatment for inflammatory cancers. These checkpoint blockade therapies have already reached clinical trials and shown varying degrees of success depending on the tissue sites (Chang et al., 2017; Li et al., 2016a; Li et al., 2018; Li et al., 2016b; Li et al., 2016c; M et al., 2016). These promising findings suggest that modulation of T cells has a potential to bring novel therapies to diseases, in particular to metabolic diseases, which are inflammatory in nature. Here I discuss prospects for modulating T cell exhaustion in the context of liver disease and hepatocellular carcinoma, based on scRNA-seq findings.

**CD8+ T cells adopt an exhausted transcriptional signature in NASH**

In our scRNA-seq study (Xiong et al., 2019a), one of our major clusters of liver NPCs was T-cells. Subdivision of T-cells by clustering at higher resolution yielded identifiable populations of naïve CD8+ cells, CD4+, ydT cells, NKT, and mature CD8+ cells (Figure 1A), based on classic markers of these T cell subsets (data not shown). In observing the highly regulated genes between chow and NASH, we found that CD8+ cells appeared to display higher UMI counts of genes involved in exhaustion such as Pdcd1 and Havcr2 (Figure 1B). Conversely, genes involved in T cell activation such as Klrg1 and Il2 (Akbar and Henson, 2011; Brenchley et al., 2003) appeared to be decreased based on UMI count. This led us to ask if the T cell population in NASH liver adopt increased transcription overall for exhaustion markers and lose function. To test transcription profile, we checked whole-liver RNA sequencing from our previous NASH study (Xiong et al., 2019a) and observed a whole-liver increase in transcription for exhaustion markers, including Pdcd1 and Havcr2 (Figure 1C). To confirm this, we performed qPCR on whole liver samples from mice on varying degrees of NASH diet. We found that as treatment with Amylin diet increased in duration, the total level of exhaustion marker RNA increased in the livers (Figure 1D). Interestingly, we surveyed mice who had been reverted to a normal chow

diet from Amylin diet (Xiong et al., 2019a; Xiong et al., 2019b) and found that reversal of diets negated this increase in exhaustion markers (Figure 1E), indicating that this potential exhaustion phenotype tracks with disease progression.

**T cells are functionally exhausted in diet-induced NASH mice**

Given that there appeared to be an overall increase in expression of exhaustion markers in NASH liver, we asked if these T cells were functionally exhausted in our murine models. To begin to profile the landscape of T cells, we performed flow cytometry on the non-parenchymal cells (NPCs) of Amylin-diet fed mice compared with chow diet mice. Interestingly, matching with our findings from scRNA-seq, there was a proportional increase in CD8+ T cells in NASH, and reduction of CD4+ cells (Figure 2A-B). As we found much of the exhaustion marker expression was restricted to CD8+ cells in our scRNA-seq (data not shown), we focused our studies on the CD8+ population of T cells. Profiling on flow cytometry, we observed increased expression of PD1 and LAG3, classic inhibitory receptors, in NASH liver CD8+ T cells compared to chow control (Figure 2C-D). Interestingly, we found that KLRG1, a marker for active cytotoxic T cells (Akbar and Henson, 2011; Brenchley et al., 2003), was reduced in the NASH liver CD8+ cells, indicating their function may be abrogated. To test this, we performed phorbol myristate acetate (PMA)-ionomycin stimulation of isolated T cells from our mice and tested effects of disease on cytokine secretion. We observed that NASH CD8+ T cells had a lower propensity for production of IFNγ, TNFα, and IL2 during stimulation (Figure 2E-F). This decrease in activator function leads us to conclude that CD8+ T cells are functionally exhausted in NASH. We also examined CD4+ cells for regulatory status, as regulatory T cells also act to suppress cytotoxicity, but may also contribute to exhaustion of CD8+ T cells (Farber et al., 2014; Kumar et al., 2018; Schietinger and Greenberg, 2014; Wherry and Kurachi, 2015). We observed an increase in FOXP3 in CD4+ cells in NASH, indicating increased Treg activity may also contribute to the lowered immune function of T cells in NASH (Figure 2G-H).

To verify the phenotype is a feature of NASH and not a specific diet, we utilized a different dietary model to induce liver injury, the CDA HFD model (Xiong et al., 2019a). Consistent with Amylin diet-induced NASH, we found that following a 6-week course of CDA HFD, we observed a significant increase in CD8+ T cells in liver injury compared to chow diet controls

(Figure 3A-B). The markers of exhaustion were consistent as well, as PD1 and LAG3 were increased on CD8+ T cells in CDA HFD, and KLRG1 was also decreased (Figure 3C-D). We verified functional exhaustion through PMA-ionomycin stimulation in the T cells of CDA HFD mice and found them to be reduced in cytokine secretion (Figure 3E-F). In demonstrating that a similar exhaustion phenotype exists in two different dietary models for liver injury, we show that the NASH phenotype confers this state of functional exhaustion in CD8+ T cells.

**Exhaustion of T cells in diet-induced murine NASH is restricted to the liver**

As T cells enter into sites of inflammation, they also are capable of shuttling to secondary lymphoid sites such as lymph nodes and spleen to mediate stimulation and maturation of newer T cells, as well as other immune cells (Farber et al., 2014; Kumar et al., 2018). These sites potentially act as reservoirs for T cells, including exhausted populations (Blackburn et al., 2008; Paley et al., 2012). These populations themselves have varying degrees of heterogeneity that differ based on the disease (Grosso et al., 2009; Myers et al., 2019). To assess if exhausted T cell populations exist outside of the liver in NASH, we tested secondary lymphoid sites in our Amylin diet model. Flow cytometry of mesenteric lymph node isolates showed no significant difference in proportions of CD4+ and CD8+ T cells between Amylin-diet mice and controls (Figure 4A). Levels of expression of exhaustion markers including PD1 and KLRG1 were not significantly changed in lymph CD8+ T cells compared to chow control lymph nodes (Figure 4B). We also did not observe a functional difference in the T cells, as PMA-ionomycin stimulated secretion of IFNγ, TNFα, and IL2 showed no difference in NASH and chow lymph node T cells (data not shown). In the spleen, we did not observe a significant change in the proportions of CD4+ and CD8+ T cells in NASH (Figure 4C). Interestingly, we found an increase in PD1 expression on CD8+ T cells in NASH spleen compared to chow (Figure 4D-E). In contrast to the liver, this PD1 increase was accompanied by an increase in KLRG1 expression on these T cells, indicating potentially increased function of these cells. To confirm this, we performed PMA-ionomycin stimulation on CD8+ T cells from spleen and found that NASH spleen CD8+ T cells had increased IFNγ and IL2 production than chow spleen CD8+ T cells (Figure 4F-G). This increased propensity for cytokine secretion indicates the spleen CD8+ T cells are actually more functional in NASH. We observed similar findings within the lymph nodes and spleen of mice on the CDA HFD to confirm our results were consistent among NASH

models (data not shown). We show here that T cell exhaustion is not present in the lymph nodes of NASH mice, and that while certain exhaustion inhibitory receptors are affected in spleen T cells, it appears that they are not functionally exhausted in a classic sense. Interestingly, certain subsets of PD1-high T cells are known to have increased functionality, denoting a potent progenitor population for T cells (Hashimoto et al., 2018; Hudson et al., 2019; Jadhav et al., 2019). The exact function of these unique cells remains poorly understood, particularly in the context of NASH. Future work will be needed to characterize and profile these unique CD8+ cells throughout the body in NASH, and to determine the role they play in disease progression. Regardless, it would seem that the liver is a site of T cell exhaustion that reduces cytotoxicity of foreign material, and is therefore permissive of carcinogenesis and progression to hepatocellular carcinoma (HCC).

**Role of liver CD8+ T cell exhaustion in the NASH-HCC axis**

In liver disease, repeated cell death elicits regeneration and turnover, raising the incidence of mutations, neoplasia, and HCC (Anstee et al., 2013; Baffy et al., 2012; Bhala et al., 2011; Ertle et al., 2011; Ghouri et al., 2017; Kanwal et al., 2018; Ratziu et al., 2002; Schutte et al., 2014; Wree et al., 2013). HCC remains a deadly end-stage sequellae to chronic NASH, with poor prognosis and no treatments (Schutte et al., 2014). Our group's previous work has highlighted a potential role of the adipose endocrine factor NRG4 in signaling to prevent NASH (Chen et al., 2017; Guo et al., 2017; Wang et al., 2014). Different models have found that NRG4 protects the liver from diet-induced liver injury, and that ablation of NRG4 renders the liver more vulnerable to damage. However, it remains unknown if NRG4 could then prevent pathophysiology further downstream of NASH, particularly, HCC. An interesting observation we made with T cell exhaustion was its potentially mechanistic connection with the adipokine NRG4. In liver from NRG4 transgenic mice, which have reduced liver damage and fibrosis, we observed reduced marker expression for T cell exhaustion by whole liver qPCR (Figure 5A), indicating that this reduction of exhaustion may increase toxicity and clearance of injured and offending hepatocytes, thus leading to a healthier liver environment. Conversely, in the NRG4 knockout mouse, which has worsened liver health and more fibrosis, we found an increase in the same genes by whole liver qPCR (Figure 5B). It is possible that the mechanism through which NRG4 improves liver health in dietary challenge to NASH is through protection of T cell function,

112

which can then survey the cell landscape and maintain the liver. As T cell exhaustion appears to also be potentially important in carcinogenesis, we wondered if this mechanistic connection could link NRG4 to the NASH-HCC axis.

To evaluate if NRG4 may protect from NASH-associated HCC, we adapted an established dietary mouse model for HCC in mice (Healy et al., 2016; Horie et al., 2004; Park et al., 2010; Wang et al., 2009). This model entails induction of hepatocellular toxicity by intraperitoneal injection at D15 with 25 mg/kg of liver carcinogen diethylnitrosamine (DEN), followed by switching mice from chow diet to high-fat diet at D60 (Healy et al., 2016; Horie et al., 2004; Park et al., 2010; Tolba et al., 2015; Wang et al., 2009). To better recapitulate NASH-associated HCC, we instead fed the mice with Amylin diet starting at D60 (Figure 5C). We tested this modified regimen on NRG4 transgenic mice to examine if transgenic NRG4 expression could protect mice from HCC. Because C57BL/6J (B6) mice are less susceptible to DEN (Heindryckx et al., 2009), we crossed our B6 NRG4 transgenic mice with WT C3H background mice to produce F1 WT and transgenic mice (n=20) with mixed C3H background (Figure 5C). Following DEN injection and NASH-diet feeding, mice were dissected at D150. We observed dramatically larger and more prevalent tumors in WT livers compared to NRG4 transgenic livers (Figure 5D-E), indicating that transgenic expression of NRG4 is preventative of liver tumorigenesis. Consistent with this decreased tumor burden, we found that the overall health of the transgenic mice was improved through the course of tumorigenesis. While transgenic mice are typically more resistant to aberrant lipid accumulation and weight gain in NASH (Chen et al., 2017; Guo et al., 2017; Wang et al., 2014), we found that in the carcinogenic model, the transgenic mice maintained a higher weight while the wild type mice lost weight later (Figure 5F), potentially because the transgenic mice are protected from the cachexic effects of late-stage HCC (Chang et al., 2018; Erdem et al., 2019; Meza-Junco et al., 2013). To confirm that exhaustion of T cells persisted in these cancerous conditions, we found that the exhaustion markers remained reduced by whole liver qPCR in the transgenic mice compared to wild type (Figure 5G). Interestingly, we observed a correlation between levels of Pdcd1 mRNA by qPCR and the tumor burden in our mice (Figure 5H). These findings suggest that NRG4 is indeed protective from liver carcinogenesis. Furthermore, NRG4 appears to modulate T cell exhaustion that is prominent in NASH. This blockade of exhaustion extends into the setting of HCC.

**Discussion**

We have found that in our murine dietary models for NASH, CD8+ cytotoxic cells become functionally exhausted and lose their ability to secrete inflammatory cytokines. Furthermore, the entire landscape of T cells is dramatically altered as there is an expansion of CD8+ cells in the liver, which are exhausted from their normal function. This classical exhaustion appears restricted to the liver whereas other T cell populations in the spleen gain a unique exhausted progenitor phenotype that remains functionally active. As it is known that there is functional diversity just within exhausted T cells between different diseases (Blackburn et al., 2008; Hudson et al., 2019; Paley et al., 2012), these findings indicate further work will be needed to differentiate between these spleen T cells and liver T cells, and whether they are related or independent populations. The notion that exhaustion may play a role in NASH pathogenesis does however bring the appealing notion that checkpoint inhibitor therapy may be beneficial in NASH. Future studies will study whether blockade therapy may benefit the course of NASH pathogenesis in our dietary models.

The more interesting aspect of these exhausted liver T cells was their potential role in end-stage disease. A large body of work in exhaustion has been to characterize their role in the tumor microenvironment (Li et al., 2016a; Li et al., 2018; Pardoll, 2012; Pauken and Wherry, 2015). Here we find a potential link between T cell exhaustion and hepatocellular carcinoma, wherein NRG4 defines a checkpoint for the exhaustion of CD8+ cells, while also creating a less permissive environment for tumorigenesis. A better understanding of this link could lead to future therapies for the NASH-HCC axis, which remains today one of the deadliest primary tumors known (Ertle et al., 2011; Ghouri et al., 2017). A combination therapy of pharmacologic NRG4 and checkpoint blockade could provide a synergistic treatment with more efficacy for HCC. It may be that exhaustion is even a pathogenic cause for NASH itself, but future work will be needed to demonstrate this. Connecting NRG4 and modulation of exhaustion through checkpoint therapies could lead to synergistic therapies and pave the way for improving clinical outcomes in NASH and downstream sequellae.

**Methods**

Mice

All animal studies were performed following procedures approved by the Institutional Animal Care & Use Committee at the University of Michigan. Mice were housed in pathogen-free facilities under 12-h light-dark cycles with free access to food and water. For standard chow feeding, mice were fed Teklad 5001 Laboratory Diet. For AMLN diet-induced NASH, C57/Bl6 mice were fed a diet containing 40% fat (of which 18% was trans-fat), 22% fructose, and 2% cholesterol (D09100301, Research Diets Inc.) for 20 weeks, as previously described (Clapper et al., 2013; Guo et al., 2017). In a separate diet-induced NASH model, C57/Bl6 mice were maintained on Choline-Deficient, Amino acid-defined HFD (45 kcal% fat) containing 0.1% methionine (CDAHFD, A06071309, Research Diets Inc.) for 6 weeks. For reversal studies, after 24 weeks of Amylin diet feeding mice were switched to chow diet for 16 weeks. For carcinogenesis studies, D15 mice were injected intraperitoneally with 25 mg/kg diethylnitrosamine (Sigma N0258) and housed in special hazard containment with mother. Mice were weaned normally at D21. Mice were placed on Amylin diet at D60 and maintained on diet until D150. Health of mice was monitored daily including weighing and wellness check. At dissection, tumors were counted in liver by microdissection with forceps, tumor size was measured by caliper.

Isolation and scRNA-seq analysis of liver NPC

Liver NPC were isolated following a two-step protocol of pronase/collagenase digestion. Briefly, the liver was perfused in situ with calcium-free Hank's Balanced Salt Solution (HBSS) containing 0.2mg/ml EDTA, followed by sequential perfusion with 0.4mg/ml pronase (Sigma, P5147) and 0.2% collagenase type II (Worthington, LS004196). The liver was minced and further digested with HBSS containing 0.2% collagenase type II, 0.4 mg/ml pronase and 0.1mg/ml DNase I (Roche, R104159001) in 37 °C water bath with shaking for 20 min. Digestion was terminated with DMEM containing 10% serum. The resulting liver cell suspension was centrifuged at 50g for 3 min to remove hepatocytes and passed through 30µm nylon cell strainer followed by treatment with 0.8% NH4Cl to lyse red blood cells. This NPC suspension was centrifuged, resuspended in HBSS, and subjected to density gradient centrifugation using 20% Optiprep (Axis Shield, 1114542) to remove dead cells. Cell viability was confirmed by trypan

blue exclusion. The resulting NPC were subjected to scRNA-seq analysis using 10X Genomics Chromium Single-Cell 3′ according to the manufacturer's instructions.

Data analysis

For total liver and RNA-seq, sequence reads were mapped to mouse genome mm10 using STAR. HTSeq was used to count the sequences that can be mapped to gene features. The raw read counts were normalized and processed for differential expression gene analysis using DESeq2. The significant expressed genes were determined by FDR less than 0.05. All RNA-seq data generated in this work have been deposited into the Gene Expression Omnibus (GEO) database (GSE119340, GSE129516).

For scRNA-seq, a total of 39,575 single cell NPC isolated from three chow and three NASH mice were processed using 10X Genomics CHROMIUM Single Cell 3' Solution. The libraries were sequenced using Illumina NextSeq High-Output, HiSeq 4000 and NovaSeq. We obtained a total of over 1.7 billion reads with an average of 43,122 reads per cell. Approximately 55.4% of the sequence reads can be confidently mapped to the mouse transcriptome. Seurat package (version 2.3.4) was used to analyze single cell RNA-seq data (Butler et al., 2018). After removing doublets and cells with low quality, 33,168 cells that expressed more than 500 genes and 19,349 genes with transcripts detected in more than 3 cells were used for further analysis. Unique sequencing reads for each gene were normalized to total Unique Molecular Identifiers (UMIs) in each cell to obtain normalized UMI values.  The top 1,000 highly variable genes were used for canonical correlation analysis (CCA) implemented in Seurat. Unsupervised clustering was applied after aligning the top 25 dimensions resulted from the CCA using a resolution of 0.07. The identity for each cluster was assigned based on the prior knowledge of marker genes. A higher resolution parameter was applied for sub-clustering of the endothelial and myeloid clusters. The t-SNE plots, violin plots, bar plots, circular plot, bubble plots, feature plots and heatmaps were generated by R and Java TreeView. Dot plot was generated using GraphPad.

RNA extraction and analysis

Total RNA was extracted from frozen livers or adipose using Trizol (Alkali Scientific, TRZ-100). Quantitative RT-PCR gene expression analysis was performed as previously described

116

(Guo et al., 2017; Wang et al., 2014). Liver RNA sequencing was performed using Illumina HiSeq 4000 at the University of Michigan DNA Sequencing Core.

Flow cytometry

For spleen and lymph node T cells, samples were crushed and filtered through 100 um strainers in 5% FBS and 1 mM EDTA in PBS and centrifuged at 500 g for 5 minutes to wash. Cells were then treated with 0.8% NH4Cl for 5 minutes to lyse red blood cells. For hepatic T cells, liver samples were minced in 2 mg/mL type IV collagenase (Worthington LS004186) and 0.2 mg/mL DNaseI and warmed to 37C for 30 minutes before being filtered through 100 um strainers in 5% FBS and 1 mM EDTA in PBS and centrifuged at 50x g for 3 minutes to remove hepatocytes. NPC were harvested as intermediate fraction following gradient centrifugation in 25% optiprep at 1500x g for 20 minutes. Cells were then treated with 0.8% NH4Cl for 5 minutes to lyse red blood cells. The isolated cells were centrifuged at 1,000 rpm for 5 min. After wash, 1 x 10$^6$ cells were stained with fixable viability dye (eBioscience 65-0865-14) at room temp for 10 minutes and washed in PBS before being incubated with 100 ul of various antibodies diluted at optimal concentrations for 20 min at 4 °C. The fluorochrome-conjugated antibodies against CD90.2 (Biolegend 30-H12) CD4 (Biolegend 1G1c1.5), CD8a (Biolegend 53-6.7), PD1 (Biolegend 29F.1A12), LAG3 (Biolegend C9B7W), KLRG1 (Biolegend 2F1/KLRG1), TNFα (Biolegend MP6/XT22), IFNγ (Biolegend XMG1.2), IL2 (Biolegend JES6-5H4), FOXP3 (Invitrogen FJK-16s), liver T cells were gated as CD90.2+ and gated on CD4 and CD8a for CD4 and CD8 cells, respectively. For intracellular staining of TNFα, IFNγ, and IL2, the cells were fixed and permeabilized by BD Cytofix/Cytoperm Fixation/Permeabilization Kit per manufacturer's protocol. Cells were then stained in 4C overnight in perm buffer 1x before analysis. Samples were analyzed using BD LSR cell analyzer at the Vision Research Core Facility at the University of Michigan Medical School. Data were analyzed using the CellQuest software (BD Biosciences) and Flowjo (Flowjo.com).

PMA/ionomycin stimulation

Hepatic NPC were collected as described under flow cytometry. NPC suspensions of 200 uL were plated at 1e6 cells for liver and lymph node, or 5e5 cells for spleen, in uncoated 96-well plates in IMDM with L-glut (Thermo 12440-046) containing 10% FBS, 1% Pen-Strep, 50 uM

117

beta-mercaptoethanol, and 1x Golgiplug containing Brefeldin-A (BD Biosciences 555029). For stimulation, x500 cell activation cocktail containing PMA and ionomycin was added (Biolegend 423301). Cells were incubated at 37C for 6 hours before harvesting for flow cytometry staining.

Statistics

Statistical analysis was performed using GraphPad Prism 7. Statistical differences were evaluated using two-tailed unpaired Student's t-test or one-way analysis of variance (ANOVA) between test groups as indicated in figure legends. P value less than 0.05 (*p < 0.05) was considered statistically significant.
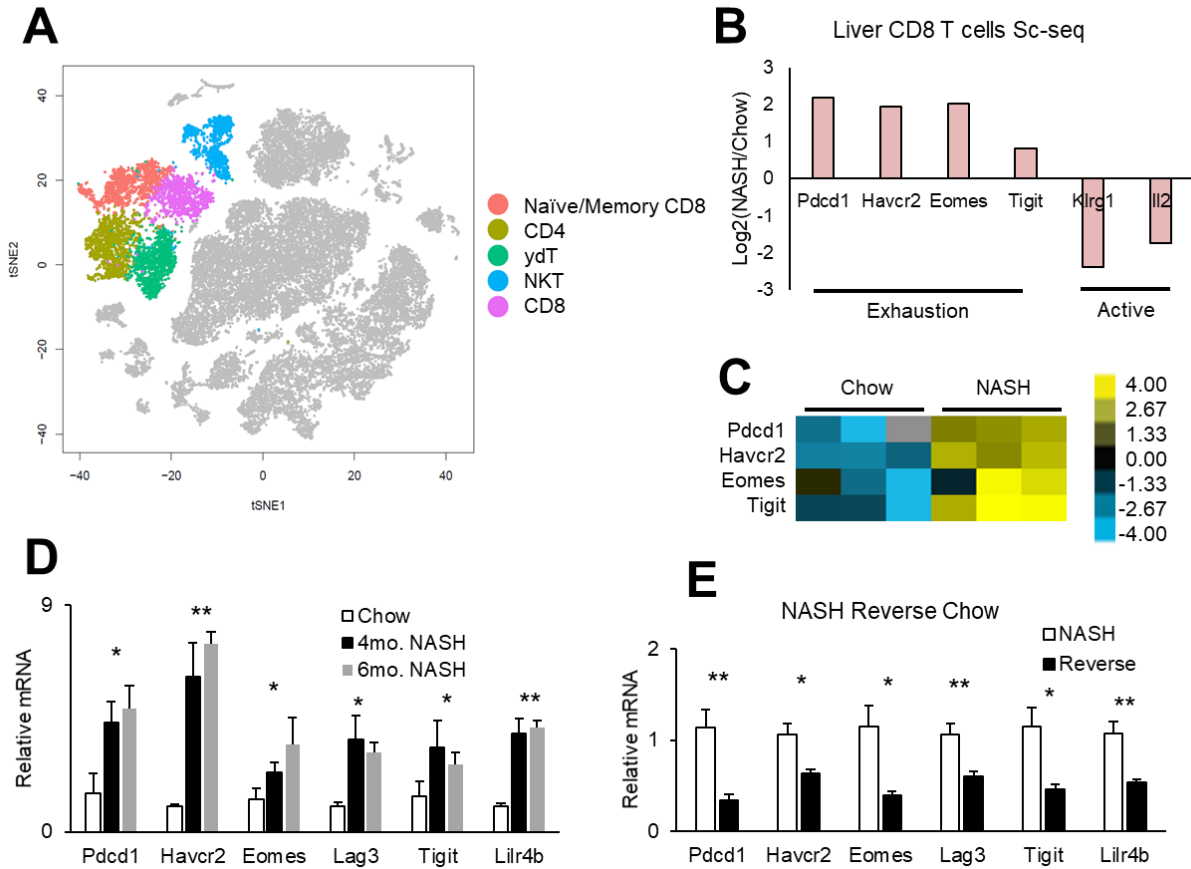
# Figures



**Figure 4.1 NASH T cells adopt a transcriptional profile resembling classic exhaustion**
(A) t-SNE visualization of liver cell clusters based on 33,168 single cell transcriptomes (Xiong et al., 2019a). Colored cluster indicates T cell populations, labeled by subtype.
(B) Log-based 2 fold change in UMI count of indicated gene for average of mice in (A), comparing NASH Amylin-diet to control chow-diet mice.
(C) Whole-liver RNA sequencing comparing NASH Amylin-diet mice (n=3) to control chow-diet mice (n=3) (Xiong et al., 2019a) for exhaustion genes, color bar indicates scale of fold change.
(D) Whole-liver qPCR for indicated genes of mice on control chow diet or Amylin NASH diet for 4 months or 6 months (n=4).
(E) Whole-liver qPCR for indicated genes of mice reverted to chow diet following Amylin NASH diet course (n=10) (Xiong et al., 2019a; Xiong et al., 2019b).
Data in (D-E) represents mean ± SEM. *p<0.05, **p<0.01, ***p<0.001 vs. chow; two-tailed unpaired Student's t-test.
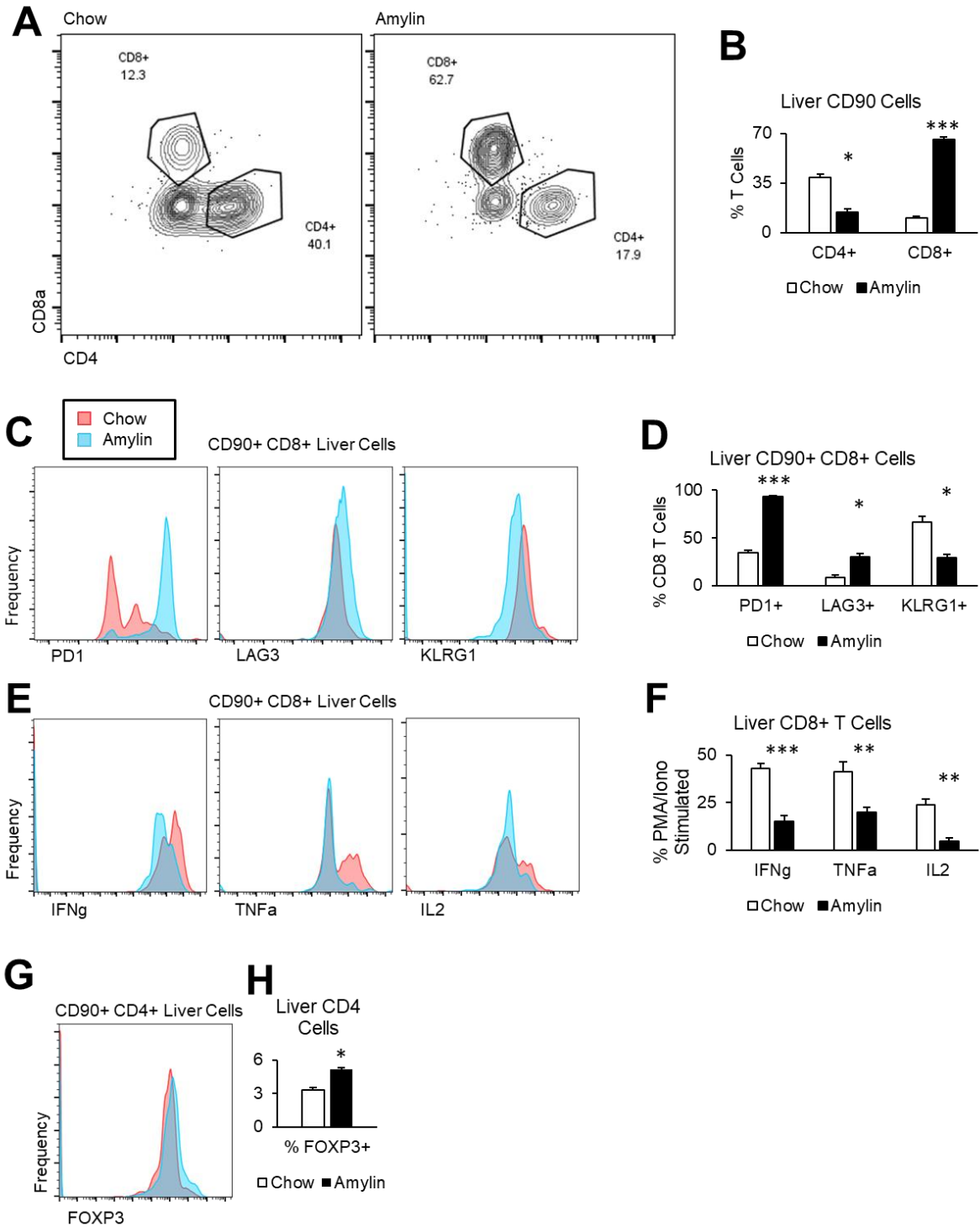
**Figure 4.2 Profiling functional exhaustion of** CD8+ **T cells in murine NASH model**
(A) Representative flow cytometry plot of CD90+ liver T cells of non-parenchymal cell isolates from control chow diet mice (n=10) and NASH Amylin-diet mice (n=10) following 5 months of feeding, plotting CD8a expression and CD4 expression. Numbers indicate relative proportion of parent population.
(B) Quantification of relative proportions of parent population of cells gated in (A) averaged for mouse group (n=10).

(C) Representative flow cytometry histograms of indicated markers for CD90+CD8+ liver T cells of non-parenchymal cell isolates in (A) comparing chow (red) and Amylin diet (blue).

(D) Quantification of relative proportions of parent population of cells gated in (C) averaged for mouse group (n=10).

(E) Representative flow cytometry histograms of indicated markers TNFα, IFNγ, IL2 for CD90+CD8+ liver T cells of non-parenchymal cell isolates in (A) comparing chow (red) and Amylin diet (blue), following 6 hour PMA/ionomycin stimulation and intracellularly stained for indicated markers.

(F) Quantification of relative proportions of parent population of cells gated in (E) averaged for mouse group (n=10).

(G) Representative flow cytometry histogram of FOXP3 for CD90+CD4+ liver T cells of non-parenchymal cell isolates in (A) comparing chow (red) and Amylin diet (blue).

(H) Quantification of relative proportions of parent population of cells gated in (G) averaged for mouse group (n=10).

Data represents mean ± SEM. *p<0.05, **p<0.01, ***p<0.001 vs. chow; two-tailed unpaired Student's t-test.
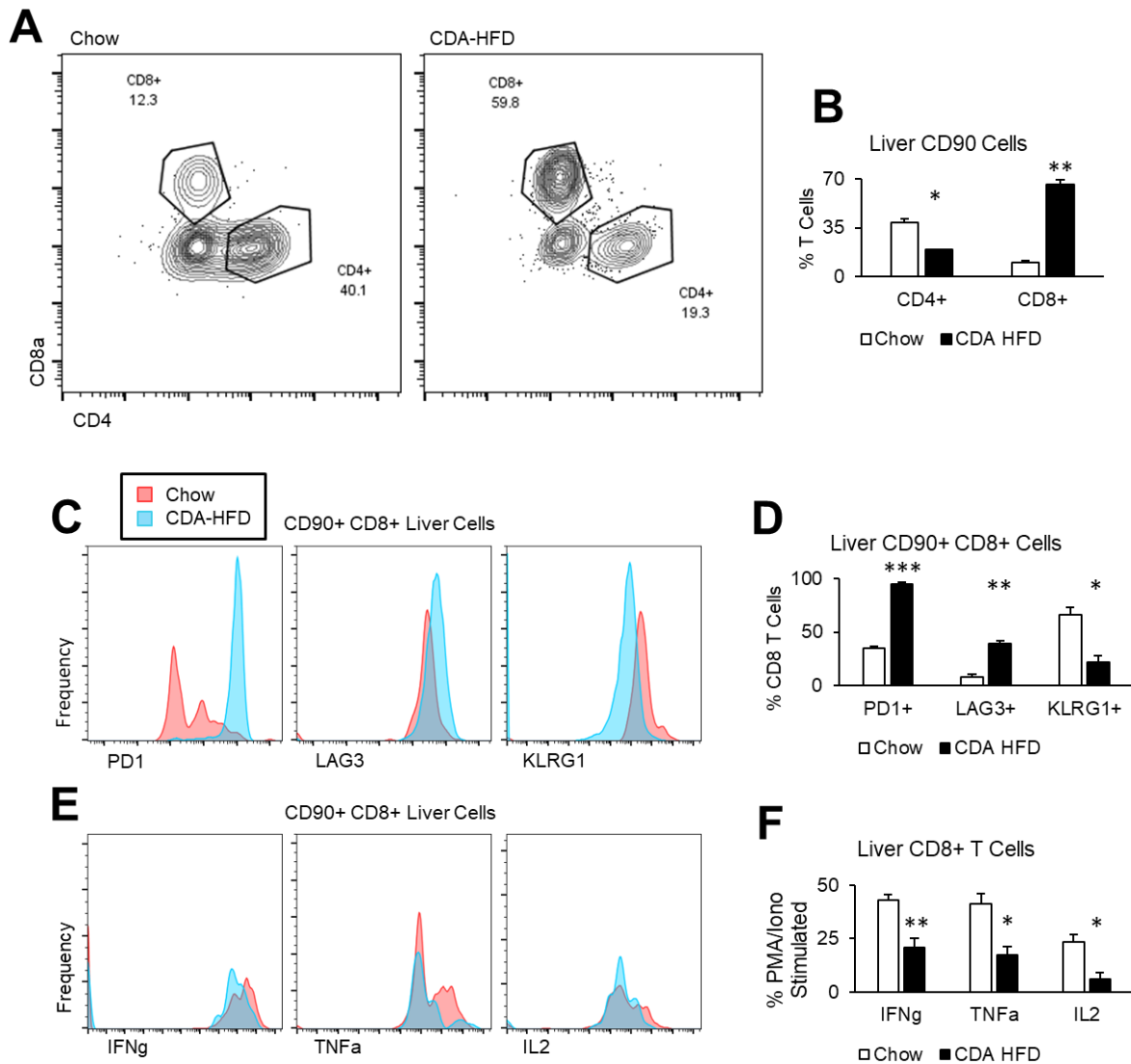


**Figure 4.3 Diet-induced NASH in mice results in functional exhaustion of T cells**

(A) Representative flow cytometry plot of CD90+ liver T cells of non-parenchymal cell isolates from control chow diet mice (n=10) and NASH CDA HFD mice (n=10) following 6 weeks of feeding, plotting CD8a expression and CD4 expression. Numbers indicate relative proportion of parent population.

(B) Quantification of relative proportions of parent population of cells gated in (A) averaged for mouse group (n=10).

(C) Representative flow cytometry histograms of indicated markers for CD90+CD8+ liver T cells of non-parenchymal cell isolates in (A) comparing chow (red) and Amylin diet (blue).

(D) Quantification of relative proportions of parent population of cells gated in (C) averaged for mouse group (n=10).

(E) Representative flow cytometry histograms of indicated markers TNFα, IFNγ, IL2 for CD90+CD8+ liver T cells of non-parenchymal cell isolates in (A) comparing chow (red) and Amylin diet (blue), following 6 hour PMA/ionomycin stimulation and intracellularly stained for indicated markers.

(F) Quantification of relative proportions of parent population of cells gated in (E) averaged for mouse group (n=10).

Data represents mean ± SEM. *p<0.05, **p<0.01, ***p<0.001 vs. chow; two-tailed unpaired Student's t-test.



**Figure 4.4 CD8+ T cell functional exhaustion in NASH spleen and mesenteric lymph nodes**
(A) Quantification of relative proportions of parent population of cells gated as CD90+CD8+ and CD90+CD4+ mesenteric lymph node T cells isolated from control chow diet mice (n=10) and NASH Amylin-diet mice (n=10) following 5 months of feeding, plotting CD8a expression and CD4 expression averaged for mouse group (n=10).
(B) Representative flow cytometry histograms of indicated markers for CD90+CD8+ mesenteric lymph node T cells isolates in (A) comparing chow (red) and Amylin diet (blue).

(C) Quantification of relative proportions of parent population of cells gated as CD90+CD8+ and CD90+CD4+ spleen T cells isolated from mice in (A), plotting CD8a expression and CD4 expression averaged for mouse group (n=10).

(D) Representative flow cytometry histograms of indicated markers for CD90+CD8+ spleen T cells isolated in (C) comparing chow (red) and Amylin diet (blue).

(E) Quantification of relative proportions of parent population of cells gated in (D) averaged for mouse group (n=10).

(F) Representative flow cytometry histograms of indicated markers TNFα, IFNγ, IL2 for CD90+CD8+ spleen T cells isolated in (D) comparing chow (red) and Amylin diet (blue), following 6 hour PMA/ionomycin stimulation and intracellularly stained for indicated markers.

(G) Quantification of relative proportions of parent population of cells gated in (F) averaged for mouse group (n=10).

Data represents mean ± SEM. *$p<0.05$, **$p<0.01$, ***$p<0.001$ vs. chow; two-tailed unpaired Student's t-test.
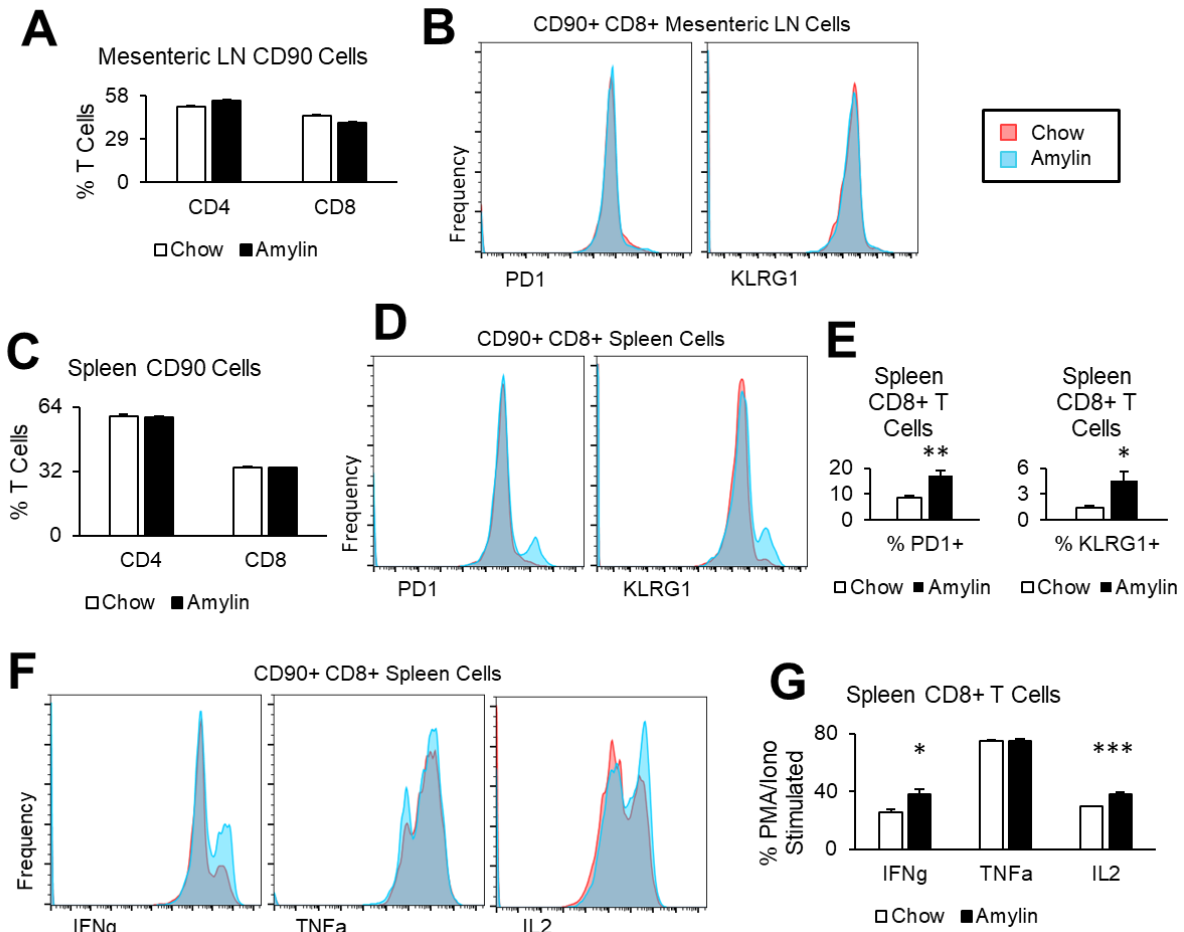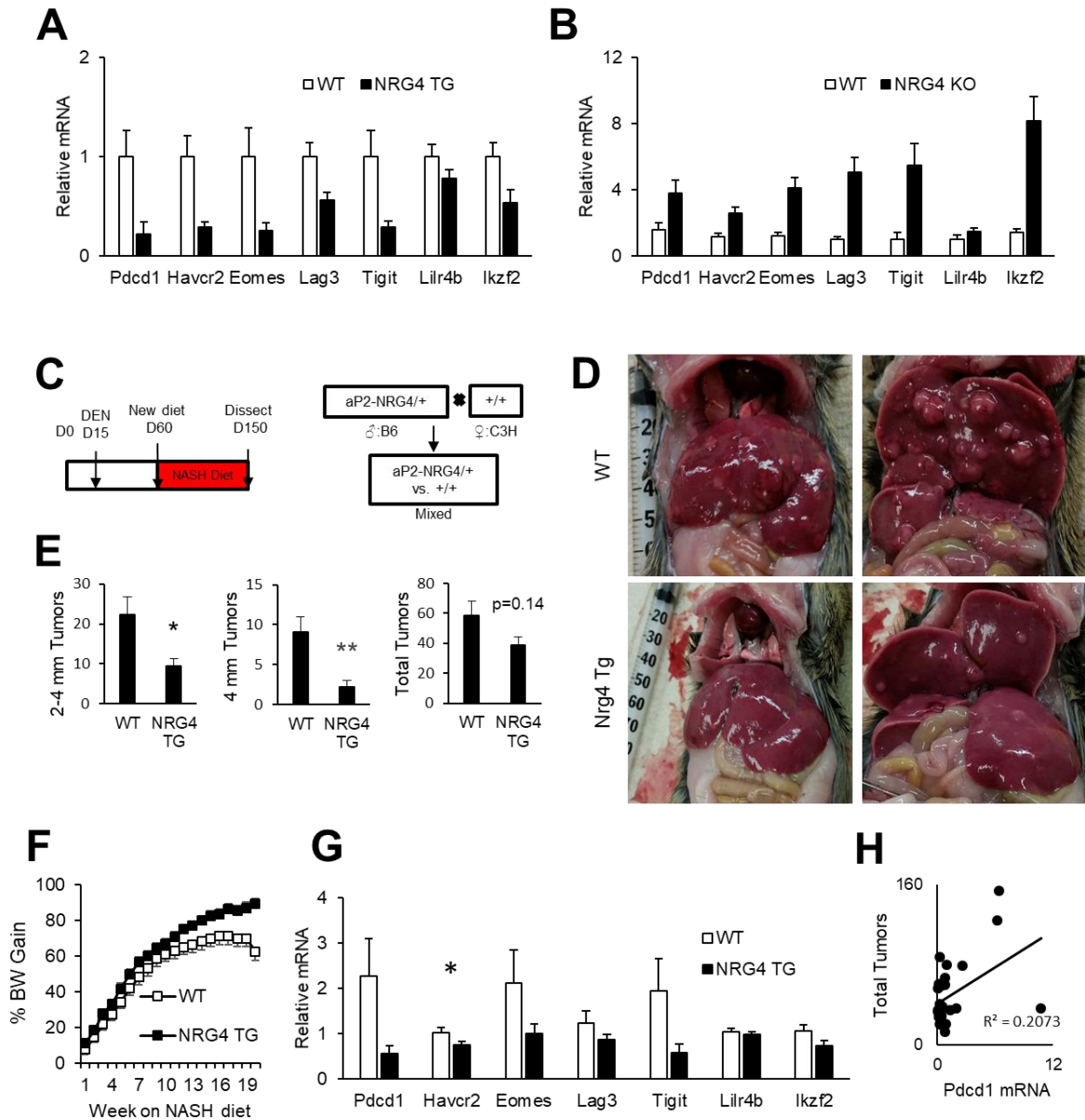
**Figure 4.5 NRG4 is an endocrine checkpoint for NASH-HCC axis and modulates T cell exhaustion**
(A) Whole-liver qPCR for indicated genes of wild type and NRG4 transgenic TG (Guo et al., 2017; Wang et al., 2014) mice on Amylin NASH diet for 6 months (n=10).
(B) Whole-liver qPCR for indicated genes of wild type (n=8) and NRG4 knockout KO (n=10) (Guo et al., 2017; Wang et al., 2014) mice on Amylin NASH diet for 6 months.
(C) Diagram of mouse background and chemical/diet induced model for NASH-associated HCC in mice.
(D) Representative images of livers from mice in (C) comparing wild type (top) to NRG4 transgenic (bottom) dissected following 20 weeks of Amylin-diet feeding (n=15).
(E) Quantification of tumor burden stratified by tumor diameter for mice in (D) (n=15).
(F) Body weight tracking of mice in (D) through course of Amylin-diet feeding.
(G) Whole-liver qPCR for indicated genes of wild type and NRG4 transgenic (n=15) mice in (D). Tissue used for qPCR included tumors and non-tumor tissue.
(H) Comparison of total tumors per mouse in (D) compared with relative Pdcd1 mRNA expression quantified by qPCR in (G), normalized to average of wild type expression.
Data represents mean ± SEM. *p<0.05, **p<0.01, ***p<0.001 vs. chow; two-tailed unpaired Student's t-test.

**References**

Akbar, A.N., and Henson, S.M. (2011). Are senescence and exhaustion intertwined or unrelated processes that compromise immunity? Nat Rev Immunol 11, 289-295.

Angelosanto, J.M., Blackburn, S.D., Crawford, A., and Wherry, E.J. (2012). Progressive loss of memory T cell potential and commitment to exhaustion during chronic viral infection. J Virol 86, 8161-8170.

Anstee, Q.M., Targher, G., and Day, C.P. (2013). Progression of NAFLD to diabetes mellitus, cardiovascular disease or cirrhosis. Nat Rev Gastroenterol Hepatol 10, 330-344.

Baffy, G., Brunt, E.M., and Caldwell, S.H. (2012). Hepatocellular carcinoma in non-alcoholic fatty liver disease: an emerging menace. J Hepatol 56, 1384-1391.

Bhala, N., Angulo, P., van der Poorten, D., Lee, E., Hui, J.M., Saracco, G., Adams, L.A., Charatcharoenwitthaya, P., Topping, J.H., Bugianesi, E., et al. (2011). The natural history of nonalcoholic fatty liver disease with advanced fibrosis or cirrhosis: an international collaborative study. Hepatology 54, 1208-1216.

Blackburn, S.D., Shin, H., Freeman, G.J., and Wherry, E.J. (2008). Selective expansion of a subset of exhausted CD8 T cells by alphaPD-L1 blockade. Proc Natl Acad Sci U S A 105, 15016-15021.

Brenchley, J.M., Karandikar, N.J., Betts, M.R., Ambrozak, D.R., Hill, B.J., Crotty, L.E., Casazza, J.P., Kuruppu, J., Migueles, S.A., Connors, M., et al. (2003). Expression of CD57 defines replicative senescence and antigen-induced apoptotic death of CD8+ T cells. Blood 101, 2711-2720.

Chang, H., Jung, W., Kim, A., Kim, H.K., Kim, W.B., Kim, J.H., and Kim, B.H. (2017). Expression and prognostic significance of programmed death protein 1 and programmed death ligand-1, and cytotoxic T lymphocyte-associated molecule-4 in hepatocellular carcinoma. APMIS 125, 690-698.

Chang, K.V., Chen, J.D., Wu, W.T., Huang, K.C., Hsu, C.T., and Han, D.S. (2018). Association between Loss of Skeletal Muscle Mass and Mortality and Tumor Recurrence in Hepatocellular Carcinoma: A Systematic Review and Meta-Analysis. Liver Cancer 7, 90-103.

Chen, Z., Wang, G.X., Ma, S.L., Jung, D.Y., Ha, H., Altamimi, T., Zhao, X.Y., Guo, L., Zhang, P., Hu, C.R., et al. (2017). Nrg4 promotes fuel oxidation and a healthy adipokine profile to ameliorate diet-induced metabolic disorders. Mol Metab 6, 863-872.

Clapper, J.R., Hendricks, M.D., Gu, G., Wittmer, C., Dolman, C.S., Herich, J., Athanacio, J., Villescaz, C., Ghosh, S.S., Heilig, J.S., et al. (2013). Diet-induced mouse model of fatty liver disease and nonalcoholic steatohepatitis reflecting clinical disease progression and methods of assessment. Am J Physiol Gastrointest Liver Physiol 305, G483-495.

Doering, T.A., Crawford, A., Angelosanto, J.M., Paley, M.A., Ziegler, C.G., and Wherry, E.J. (2012). Network analysis reveals centrally connected genes and pathways involved in CD8+ T cell exhaustion versus memory. Immunity 37, 1130-1144.

Erdem, M., Mockel, D., Jumpertz, S., John, C., Fragoulis, A., Rudolph, I., Wulfmeier, J., Springer, J., Horn, H., Koch, M., et al. (2019). Macrophages protect against loss of adipose tissue during cancer cachexia. J Cachexia Sarcopenia Muscle 10, 1128-1142.

Ertle, J., Dechene, A., Sowa, J.P., Penndorf, V., Herzer, K., Kaiser, G., Schlaak, J.F., Gerken, G., Syn, W.K., and Canbay, A. (2011). Non-alcoholic fatty liver disease progresses to hepatocellular carcinoma in the absence of apparent cirrhosis. Int J Cancer 128, 2436-2443.

Farber, D.L., Yudanin, N.A., and Restifo, N.P. (2014). Human memory T cells: generation, compartmentalization and homeostasis. Nat Rev Immunol 14, 24-35.

Ghouri, Y.A., Mian, I., and Rowe, J.H. (2017). Review of hepatocellular carcinoma: Epidemiology, etiology, and carcinogenesis. J Carcinog 16, 1.

Grosso, J.F., Goldberg, M.V., Getnet, D., Bruno, T.C., Yen, H.R., Pyle, K.J., Hipkiss, E., Vignali, D.A., Pardoll, D.M., and Drake, C.G. (2009). Functionally distinct LAG-3 and PD-1 subsets on activated and chronically stimulated CD8 T cells. J Immunol 182, 6659-6669.

Guo, L., Zhang, P., Chen, Z., Xia, H., Li, S., Zhang, Y., Kobberup, S., Zou, W., and Lin, J.D. (2017). Hepatic neuregulin 4 signaling defines an endocrine checkpoint for steatosis-to-NASH progression. J Clin Invest 127, 4449-4461.

Hashimoto, M., Kamphorst, A.O., Im, S.J., Kissick, H.T., Pillai, R.N., Ramalingam, S.S., Araki, K., and Ahmed, R. (2018). CD8 T Cell Exhaustion in Chronic Infection and Cancer: Opportunities for Interventions. Annu Rev Med 69, 301-318.

Healy, M.E., Lahiri, S., Hargett, S.R., Chow, J.D., Byrne, F.L., Breen, D.S., Kenwood, B.M., Taddeo, E.P., Lackner, C., Caldwell, S.H., et al. (2016). Dietary sugar intake increases liver tumor incidence in female mice. Sci Rep 6, 22292.

Heindryckx, F., Colle, I., and Van Vlierberghe, H. (2009). Experimental mouse models for hepatocellular carcinoma research. Int J Exp Pathol 90, 367-386.

Horie, Y., Suzuki, A., Kataoka, E., Sasaki, T., Hamada, K., Sasaki, J., Mizuno, K., Hasegawa, G., Kishimoto, H., Iizuka, M., et al. (2004). Hepatocyte-specific Pten deficiency results in steatohepatitis and hepatocellular carcinomas. J Clin Invest 113, 1774-1783.

Hudson, W.H., Gensheimer, J., Hashimoto, M., Wieland, A., Valanparambil, R.M., Li, P., Lin, J.X., Konieczny, B.T., Im, S.J., Freeman, G.J., et al. (2019). Proliferating Transitory T Cells with an Effector-like Transcriptional Signature Emerge from PD-1(+) Stem-like CD8(+) T Cells during Chronic Infection. Immunity 51, 1043-1058 e1044.

Jackson, S.R., Berrien-Elliott, M.M., Meyer, J.M., Wherry, E.J., and Teague, R.M. (2013). CD8+ T cell exhaustion during persistent viral infection is regulated independently of the virus-specific T cell receptor. Immunol Invest 42, 204-220.

Jadhav, R.R., Im, S.J., Hu, B., Hashimoto, M., Li, P., Lin, J.X., Leonard, W.J., Greenleaf, W.J., Ahmed, R., and Goronzy, J.J. (2019). Epigenetic signature of PD-1+ TCF1+ CD8 T cells that act as resource cells during chronic viral infection and respond to PD-1 blockade. Proc Natl Acad Sci U S A 116, 14113-14118.

Kaech, S.M., and Cui, W. (2012). Transcriptional control of effector and memory CD8+ T cell differentiation. Nat Rev Immunol 12, 749-761.

Kanwal, F., Kramer, J.R., Mapakshi, S., Natarajan, Y., Chayanupatkul, M., Richardson, P.A., Li, L., Desiderio, R., Thrift, A.P., Asch, S.M., et al. (2018). Risk of Hepatocellular Cancer in Patients With Non-Alcoholic Fatty Liver Disease. Gastroenterology 155, 1828-1837 e1822.

Kumar, B.V., Connors, T.J., and Farber, D.L. (2018). Human T Cell Development, Localization, and Function throughout Life. Immunity 48, 202-213.

Li, C.X., Ling, C.C., Shao, Y., Xu, A., Li, X.C., Ng, K.T., Liu, X.B., Ma, Y.Y., Qi, X., Liu, H., et al. (2016a). CXCL10/CXCR3 signaling mobilized-regulatory T cells promote liver tumor recurrence after transplantation. J Hepatol 65, 944-952.

Li, X., Shao, C., Shi, Y., and Han, W. (2018). Lessons learned from the blockade of immune checkpoints in cancer immunotherapy. J Hematol Oncol 11, 31.

Li, Z., Li, N., Li, F., Zhou, Z., Sang, J., Chen, Y., Han, Q., Lv, Y., and Liu, Z. (2016b). Immune checkpoint proteins PD-1 and TIM-3 are both highly expressed in liver tissues and correlate with their gene polymorphisms in patients with HBV-related hepatocellular carcinoma. Medicine (Baltimore) 95, e5749.

Li, Z., Li, N., Li, F., Zhou, Z., Sang, J., Jin, Z., Liu, H., Han, Q., Lv, Y., and Liu, Z. (2016c). Genetic polymorphisms of immune checkpoint proteins PD-1 and TIM-3 are associated with survival of patients with hepatitis B virus-related hepatocellular carcinoma. Oncotarget 7, 26168-26180.

M, L., P, P.V., T, K., M, P., E, S., J, P., K, V.W., C, L., F, C., S, D., et al. (2016). Essential role of HDAC6 in the regulation of PD-L1 in melanoma. Mol Oncol 10, 735-750.

Masopust, D., and Schenkel, J.M. (2013). The integration of T cell migration, differentiation and function. Nat Rev Immunol 13, 309-320.

Matsuzaki, J., Gnjatic, S., Mhawech-Fauceglia, P., Beck, A., Miller, A., Tsuji, T., Eppolito, C., Qian, F., Lele, S., Shrikant, P., et al. (2010). Tumor-infiltrating NY-ESO-1-specific CD8+ T cells are negatively regulated by LAG-3 and PD-1 in human ovarian cancer. Proc Natl Acad Sci U S A 107, 7875-7880.

Meza-Junco, J., Montano-Loza, A.J., Baracos, V.E., Prado, C.M., Bain, V.G., Beaumont, C., Esfandiari, N., Lieffers, J.R., and Sawyer, M.B. (2013). Sarcopenia as a prognostic index of nutritional status in concurrent cirrhosis and hepatocellular carcinoma. J Clin Gastroenterol 47, 861-870.

Myers, L.M., Tal, M.C., Torrez Dulgeroff, L.B., Carmody, A.B., Messer, R.J., Gulati, G., Yiu, Y.Y., Staron, M.M., Angel, C.L., Sinha, R., et al. (2019). A functional subset of CD8(+) T cells during chronic exhaustion is defined by SIRPalpha expression. Nat Commun 10, 794.

Odorizzi, P.M., and Wherry, E.J. (2012). Inhibitory receptors on lymphocytes: insights from infections. J Immunol 188, 2957-2965.

Paley, M.A., Kroy, D.C., Odorizzi, P.M., Johnnidis, J.B., Dolfi, D.V., Barnett, B.E., Bikoff, E.K., Robertson, E.J., Lauer, G.M., Reiner, S.L., et al. (2012). Progenitor and terminal subsets of CD8+ T cells cooperate to contain chronic viral infection. Science 338, 1220-1225.

Pardoll, D.M. (2012). The blockade of immune checkpoints in cancer immunotherapy. Nat Rev Cancer 12, 252-264.

Park, E.J., Lee, J.H., Yu, G.Y., He, G., Ali, S.R., Holzer, R.G., Osterreicher, C.H., Takahashi, H., and Karin, M. (2010). Dietary and genetic obesity promote liver inflammation and tumorigenesis by enhancing IL-6 and TNF expression. Cell 140, 197-208.

Pauken, K.E., and Wherry, E.J. (2015). Overcoming T cell exhaustion in infection and cancer. Trends Immunol 36, 265-276.

Philips, G.K., and Atkins, M. (2015). Therapeutic uses of anti-PD-1 and anti-PD-L1 antibodies. Int Immunol 27, 39-46.

Ratziu, V., Bonyhay, L., Di Martino, V., Charlotte, F., Cavallaro, L., Sayegh-Tainturier, M.H., Giral, P., Grimaldi, A., Opolon, P., and Poynard, T. (2002). Survival, liver failure, and hepatocellular carcinoma in obesity-related cryptogenic cirrhosis. Hepatology 35, 1485-1493.

Schietinger, A., and Greenberg, P.D. (2014). Tolerance and exhaustion: defining mechanisms of T cell dysfunction. Trends Immunol 35, 51-60.

Schutte, K., Schulz, C., Poranzke, J., Antweiler, K., Bornschein, J., Bretschneider, T., Arend, J., Ricke, J., and Malfertheiner, P. (2014). Characterization and prognosis of patients with hepatocellular carcinoma (HCC) in the non-cirrhotic liver. BMC Gastroenterol 14, 117.

Tolba, R., Kraus, T., Liedtke, C., Schwarz, M., and Weiskirchen, R. (2015). Diethylnitrosamine (DEN)-induced carcinogenic liver injury in mice. Lab Anim 49, 59-69.

Wang, G.X., Zhao, X.Y., Meng, Z.X., Kern, M., Dietrich, A., Chen, Z., Cozacov, Z., Zhou, D., Okunade, A.L., Su, X., et al. (2014). The brown fat-enriched secreted factor Nrg4 preserves metabolic homeostasis through attenuation of hepatic lipogenesis. Nat Med 20, 1436-1443.

Wang, Y., Ausman, L.M., Greenberg, A.S., Russell, R.M., and Wang, X.D. (2009). Nonalcoholic steatohepatitis induced by a high-fat diet promotes diethylnitrosamine-initiated early hepatocarcinogenesis in rats. Int J Cancer 124, 540-546.

Wherry, E.J. (2011). T cell exhaustion. Nat Immunol 12, 492-499.

Wherry, E.J., and Kurachi, M. (2015). Molecular and cellular insights into T cell exhaustion. Nat Rev Immunol 15, 486-499.

Wirth, T.C., Xue, H.H., Rai, D., Sabel, J.T., Bair, T., Harty, J.T., and Badovinac, V.P. (2010). Repetitive antigen stimulation induces stepwise transcriptome diversification but preserves a core signature of memory CD8(+) T cell differentiation. Immunity 33, 128-140.

Wree, A., Broderick, L., Canbay, A., Hoffman, H.M., and Feldstein, A.E. (2013). From NAFLD to NASH to cirrhosis-new insights into disease mechanisms. Nat Rev Gastroenterol Hepatol 10, 627-636.

Xiong, X., Kuang, H., Ansari, S., Liu, T., Gong, J., Wang, S., Zhao, X.Y., Ji, Y., Li, C., Guo, L., et al. (2019a). Landscape of Intercellular Crosstalk in Healthy and NASH Liver Revealed by Single-Cell Secretome Gene Analysis. Mol Cell 75, 644-660 e645.

Xiong, X., Wang, Q., Wang, S., Zhang, J., Liu, T., Guo, L., Yu, Y., and Lin, J.D. (2019b). Mapping the molecular signatures of diet-induced NASH and its regulation by the hepatokine Tsukushi. Mol Metab 20, 128-137.

Zhang, N., and Bevan, M.J. (2011). CD8(+) T cells: foot soldiers of the immune system. Immunity 35, 161-168.

# Chapter 5
## Supplemental Chapter: NRG1-Fc Improves Metabolic Health Via Dual Hepatic and Central Action

## Abstract

Neuregulins (NRGs) are emerging as an important family of signaling ligands that regulate glucose and lipid homeostasis. Neuregulin 1 (NRG1) lowers blood glucose levels in obese mice whereas the brown fat-enriched secreted factor NRG4 protects mice from high-fat diet (HFD)-induced insulin resistance and hepatic steatosis. However, the therapeutic potential of NRGs remains elusive given the poor plasma half-life of the native ligands. Here, we engineered a fusion protein between human NRG1 and the Fc domain of human IgG1 (NRG1-Fc) that exhibited extended half-life in circulation and improved potency in receptor signaling. We evaluated its efficacy in improving metabolic parameters and dissected the mechanisms of action. NRG1-Fc treatment triggered potent AKT activation in the liver, lowered blood glucose, improved insulin sensitivity, and suppressed food intake in obese mice. NRG1-Fc is a potent secretagogue for the metabolic hormone FGF21; however, the latter is largely dispensable for its metabolic effects. NRG1-Fc directly acts on the hypothalamic POMC neurons to promote membrane depolarization and increase firing rate. Taken together, NRG1-Fc exhibits improved pharmacokinetic properties and exerts metabolic benefits through dual inhibition of hepatic gluconeogenesis and caloric intake.

**Introduction**

The Neuregulin (NRG) family of ligands and their cognate ErbB receptor tyrosine kinases play an important role in the regulation of tissue development, growth and homeostasis (Burgess, 2008; Falls, 2003; Schneider and Wolf, 2009). NRGs are synthesized as membrane-bound precursor proteins, some of which undergo proteolytic cleavage to release the biologically active fragments that act via paracrine and/or endocrine mechanisms. Previous genetic studies have revealed associations between single-nucleotide polymorphisms (SNPs) in the NRG/ErbB signaling pathways and diverse metabolic traits. A multiethnic genome-wide association study identified a SNP at the ErbB4 locus to be strongly associated with greater body mass index in the African American population (Salinas et al., 2016). Two NRG3 gene SNPs were found to be associated with basal metabolic rate and body mass index (Lee et al., 2016). As such, altered NRG/ErbB signaling may contribute to the pathogenesis of metabolic disorders in humans.

Recent work has strongly implicated NRGs as endocrine regulators of metabolic physiology. Nrg4, a ligand for ErbB3 and ErbB4, was recently identified as a brown fat-enriched secreted factor that acts on the liver to attenuate de novo lipogenesis and enhance fatty acid β -oxidation (Chen et al., 2017; Harari et al., 1999; Rosell et al., 2014; Wang et al., 2015; Wang et al., 2014). Adipose tissue expression of Nrg4 was downregulated in mouse and human obesity. In fact, serum NRG4 concentrations are inversely associated with non-alcoholic fatty liver disease (NAFLD), metabolic syndrome in obese Chinese adults, and subclinical cardiovascular disease in obese adults (Cai et al., 2016; Dai et al., 2015; Jiang et al., 2016). Mice lacking Nrg4 were more prone to diet-induced insulin resistance and hepatic steatosis, whereas fat-specific Nrg4 transgenic mice were protected from these obesity-associated metabolic disorders (Wang et al., 2014). Further, the Nrg4/ErbB4 signaling pathway protects hepatocytes from stress-induced cell death, thereby serving as an endocrine checkpoint for the steatosis to steatohepatitis transition (Guo et al., 2017).

The EGF-like domain of NRG1 has been previously demonstrated to promote glucose uptake and mitochondrial oxidative metabolism in cultured myotubes (Canto et al., 2007; Canto et al., 2004; Suarez et al., 2001). When administered into mice, this fragment lowered blood glucose and reduced weight gain (Ennequin et al., 2015a; Ennequin et al., 2015b). However, the

physiological and molecular mechanisms through which NRG1 exerts these metabolic effects remain largely unknown. Recombinant NRG1 has been tested in clinical studies to improve cardiac function in heart failure patients (Gao et al., 2010; Jabbour et al., 2011; Mendes-Ferreira et al., 2016). Due to its short plasma half-life, continuous intravenous administration of recombinant NRG1 was required to achieve therapeutic levels in circulation. In this study, we generated a long-lived NRG1-Fc fusion protein that potently lowers blood glucose and promote weight loss in HFD-fed mice. Our findings revealed unexpected dual effects of recombinant NRG1-Fc on the inhibition of hepatic gluconeogenesis and the central regulation of food intake.

**Methods**

Construction and purification of NRG1-Fc

The NRG1-Fc fusion construct contains an N-terminal signal peptide from Azurocidin 1 followed by the EGF-like domain of human NRG1 (amino acids 176 - 226 of hNRG1), a glycine-serine linker and human IgG1 Fc fragment (Fig. 1A). The construct was synthesized by GeneArt (Thermo Fisher Scientific) and subcloned into pcDNA3 expression vector. For Fc fusion protein production, The Fc vector and NRG1-Fc constructs were transiently transfected into suspension HEK293 cells using the Expi293™ Expression System (Thermo Fisher Scientific). Conditional media (CM) were collected seven days after transfection, adjusted to the composition of binding buffer (0.2 M sodium phosphate, pH 7.0), filtered through 0.45 um filter (Millipore), and processed for affinity purification using Hitrap rProtein A FF 5 ml column on ÄKTA Pure FPLC chromatography system (GE Healthcare). The column was washed with 50 ml binding buffer and eluted with a pH 3-7 gradient elution buffer (0.1 M sodium citrate, pH 3.0). Fusion proteins were dialyzed in 1X phosphate-buffered saline buffer (137 mM NaCl, 2.7 mM KCl, 10 mM Na2HPO4, 1.8 mM KH2PO4, pH 7.4) using Slide-A-Lyzer® Dialysis Cassette (Thermo Fisher Scientific).

Mouse studies

All mouse studies were performed according to procedures approved by the University Committee on Use and Care of Animals at the University of Michigan. Mice were maintained under 12/12 hr light/dark cycles with free access to food and water. Teklad 5001 laboratory diet

133

was used as standard chow. For HFD feeding, mice were fed a diet containing 60% of calories from fat (D12492, Research Diets). C57BL/6J mice were obtained from the Jackson Laboratory. The generation of liver-specific FGF21 KO mice was previously described (Markan et al., 2014).

For measurements of plasma half-life NRG1-Fc, male C57BL/6J mice received an intraperitoneal injection of NRG1-Fc (0.6 mg/Kg). NRG1-Fc fusion protein was quantified using Human IgG ELISA Quantitation Set (Bethyl Laboratories, Inc.). Glucose, insulin, and pyruvate tolerance tests were performed as previously described (Meng et al., 2017; Molusky et al., 2012). For insulin signaling studies, HFD-fed mice received three doses of Fc or NRG1-Fc (50 µg/Kg BW) over a period of one week were fasted overnight for 16 hr before insulin injection. Tissues were harvested 10 min after intravenous injection insulin (1.5 U/Kg BW) for immunoblotting analyses.

Liver glycogen and TAG were measured as previously described (Li et al., 2008; Meng et al., 2017). Plasma concentrations of TAG and NEFA were measured using commercial assay kits (Stanbio Laboratory). Plasma insulin and FGF21 concentrations were measured using mouse insulin ELISA kit (Crystal Chem) and mouse/rat FGF21 quantikine ELISA kit (R&D Systems), respectively.

Electrophysiology

POMC-CreER/Rosa26-tdTOMATO mice received tamoxifen inductions (0.2 mg/g, i.p., twice at 9 weeks of age). At 13-14 weeks of age, these mice were deeply anesthetized with isoflurane at 9:00-9:30 am, and transcardially perfused with a modified ice-cold artificial cerebral spinal fluid (aCSF, in mM: 10 NaCl, 25 NaHCO3, 195 Sucrose, 5 Glucose, 2.5 KCl, 1.25 NaH2PO4, 2 Na pyruvate, 0.5 CaCl2, 7 MgCl2). The mice were then decapitated, and the entire brain was removed. Brains were quickly sectioned in ice-cold aCSF solution (in mM: 126 NaCl, 2.5 KCl, 1.2 MgCl2, 2.4 CaCl2, 1 NaH2PO4, 11.1 Glucose, and 21.4 NaHCO3) saturated with 95% O2 and 5% CO2. Coronal sections containing the ARH (250 µm) were cut with a Microm HM 650V vibratome (Thermo Scientific). Then the slices were recovered in the aCSF at 34°C for 1 hour. Whole-cell patch clamp recordings were performed in the TOMATO-labelled mature POMC neurons in the ARH visually identified by an upright microscope (Eclipse FN-1, Nikon)

equipped with IR-DIC optics (Nikon 40x NIR). Signals were processed using Multiclamp 700B amplifier (Axon Instruments), sampled using Digidata 1440A and analyzed offline on a PC with pCLAMP 10.3 (Axon Instruments). The slices were bathed in oxygenated aCSF (32°C–34°C) at a flow rate of approximately 2 ml/min. Patch pipettes with resistances of 3-5 MΩ were filled with solution containing 126 mM K gluconate, 10 mM NaCl, 10 mM EGTA, 1 mM MgCl2, 2 mM Na-ATP and 0.1 mM Mg-GTP (adjusted to pH7.3 with KOH).

Current clamp was engaged to test neural firing frequency and resting membrane potential (RM) at the baseline and after puff application of vehicle, NRG1, leptin (300 nM, 1 second puff). In some experiments, the aCSF solution also contained 1 μM tetrodotoxin (TTX) and a cocktail of fast synaptic inhibitors, namely bicuculline (50 μM; a GABA receptor antagonist), AP-5 (30 μM; an NMDA receptor antagonist) and CNQX (30 μM; an AMPA receptor antagonist) to block the majority of presynaptic inputs. The values for RM and firing frequency were averaged within 2-min bin at the baseline or after puffs. The RM values were calculated by Clampfit 10.3 using the "analysis statistic" function of the software. A neuron was considered depolarized or hyperpolarized if a change in membrane potential was at least 2 mV in amplitude and this response was observed after leptin application and stayed stable for at least 2 minute. At the end of recordings, lucifer yellow dye was included in the pipette solution to trace the recorded neurons and the brain slices were fixed with 4% formalin overnight and mounted onto slides. Cells were then visualized with the Leica DM5500 fluorescence microscope to identify post hoc the anatomical location of the recorded neurons in the ARH.

Gene expression analysis
Gene expression analysis was performed as previously described (Hernandez et al., 2010; Meng et al., 2017). Briefly, total RNA was isolated using the TRIzol reagent and method. For quantitative real-time PCR (qPCR) analysis, 2 ug of total RNA was revers-transcribed using MMLV-RT (Invitrogen) and quantified by QuantStudio 6 Flex Real-Time PCR System (Thermo Fisher Scientific) using SYBR Green (Life Technologies). Relative mRNA expression was normalized to the levels of ribosomal protein 36B4.

Immunoblotting analyses

T47D cells were maintained in DMEM containing 10% FBS and starved for 12-16 hrs in serum-free DMEM before treatments with Fc, NRG1-Fc or recombinant rhNRG1 (R&D Systems) for 15 min. Total cell lysates were prepared in a lysis buffer containing 50 mM Tris (pH 7.5), 150 mM NaCl, 5 mM NaF, 25 mM b-glycer-olphosphate, 1 mM sodium orthovanadate, 10% glycerol, 1% tritonX- 100, 1 mM dithiothreitol (DTT), and freshly added protease inhibitors. Total protein concentration was determined by BCA method using Protein Assay Dye Reagent Concentrate (Bio-Rad). Antibodies used in this study are: phospho-ErbB3 (Y1289), phospho-ErbB4 (Y1284), ErbB3, ErbB4, phospho-AKT (T308), phospho-AKT (S473), AKT, phospho-S6K and S6K (Cell Signaling Technology), Tubulin (T6199, Sigma), and ErbB3 (sc-285, Santa Cruz Biotechnology).

Statistics

Statistical analysis was performed using GraphPad Prism 7. Statistical differences were evaluated using two-tailed unpaired Student's t-test or one-way analysis of variance (ANOVA) between test groups as indicated in figure legends. P value less than 0.05 (*$p < 0.05$) was considered statistically significant.

**Results**

*Recombinant NRG1-Fc triggers potent and selective AKT activation in the liver*

The NRG family of ligands has been demonstrated to elicit beneficial metabolic effects in mice. NRG1 engages the ErbB receptor tyrosine kinases through its EGF-like domain, a small fragment that exhibits short half-life in circulation (Liu et al., 2006). Poor pharmacokinetic properties hinder the assessment of its potential as a therapeutic biologic for improving metabolic health in chronic settings. To address this, we fused the EGF-like domain of human NRG1 (a.a. 176 – 226) to the Fc fragment of human IgG1 (NRG1-Fc; Fig. 1A). This strategy has been successfully used to improve treatment efficacy of therapeutic biologics by increasing their half-life in circulation (Czajkowsky et al., 2012; Wu and Sun, 2014). As expected, recombinant NRG1-Fc protein exhibited markedly prolonged plasma half-life in mice, reaching approximately 40 hrs following intraperitoneal injection (Fig. 1B). NRG1-Fc stimulated tyrosine phosphorylation of ErbB3 and ErbB4 in T47D cells in a dose-dependent manner (Fig. 1C). Intriguingly, NRG1-Fc exhibited higher potency in triggering ErbB receptor activation and AKT

phosphorylation than a commercial recombinant NRG1 protein that contains the EGF-like domain alone. As NRG1-Fc fusion protein exists as a dimer as a result of Fc domain dimerization, our results suggest that the dimeric NRG1 ligand may be more efficacious in receptor engagement and signaling.

We next examined the effects of NRG1-Fc on ErbB signaling in C57BL/6 mice after overnight fasting. Compared to Fc control, intravenous injection of NRG1-Fc (100 ug/kg) resulted in rapid induction of endogenous ErbB3 phosphorylation within 15 min in the liver, which was accompanied by robust activation of AKT and S6K (Fig. 1D). This stimulatory effect was also observed at lower doses (25 ug/kg, data not shown). Similar to cell culture studies, NRG1-Fc was more potent in stimulating ErbB/AKT signaling than rhNRG1. In striking contrast, no significant changes in AKT phosphorylation were observed in the heart, quadriceps muscle, inguinal WAT (iWAT), epididymal WAT (eWAT), and brown adipose tissue (BAT) following NRG1-Fc treatment (Fig. 1E). This remarkable selectivity of hepatic AKT activation by NRG1-Fc demonstrates that, among the peripheral insulin-sensitive metabolic tissues, the liver is likely a primary target of NRG1-Fc action.

*NRG1-Fc lowers blood glucose by suppressing hepatic gluconeogenesis*
AKT is a key mediator of insulin signaling that suppresses hepatic gluconeogenesis during the postprandial phase. We next examined how acute exposure to NRG1-Fc fusion protein affects hepatic and systemic glucose metabolism. Compared to Fc, a single intravenous injection of NRG1-Fc resulted in significantly lower blood glucose 6 hrs after treatment (Fig. 2A). To determine whether NRG1-Fc may lower blood glucose by augmenting insulin secretion by islet β-cells, we measured plasma insulin concentrations in treated mice. As shown in Fig. 2A, mice treated with NRG1-Fc had significantly lower plasma insulin concentrations than control, suggesting that lower blood glucose likely precedes reduced insulin secretion. Quantitative PCR (qPCR) analysis of gene expression indicated that mRNA levels of key gluconeogenic genes, including phosphoenolpyruvate carboxykinase 1 (Pck1) and glucose-6-phosphatase (G6pc), and Ppargc1a, a transcriptional coactivator that stimulates gluconeogenic gene expression (Liu and Lin, 2011), were decreased in the livers from mice treated with NRG1-Fc (Fig. 2B). We performed pyruvate tolerance test to directly assess hepatic glucose production. Compared to

137

control, blood glucose levels were significantly lower in NRG1-Fc treated mice following pyruvate injection, indicative of attenuated hepatic glucose production (Fig. 2C). AKT activation is known to promote glycogen storage in the liver. Accordingly, we observed significantly higher liver glycogen content in mice treated with NRG1-Fc than control (Fig. 2D). Hepatic expression of FGF21, a hepatokine with diverse metabolic effects (Markan and Potthoff, 2016; Owen et al., 2015), was also strongly induced by approximately 30-fold in response to NRG1-Fc treatment (Fig. 2E). Plasma FGF21 levels reached over 1500 pg/ml compared to approximately 95 pg/ml in mice treated with Fc, indicating that NRG1-Fc acts as a potent FGF21 secretagogue in mice. The drastic rise of circulating FGF21 by NRG1-Fc diminished 2-3 days following treatment with the fusion protein (data not shown).

We next examined the effects of NRG1-Fc on metabolic signaling and glucose metabolism in HFD-fed obese mice. Similar to the observations in lean mice, we found that tail vein injection of NRG1-Fc potently stimulated ErbB3 and AKT phosphorylation in the liver (Fig. 3A). Compared to control, blood glucose levels were significantly lower in the mice treated with NRG1-Fc 30 min following the treatments (Fig. 3B). This decrease in blood glucose was sustained one day after a single dose of NRG1-Fc, accompanied by lower plasma insulin concentrations (Fig. 3C). Hepatic gene expression analysis indicated that Pck1 and G6pc mRNA expression was markedly inhibited by NRG1-Fc (Fig. 3D). Hepatic expression and plasma levels of FGF21 were significantly induced by NRG1-Fc in diet-induced obese mice (Fig. 3E). Together, these results suggest that reduced hepatic gluconeogenesis likely underlies the acute glucose-lowering effects of NRG1-Fc.

*NRG1-Fc resolves key aspects of selective hepatic insulin resistance in diet-induced obese mice*
The potent effects of NRG1-Fc on hepatic signaling and glucose metabolism prompted us to investigate the efficacy of chronic administration of NRG1-Fc in ameliorating metabolic disorders associated with obesity. HFD-fed obese mice were intraperitoneally injected biweekly with Fc or NRG1-Fc (25 ug/kg). We measured body weight and food intake of treated mice daily. While mice receiving Fc had modest changes in body weight, the NRG1-Fc treated group lost approximately 10% body weight within one week, accompanied by significantly reduced cumulative food intake during the treatment period (Fig. 4A-B). Plasma triglycerides (TAG) and

non-esterified fatty acids (NEFA) concentrations were largely unaffected by recombinant NRG1-Fc (Fig. 4C). In contrast, blood glucose and plasma insulin levels were significantly lower in mice treated with NRG1-Fc under both fed and fasted conditions (Fig. 4D-E). Consistently, glucose and insulin-tolerance tests demonstrated that NRG1-Fc treatment markedly improved whole-body glucose tolerance and insulin sensitivity in obese mice (Fig. 4F). To directly assess insulin sensitivity in peripheral tissues, we injected HFD-fed mice treated with Fc or NRG1-Fc for 7 days with a single dose of insulin via tail vein and examined AKT activation in the liver, eWAT, and quadriceps muscle. As expected, insulin robustly activated AKT phosphorylation in these insulin-responsive tissues (Fig. 4G). Insulin-stimulated AKT phosphorylation was further augmented by pretreatment of mice with recombinant NRG1-Fc fusion protein.

Obesity is commonly linked to aberrant activation of both gluconeogenesis and de novo lipogenesis in the liver, a phenomenon described as selective hepatic insulin resistance (Brown and Goldstein, 2008). As a result, elevated hepatic glucose output contributes to hyperglycemia in diabetes whereas increased lipogenesis exacerbates hepatic steatosis and hyperlipidemia. We next examined whether NRG1-Fc treatment ameliorates the molecular features associated with selective hepatic insulin resistance. We found that, compared to control, mRNA levels of gluconeogenic genes (Pck1 and G6pc) were significantly lower in the livers from mice treated with NRG1-Fc under fasted condition (Fig. 5A). The expression of several genes involved in de novo lipogenesis, including Acetyl-CoA carboxylase 2 (Acc2), Malic enzyme 1 (Me1), Stearoyl-CoA desaturase 1 (Scd1), and Thyroid hormone responsive (Thrsp, also known as S14), was also attenuated. Under fed condition, the expression of a larger set of lipogenic genes, including Acc2, Me1, ATP-citrate lyase (Acly), Fatty acid synthase (Fasn), Scd1, Thrsp, and Cell death-inducing DFFA-like effector c (Cidec, also known as Fsp27), were significantly lower in NRG1-Fc-treated mice (Fig. 5B). The expression of genes involved in inflammatory signaling, including Tumor necrosis factor α (TNFα), C-C motif chemokine 2 (Ccl2), and Adhesion G protein-coupled receptor E1 (Adgre1, also known as F4/80), remained largely unaffected by the treatments. As such, chronic NRG1-Fc treatment exerts an inhibitory effect on transcriptional activation of hepatic gluconeogenic and lipogenic gene programs in obese mice. Surprisingly, NRG1-Fc had modest effects on hepatic fat content (Fig. 5C-D). As mice treated with NRG1-Fc

had markedly lower plasma insulin levels, it is likely that increased adipose tissue lipolysis may offset the beneficial effects of lipogenic inhibition on hepatic steatosis.

*Direct action of NRG1 in POMC neurons mediates its inhibitory effects on food intake*
FGF21 is a hepatokine that has been demonstrated to promote energy expenditure and improve insulin sensitivity (Markan and Potthoff, 2016; Owen et al., 2015). The robust increase of plasma FGF21 levels following NRG1-Fc treatment raised the possibility that FGF21 may mediate certain metabolic effects of NRG1. To test this, we administered recombinant Fc or NRG1-Fc protein into HFD-fed control (flox/flox) and liver-specific FGF21 knockout (LKO) mice. As expected, plasma FGF21 levels were elevated in control group following NRG1-Fc treatment (Fig. 6A, P =0.07). FGF21 was nearly undetectable in plasma from LKO mice, consistent with previous findings that the liver is the major source of FGF21 in circulation (Markan et al., 2014). To our surprise, NRG1-Fc treatment resulted in similar weight loss and glucose lowering in control and LKO mice (Fig. 6B-C). Further, the inhibitory effect of NRG1-Fc on food intake was largely unaffected by FGF21 deficiency (Fig. 6D). As such, while we cannot rule out that certain functions of NRG1 may require FGF21, the latter appears to be largely dispensable for the effects of NRG1-Fc on energy balance and glucose metabolism.

To explore the neural mechanisms by which NRG1-Fc suppresses food intake, we examined whether NRG1-Fc directly acts on the hypothalamus to trigger neuronal activation. ErbB4, but not ErbB3, is abundantly expressed in the central nervous system (Bean et al., 2014; Mei and Xiong, 2008). Intravenous administration of NRG1-Fc robustly stimulated ErbB4 phosphorylation in the hypothalamus (Fig. 7A). Accordingly, mRNA expression of c-Fos, a molecular marker of neuronal activity, was significantly induced in response to NRG1-Fc (Fig. 7B). These results demonstrate that circulating NRG1-Fc is capable of penetrating the blood brain barrier and directly acts on hypothalamic neurons to regulate feeding behaviors.

We next examined its effects on excitability of pro-opiomelanocortin (POMC) neurons in the arcuate nucleus of the hypothalamus (ARH), which are well-known to produce anorexigenic effects (Zhan et al., 2013). We found that vehicle treatment (Fc) did not affect the resting

140

membrane potential and firing rate of ARH POMC neurons (Fig. 7C-E). Interestingly, exposure to NRG1-Fc (300 nM, 1s puff) significantly depolarized 16/31 (51.61%) of POMC neurons, while the other 15 POMC neurons tested were not affected. The depolarization was associated with significant increases in firing rate (Fig. 7F). As leptin also depolarizes POMC neurons to exert anorectic effects (Cowley et al., 2001), we examined leptin-induced depolarization in TOMATO-labeled mature POMC neurons, and found that 13/38 (34.21%) of POMC neurons were depolarized by leptin (Fig. 7C-D). Notably, leptin-induced depolarization and increases in firing rate were comparable to responses evoked by NRG1-Fc (Fig. 7E-F). We next recorded NRG1-induced changes in resting membrane potential in the presence of a cocktail of neuronal inhibitors containing 1 $\mu$M tetrodotoxin (TTX), which blocks action potentials, and a mixture of fast synaptic inhibitors (GABA receptor antagonist, bicuculline; AP-5, NMDA receptor antagonist; CNQX, AMPA receptor antagonist), which block the majority of presynaptic inputs. Under this condition, we found that 9/18 (50%) of POMC neurons were depolarized in response to NRG1-Fc (Fig. 7C-E), suggesting that NRG1-Fc likely acts directly upon POMC neurons to modulate their excitability.

**Discussion**

Neuregulins are emerging as an important family of ligands that regulates diverse aspects of glucose and lipid metabolism and energy balance. Nrg4 protects mice from HFD-induced insulin resistance and hepatic steatosis by attenuating de novo lipogenesis and promoting fuel oxidation in the liver. Further, hepatic Nrg4 signaling serves as an endocrine checkpoint for the steatosis to NASH transition by protecting hepatocytes from stress-induced cell death. NRG1 improves whole body glucose metabolism and has been shown to exert beneficial effects on cardiac function in heart failure patients. Despite these intriguing observations, the therapeutic potential of NRGs remains elusive given the poor plasma half-life of the native ligands. In this study, we generated an NRG1-Fc fusion protein with prolonged plasma half-life and characterized its metabolic action in mice in acute and chronic settings. Our findings revealed surprisingly potent dual effects of recombinant NRG1-Fc on the inhibition of hepatic gluconeogenesis and the central regulation of food intake (Fig. 8).

The ErbB receptors, particularly ErbB4, exhibit a broad pattern of tissue distribution, including skeletal muscle and heart (Falls, 2003). As such, the highly selective AKT activation in the liver, but not in other peripheral tissues known to express these ErbB receptors, came as a surprise. In fact, we failed to detect changes in AKT phosphorylation in skeletal muscle and the heart in response to intravenous injection of NRG1-Fc. In contrast, ErbB3/AKT signaling was markedly stimulated by NRG1-Fc in both lean and obese mouse livers, leading to suppression of gluconeogenic gene expression and hepatic glucose output. Following chronic treatments, mice receiving NRG1-Fc had greatly improved insulin sensitivity and glucose tolerance. This improved glucose homeostasis is linked to attenuated expression of genes involved in hepatic gluconeogenesis and de novo lipogenesis. Aberrant activation of these metabolic pathways contributes to hyperglycemia, hyperlipidemia, and hepatic steatosis in metabolic syndrome. Our results suggest that pharmacological activation of NRG1/ErbB signaling may resolve this deleterious metabolic reprogramming in obesity and improve metabolic health. Neuregulins and other EGF-like ligands are expressed in diverse tissues. Future work should address their role in ErbB-mediated metabolic signaling under various physiological and pathophysiological conditions.

An unexpected finding here is that NRG1-Fc potently stimulated hepatic expression and plasma levels of FGF21. The ability of NRG1-Fc to markedly elevate plasma FGF21 beyond its physiological levels demonstrates that NRG1-Fc serves as a powerful secretagogue for FGF21. Surprisingly, mice lacking FGF21 in the liver exhibited very low levels of plasma FGF21, yet their response to NRG1-Fc was nearly indistinguishable from control mice. These results suggest that FGF21 is largely dispensable for the effects of NRG1-Fc on blood glucose and energy balance. It remains unknown, however, whether other aspects of NRG1 action require FGF21 signaling. The inhibitory effects of NRG1-Fc on food intake and body weight are consistent with its direct action in the POMC neurons. In fact, ErbB4 is abundantly expressed in the central nervous system (Bean et al., 2014; Mei and Xiong, 2008). Peripheral administration of NRG1-Fc leads to strong ErbB4 phosphorylation and c-Fos induction in the hypothalamus. Remarkably, NRG1-Fc-induced depolarization and increase in firing rate were comparable to responses evoked by leptin, a potent anorexigenic hormone. As NRG1 is highly expressed in the central nervous system (Falls, 2003), it is possible that local NRG1 signaling in the brain may modulate

142

food intake and energy balance. In summary, pharmacological activation of NRG1/ErbB signaling by NRG1-Fc elicits multiple metabolic benefits on blood glucose and body weight, providing proof-of-principle validation for developing biologic therapeutics targeting this pathway.

Acknowledgments

Conflict of interest:
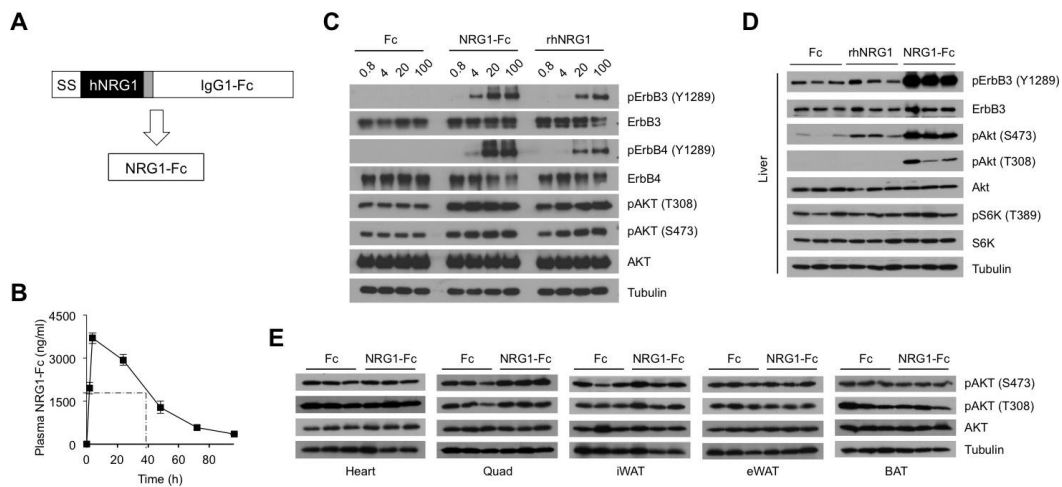The authors declare no conflict of interest.

**Figures**



**Figure 5.1 Generation and characterization of NRG1-Fc fusion protein.**
(A) A schematic diagram of the NRG1-Fc construct. Signal sequence (SS) and serine glycine linker (grey) are indicated. (B) Plasma concentrations of NRG1-Fc in mice receiving a single i.p. injection of the fusion protein (0.6 mg/kg, n=9). (C) Immunoblots of total cell lysates from T47D cells treated with different concentrations of indicated proteins for 15 min. (D) Immunoblots of total liver lysates from overnight fasted mice 15 min after intravenous injection of 100 µg/kg Fc or NRG1-Fc. (E) Immunoblots of total tissue lysates from treated mice. Data represent mean ± sem.
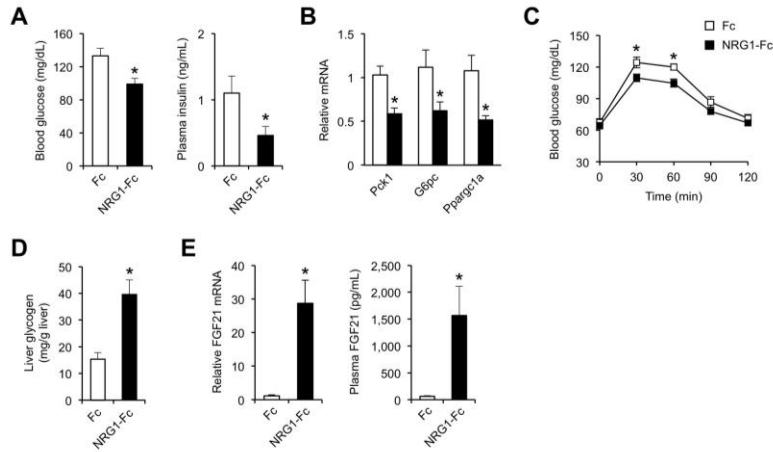
**Figure 5.2 Effects of NRG1-Fc on glucose metabolism in chow-fed mice.**
(A) Blood glucose (left) and plasma insulin (right) levels in chow-fed mice 6 hrs following i.p. injection (100 ug/kg) of Fc (open, n=9) or NRG1-Fc (filled, n=9). (B) qPCR analysis of hepatic gene expression in treated mice. (C) Pyruvate tolerance test in chow fed mice one day after Fc (open, n=7) or NRG1-Fc (filled, n=8) treatment. (D) Liver glycogen content. (E) Hepatic FGF21 mRNA expression (left) and plasma FGF21 concentrations (right) in mice described in A. Data represent mean ± sem. *p < 0.05, vs. Fc; two-tailed unpaired Student's t-test.
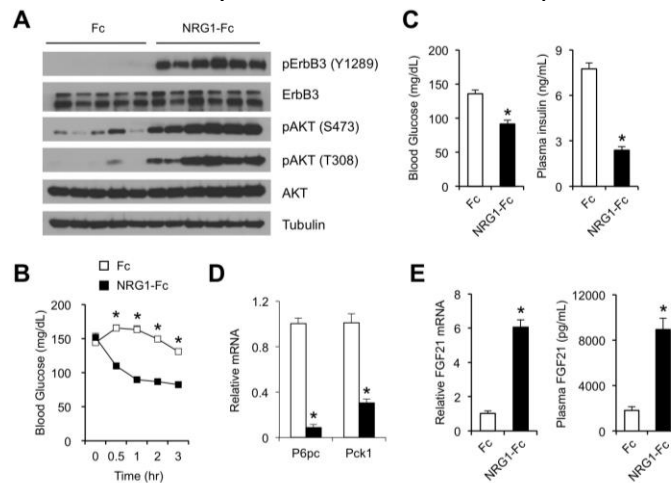


**Figure 5.3 Effects of NRG1-Fc on glucose metabolism in HFD-fed mice.**
(A) Immunoblots of total liver lysates from mice four hrs after Fc or NRG1-Fc administration (100 ug/kg). (B) Blood glucose at different time points following a single dose of Fc (open, n=7) or NRG1-Fc (filled, n=7) in HFD-fed mice. (C) Blood glucose and plasma insulin levels in HFD mice treated with Fc (open, n=4) or NRG1-Fc (filled, n=5) for 24 hrs. (D) qPCR analysis of hepatic gene expression. (E) Hepatic FGF21 mRNA expression (left) and plasma FGF21 concentrations (right) in treated mice. Data represent mean ± sem. *p < 0.05, vs. Fc; two-tailed unpaired Student's t-test.
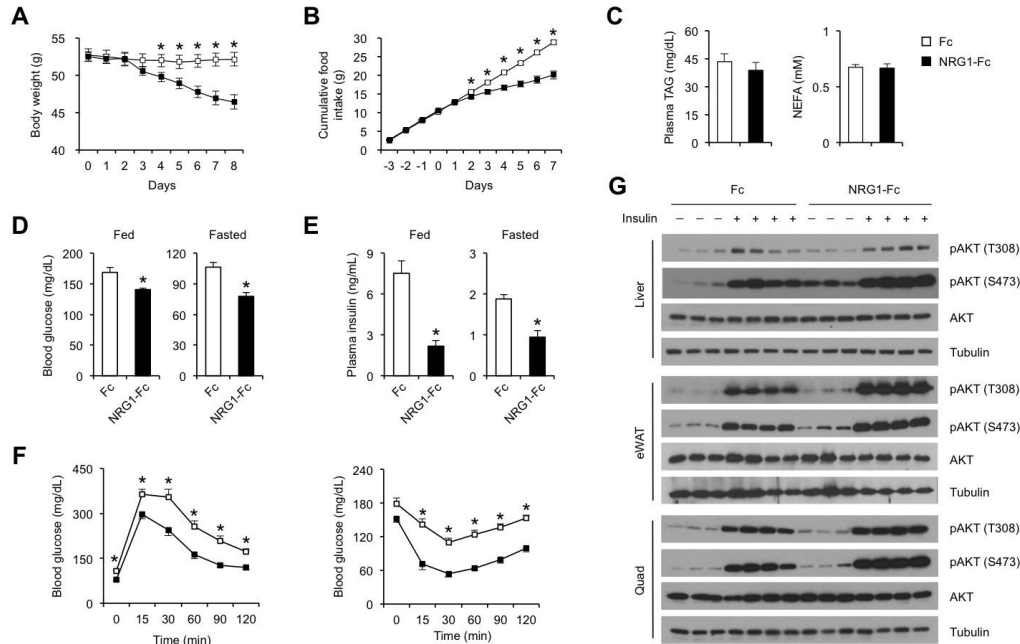
144

**Figure 5.4 Chronic effects of NRG1-Fc on energy balance and insulin sensitivity.**
(A, B) Body weight (A) and cumulative food intake (B) in HFD-fed mice treated with Fc (open, n=8) or NRG1-Fc (filled, n=8). (C) Plasma TAG (left) and NEFA (right) concentrations in treated mice. (E-F) Blood glucose (E) and plasma insulin (F) levels in HFD-fed mice treated with Fc (open, n=6) or NRG1-Fc (filled, n =7) measured under fed and fasted conditions. (F) Glucose tolerance test (GTT, left) and insulin tolerance test (ITT, right). (G) Immunoblots of total liver, eWAT and quadriceps muscle (Quad) lysates 15 min following intravenous insulin injection. Data represent mean ± sem. *p < 0.05, vs. Fc; two-tailed unpaired Student's t-test (C-E) or two-way ANOVA (A, B, F).
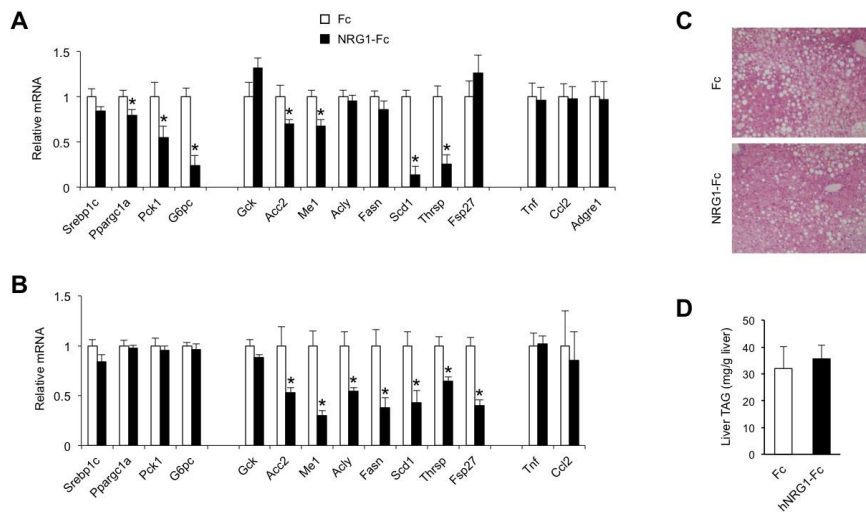


**Figure 5.5 Effects of chronic NRG1-Fc administration on hepatic gene expression and steatosis.**
(A) qPCR analysis of hepatic gene expression in HFD-fed mice treated with Fc (open, n=6) or NRG1-Fc (filled, n=6) and analyzed under fasted condition. (B) qPCR analysis of hepatic gene expression in HFD-fed mice treated with Fc (open, n=10) or NRG1-Fc (filled, n=12) and analyzed under fed condition. (C) H&E staining of liver sections. (D) Liver TAG content. Data represent mean ± sem. *p < 0.05, vs. Fc; two-tailed unpaired Student's t-test.
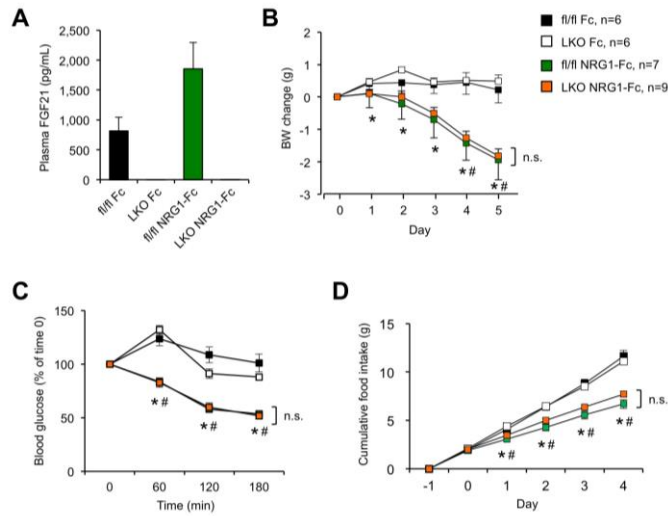
145

**Figure 5.6 Metabolic effects of NRG1-Fc in liver-specific FGF21 KO mice.**
(A) Plasma FGF21 levels in HFD-fed control (fl/fl) and FGF21 LKO mice after Fc or NRG1-Fc treatment, as indicated. (B-D) Changes in body weight (B), blood glucose (C) and cumulative food intake (D) in treated mice. Data represent mean ± sem. *$p < 0.05$, NRG1-Fc vs. Fc in LKO mice; #$p < 0.05$, NRG1-Fc vs. Fc in fl/fl mice; n.s. not significant; two-tailed unpaired Student's t-test.
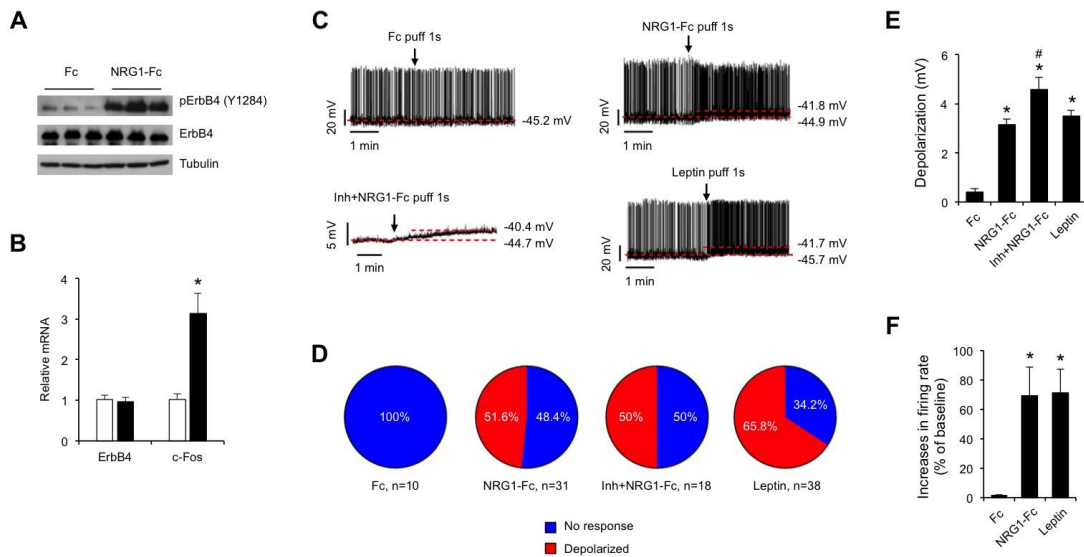


**Figure 5.7 Direct effects of NRG1-Fc on POMC neurons.**
(A) Immunoblots of hypothalamic lysates from mice treated with Fc or NRG1-Fc (300 ug/kg) for 30 min. (B) qPCR analysis of hypothalamic gene expression from mice treated with Fc (open, n=4) or NRG1-Fc (filled, n=4) for 45 min. (C) Representative traces of POMC neurons responding to 1s puff of Fc, NRG1-Fc (300 nM), NRG1-Fc in the presence of synaptic inhibitors (TTX+AP5+CNQX+bicuculline) in infusion buffer (Inh+NRG1-Fc), or leptin (300 nM). (D) Proportion of cells recorded that responded with depolarization >2mV (red) or with no change in resting membrane potential (blue) following the indicated treatments. (E-F) Depolarization (E) and increase in firing rate (F) of POMC neurons after the above treatments. Data represent mean ± sem. *$p < 0.05$ by one-way ANOVA and # $p<0.05$ vs. NRG1-Fc.
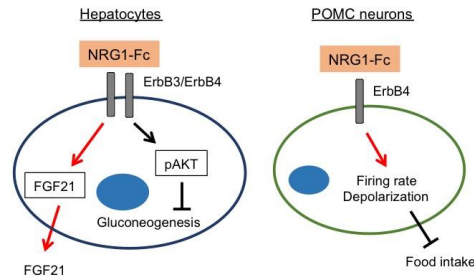
146

**Figure 5.8 Model depicting the pleiotropic effects of NRG1-Fc in hepatocytes and POMC neurons.**
NRG-Fc lowers blood glucose by activating hepatic AKT signaling to inhibit gluconeogenesis, while suppressing food intake by depolarizing and increasing the firing rate of POMC neurons.

# References

Bean, J.C., Lin, T.W., Sathyamurthy, A., Liu, F., Yin, D.M., Xiong, W.C., and Mei, L. (2014). Genetic labeling reveals novel cellular targets of schizophrenia susceptibility gene: distribution of GABA and non-GABA ErbB4-positive cells in adult mouse brain. J Neurosci 34, 13549-13566.

Brown, M.S., and Goldstein, J.L. (2008). Selective versus total insulin resistance: a pathogenic paradox. Cell Metab 7, 95-96.

Burgess, A.W. (2008). EGFR family: structure physiology signalling and therapeutic targets. Growth Factors 26, 263-274.

Cai, C., Lin, M., Xu, Y., Li, X., Yang, S., and Zhang, H. (2016). Association of circulating neuregulin 4 with metabolic syndrome in obese adults: a cross-sectional study. BMC Med 14, 165.

Canto, C., Pich, S., Paz, J.C., Sanches, R., Martinez, V., Orpinell, M., Palacin, M., Zorzano, A., and Guma, A. (2007). Neuregulins increase mitochondrial oxidative capacity and insulin sensitivity in skeletal muscle cells. Diabetes 56, 2185-2193.

Canto, C., Suarez, E., Lizcano, J.M., Grino, E., Shepherd, P.R., Fryer, L.G., Carling, D., Bertran, J., Palacin, M., Zorzano, A., et al. (2004). Neuregulin signaling on glucose transport in muscle cells. J Biol Chem 279, 12260-12268.

Chen, Z., Wang, G.X., Ma, S.L., Jung, D.Y., Ha, H., Altamimi, T., Zhao, X.Y., Guo, L., Zhang, P., Hu, C.R., et al. (2017). Nrg4 promotes fuel oxidation and a healthy adipokine profile to ameliorate diet-induced metabolic disorders. Mol Metab 6, 863-872.

Cowley, M.A., Smart, J.L., Rubinstein, M., Cerdan, M.G., Diano, S., Horvath, T.L., Cone, R.D., and Low, M.J. (2001). Leptin activates anorexigenic POMC neurons through a neural network in the arcuate nucleus. Nature 411, 480-484.

Czajkowsky, D.M., Hu, J., Shao, Z., and Pleass, R.J. (2012). Fc-fusion proteins: new developments and future perspectives. EMBO Mol Med 4, 1015-1028.

Dai, Y.N., Zhu, J.Z., Fang, Z.Y., Zhao, D.J., Wan, X.Y., Zhu, H.T., Yu, C.H., and Li, Y.M. (2015). A case-control study: Association between serum neuregulin 4 level and non-alcoholic fatty liver disease. Metabolism 64, 1667-1673.

Ennequin, G., Boisseau, N., Caillaud, K., Chavanelle, V., Etienne, M., Li, X., Montaurier, C., and Sirvent, P. (2015a). Neuregulin 1 affects leptin levels, food intake and weight gain in normal-weight, but not obese, db/db mice. Diabetes Metab 41, 168-172.

Ennequin, G., Boisseau, N., Caillaud, K., Chavanelle, V., Etienne, M., Li, X., and Sirvent, P. (2015b). Neuregulin 1 Improves Glucose Tolerance in db/db Mice. PLoS One 10, e0130568.

Falls, D.L. (2003). Neuregulins and the neuromuscular system: 10 years of answers and questions. J Neurocytol 32, 619-647.

Gao, R., Zhang, J., Cheng, L., Wu, X., Dong, W., Yang, X., Li, T., Liu, X., Xu, Y., Li, X., et al. (2010). A Phase II, randomized, double-blind, multicenter, based on standard therapy, placebo-controlled study of the efficacy and safety of recombinant human neuregulin-1 in patients with chronic heart failure. J Am Coll Cardiol 55, 1907-1914.

Guo, L., Zhang, P., Chen, Z., Xia, H., Li, S., Zhang, Y., Kobberup, S., Zou, W., and Lin, J.D. (2017). Hepatic neuregulin 4 signaling defines an endocrine checkpoint for steatosis-to-NASH progression. J Clin Invest.

Harari, D., Tzahar, E., Romano, J., Shelly, M., Pierce, J.H., Andrews, G.C., and Yarden, Y. (1999). Neuregulin-4: a novel growth factor that acts through the ErbB-4 receptor tyrosine kinase. Oncogene 18, 2681-2689.

Hernandez, C., Molusky, M., Li, Y., Li, S., and Lin, J.D. (2010). Regulation of hepatic ApoC3 expression by PGC-1beta mediates hypolipidemic effect of nicotinic acid. Cell Metab 12, 411-419.

Jabbour, A., Hayward, C.S., Keogh, A.M., Kotlyar, E., McCrohon, J.A., England, J.F., Amor, R., Liu, X., Li, X.Y., Zhou, M.D., et al. (2011). Parenteral administration of recombinant human neuregulin-1 to patients with stable chronic heart failure produces favourable acute and chronic haemodynamic responses. Eur J Heart Fail 13, 83-92.

Jiang, J., Lin, M., Xu, Y., Shao, J., Li, X., Zhang, H., and Yang, S. (2016). Circulating neuregulin 4 levels are inversely associated with subclinical cardiovascular disease in obese adults. Sci Rep 6, 36710.

Lee, M., Kwon, D.Y., Kim, M.S., Choi, C.R., Park, M.Y., and Kim, A.J. (2016). Genome-wide association study for the interaction between BMR and BMI in obese Korean women including overweight. Nutr Res Pract 10, 115-124.

Li, S., Liu, C., Li, N., Hao, T., Han, T., Hill, D.E., Vidal, M., and Lin, J.D. (2008). Genome-wide coactivation analysis of PGC-1alpha identifies BAF60a as a regulator of hepatic lipid metabolism. Cell Metab 8, 105-117.

Liu, C., and Lin, J.D. (2011). PGC-1 coactivators in the control of energy metabolism. Acta Biochim Biophys Sin (Shanghai) 43, 248-257.

Liu, X., Gu, X., Li, Z., Li, X., Li, H., Chang, J., Chen, P., Jin, J., Xi, B., Chen, D., et al. (2006). Neuregulin-1/erbB-activation improves cardiac function and survival in models of ischemic, dilated, and viral cardiomyopathy. J Am Coll Cardiol 48, 1438-1447.

Markan, K.R., Naber, M.C., Ameka, M.K., Anderegg, M.D., Mangelsdorf, D.J., Kliewer, S.A., Mohammadi, M., and Potthoff, M.J. (2014). Circulating FGF21 is liver derived and enhances glucose uptake during refeeding and overfeeding. Diabetes 63, 4057-4063.

Markan, K.R., and Potthoff, M.J. (2016). Metabolic fibroblast growth factors (FGFs): Mediators of energy homeostasis. Semin Cell Dev Biol 53, 85-93.

Mei, L., and Xiong, W.C. (2008). Neuregulin 1 in neural development, synaptic plasticity and schizophrenia. Nat Rev Neurosci 9, 437-452.

Mendes-Ferreira, P., Maia-Rocha, C., Adao, R., Mendes, M.J., Santos-Ribeiro, D., Alves, B.S., Cerqueira, R.J., Castro-Chaves, P., Lourenco, A.P., De Keulenaer, G.W., et al. (2016). Neuregulin-1 improves right ventricular function and attenuates experimental pulmonary arterial hypertension. Cardiovasc Res 109, 44-54.

Meng, Z.X., Gong, J., Chen, Z., Sun, J., Xiao, Y., Wang, L., Li, Y., Liu, J., Xu, X.Z.S., and Lin, J.D. (2017). Glucose Sensing by Skeletal Myocytes Couples Nutrient Signaling to Systemic Homeostasis. Mol Cell 66, 332-344 e334.

Molusky, M.M., Li, S., Ma, D., Yu, L., and Lin, J.D. (2012). Ubiquitin-specific protease 2 regulates hepatic gluconeogenesis and diurnal glucose metabolism through 11beta-hydroxysteroid dehydrogenase 1. Diabetes 61, 1025-1035.

Owen, B.M., Mangelsdorf, D.J., and Kliewer, S.A. (2015). Tissue-specific actions of the metabolic hormones FGF15/19 and FGF21. Trends Endocrinol Metab 26, 22-29.

Rosell, M., Kaforou, M., Frontini, A., Okolo, A., Chan, Y.W., Nikolopoulou, E., Millership, S., Fenech, M.E., MacIntyre, D., Turner, J.O., et al. (2014). Brown and white adipose tissues: intrinsic differences in gene expression and response to cold exposure in mice. Am J Physiol Endocrinol Metab 306, E945-964.

Salinas, Y.D., Wang, L., and DeWan, A.T. (2016). Multiethnic genome-wide association study identifies ethnic-specific associations with body mass index in Hispanics and African Americans. BMC Genet 17, 78.

Schneider, M.R., and Wolf, E. (2009). The epidermal growth factor receptor ligands at a glance. J Cell Physiol 218, 460-466.

Suarez, E., Bach, D., Cadefau, J., Palacin, M., Zorzano, A., and Guma, A. (2001). A novel role of neuregulin in skeletal muscle. Neuregulin stimulates glucose uptake, glucose transporter translocation, and transporter expression in muscle cells. J Biol Chem 276, 18257-18264.

Wang, G.X., Zhao, X.Y., and Lin, J.D. (2015). The brown fat secretome: metabolic functions beyond thermogenesis. Trends Endocrinol Metab 26, 231-237.

Wang, G.X., Zhao, X.Y., Meng, Z.X., Kern, M., Dietrich, A., Chen, Z., Cozacov, Z., Zhou, D., Okunade, A.L., Su, X., et al. (2014). The brown fat-enriched secreted factor Nrg4 preserves metabolic homeostasis through attenuation of hepatic lipogenesis. Nat Med 20, 1436-1443.

Wu, B., and Sun, Y.N. (2014). Pharmacokinetics of Peptide-Fc fusion proteins. J Pharm Sci 103, 53-64.

Zhan, C., Zhou, J., Feng, Q., Zhang, J.E., Lin, S., Bao, J., Wu, P., and Luo, M. (2013). Acute and long-term suppression of feeding behavior by POMC neurons in the brainstem and hypothalamus, respectively. J Neurosci 33, 3624-3632.

# Chapter 6
## Conclusions and Future Perspectives

**Single-cell RNA sequencing unravels liver heterogeneity in NASH**

NASH is an inflammatory condition that progresses do deadlier sequellae such as cirrhosis and hepatocellular carcinoma, which presently lack therapies. NASH presents with major hallmarks that define disease: cell damage and aberrant lipid accumulation in the liver, inflammation, and reactive fibrosis. These hallmarks are interrelated, but how they contribute to each other is not understood. Part of the reason NASH pathophysiology has been difficult to dissect is the multi-factorial nature of the disease and the heterogeneity of cell types in the liver. The complexity of the paracrine network dictating liver function further complicates disease mechanism. In my thesis research, I utilized scRNA-seq to deconvolute the heterogeneity of liver cells and uncover their role in NASH. We began to evaluate the transcriptional changes that specific NPC subsets including stellate cells, macrophages, and T cells undergo in disease.

Initially, we sought to clarify the contributions of each different cell type, and also to define the cross-talk system among these cells, to begin to connect these major hallmarks and create an overarching scheme for NASH pathogenesis. After identifying the major NPC subsets including cholangiocytes, endothelial cells, stellate cells, macrophages, T cells, and B cells, we mapped known secreted ligand and membrane receptor expression to the NPCs and found each cell type expressed a specific subset of ligands and receptors, which we confirmed at a proteomic level. By integrating this matrix of enriched ligands and receptors with known ligand-receptor interactions, we constructed a hepatic paracrine network, which we found to be conserved from mouse to human. We found the ligands and receptor expression to be altered in every cell type profiled, and the major hubs of paracrine signaling appeared to be stellate cells and macrophages. We deemed the ligands restricted to expression in stellate cells as the stellakines, which included factors that interact with receptors on endothelial cells, as well as inflammatory cytokines including CXCL1 and CCL11. HSC production of these cytokines was regulated by Il11, placing

HSCs and stellakines in an immune-regulatory axis. Furthermore, we uncovered that HSCs express vaso-regulatory membrane receptors including EDNRB, ADRA2B, and VIPR1. *In vitro* stimulation of mouse and human HSCs with cognate ligands for these receptors resulted in calcium influx, a known regulator of vascular tone. We therefore functionally demonstrated that HSCs are a major player in paracrine signaling, extending beyond production of extracellular matrix material.

**Profiling expansion of NASH-associated macrophages in disease**

By profiling immune cells, we observed a dramatic expansion of liver macrophages which resembled tissue-resident Kupffer cells. On further examination, we uncovered this NASH-associated macrophage (NAM) population, marked by expression of the Trem2 gene. To further study NAMs, we generated a Trem2 Cre knock-in mouse line, and crossed it with flox tdTomato reporter to examine where in tissue Trem2 is expressed. While Trem2 expressing cells appear in every tissue we profiled including brain, intestine, colon, kidney, pancreas, liver, brown and white adipose, lung, heart, and quadriceps, co-staining with F4/80 indicated that this Trem2 expression is specific to macrophages. By tracing hematopoietic cells in a bone-marrow transplant, we found that NAMs derive from hematopoietic sources in the bone marrow, as opposed to differentiating *in situ* from tissue-resident macrophage populations, during diet-induced NASH pathogenesis. This potentially explains why macrophages showing any past expression of Trem2 seem to be found in every tissue of the body that we profiled.

The NAM population transcriptionally displayed a propensity for antigen presentation, extracellular matrix remodeling, and phagocytosis. Given these findings, we hypothesize that this population plays a role in the pathogenesis of NASH. While previous work has indicated Trem2 is important for the homeostatic function of these macrophages in brain through clearance of amyloid plaques by microglia, we have shown that the gene itself has minor effects on our liver injury readouts in our dietary mouse NASH models. We compared Trem2 knockout mice with wild type on our Amylin NASH diet model. Profiling liver injury through ALT and AST, we found there was no difference in comparing knockouts to wild type, and also found no transcriptional differences by whole-liver qPCR in inflammatory cytokine profile or fibrosis. Histologically, there was no difference in steatosis or scarring in the liver of Trem2 knockout

mice. Interestingly, we also did not observe a loss of NAM expression profile in the Trem2 knockout through genes such as Gpnmb and Ms4a7, which in the brain and adipose tissue was previously shown to abrogate the generation of the NAM expression profile in macrophage transcriptomes. How Trem2 may be important in brain macrophage differentiation but not in liver remains unknown. It is possible that NASH represents too severe of a phenotype for Trem2 expressing Kupffer-like cells to respond to as the microglia might in Alzheimer's disease. Furthermore, there are likely different cues that regulate the development of NAMs between the amyloid plaques of the brain and pathological hallmarks of NASH. Presently, it is unknown if Trem2 reacts to paracrine factors from injured hepatocytes, or inflammatory cytokines from other NPCs such as activated HSCs, or possibly if Trem2 responds directly to lipid droplets in the NASH liver. The knowledge that Trem2 macrophages arise from bone-marrow-derived macrophages allows us to focus our studies on a specific population of progenitors and elucidate the developmental signals that regulate NAMs. Future studies will focus on exposure of bone-marrow-derived macrophages to different factors including purified lipid droplets, regulatory cytokines and other stellakines, and damaged hepatocytes, to determine how Trem2 and the rest of the NAM signature are regulated.

The other major question from our NAM findings pertains to their function. To begin to understand the function of Trem2 and the NAM population, our future studies will focus on the cell population as a whole, rather than one gene that marks the population. Our Trem2 Cre mouse is a powerful model that allows for targeted studies specifically on the NAM population. We may cross it with any flox line to delete specific genes in NAMs, evaluating the role that certain functions of NAMs play in NASH pathogenesis. To determine the end-all importance of them, we will cross Trem2 Cre with a floxed inducible diphtheria toxin receptor (iDTR) system to express the DTR specifically in NAMs. Injection of diphtheria toxin then allows for targeted ablation of the NAM population. With this, we may study the effects of NAMs on NASH, answering what their function is in pathophysiology. Elucidation of the native function of NAM will determine which pathways are critical for their effects on NASH, whether it is phagocytosis, or extracellular matrix remodeling. We may then target individual genes to flox and knock out in NAMs with our Trem2 Cre model and study those effects on NASH. A better understanding of

NAM regulation could pave the way for targeted treatments on this cell population and novel therapies for NASH.

**CD8+ T cell exhaustion in NASH liver and regulation of hepatocellular carcinogenesis**

In examining other large immune cell clusters from our scRNA-seq, we also discovered a shift in the T cell landscape to a state of exhaustion. The cytotoxic CD8+ T cells increased expression for exhaustion markers PD1, LAG3, HAVCR2, and EOMES in scRNA-seq NASH liver, and was confirmed by whole-liver qPCR in our murine models for NASH, suggesting that the NASH liver may contain exhausted T cells. This would represent an environment that is relatively tolerant to foreign material, injured cells, and tumor cells. We confirmed this by flow cytometry finding that NASH CD8+ T cells expressed significantly higher amounts of exhaustion markers PD1 and LAG3, with lower activity marker KLRG1. CD8+ effector function was abrogated in these T cells, as we show that NASH CD8+ T cells secrete significantly less IL2, IFNγ, and TNFα upon stimulation with PMA and ionomycin. This functional exhaustion was restricted to the liver in our NASH model, as flow cytometry of spleen and mesenteric lymph node populations revealed there was no increase of PD1 accompanied by loss of IL2, IFNγ, or TNFα secretion in secondary lymphoid subsets.

We found that the liver T cell exhaustion landscape is modulated by one of our previously studied adipose endocrine factors, NRG4. Prior work shows the adipokine NRG4 is protective from NASH, as overexpression of NRG4 reduces hepatocyte injury in our dietary NASH model, resulting in improved steatosis and fibrosis measured by qPCR and histology. Conversely, knockout of NRG4 results in worsened NASH phenotype, suggesting that NRG4 acts a checkpoint for NASH progression. We hypothesized that one mechanism through which NRG4 protects the liver from downstream injury in NASH may be interaction with T cells, which could act to survey and clear the liver of aberrant cells, such as cancer cells. Concordantly, we showed that transcription of our exhaustion markers such as PD1, LAG3, HAVCR2, EOMES, and TIGIT were significantly reduced by whole liver qPCR in the NRG4 transgenic mouse compared to the wild type in NASH. The increase of these markers on qPCR in the knockout mouse confirmed that NRG4 serves as an endocrine blockade on exhaustion in NASH liver T cells. As T cell exhaustion is believed to modulate progression to cancers, and our previous work suggests

154

NRG4 can act as a checkpoint for NASH progression, we tested if NRG4 could attenuate the NASH-HCC axis. We demonstrated that the NRG4 transgenic mouse is more resistant to tumor burden and weight loss in our dietary HCC model compared to wild type control, exhibiting fewer tumors and higher weight stability in later stages of feeding. Our exhaustion findings suggest a link between NRG4 and blockade of the NASH progression axis, and that NRG4 could sensitize CD8+ T cells to checkpoint blockade therapies.

As NRG4 acts in an endocrine fashion and could be used in a therapeutic sense, we envision the potential for synergistic therapies with checkpoint inhibition treatments such as PD1 blockade to increase efficacy in HCC treatment. While we will eventually investigate how checkpoint treatments could modulate T cell exhaustion to affect NASH, our major focus will be on the end stages of NASH, particularly HCC. At the present, it is still unclear if T cell function is homeostatic or pathologic. It could be argued that immune cells clear aberrant material such as dysfunctional parenchymal cells, or importantly, tumorigenic cells. In this sense, the T cells are responsible for this clearance, and exhaustion is causative of worsened pathology. Ablation of exhaustion would serve to reactivate the cytotoxicity of CD8+ T cells, providing a less tumorigenic environment in the liver. Conversely, cytotoxic T cells may represent an inflammatory population which is a byproduct of NASH pathology that further damage the parenchyma, worsening the phenotype. T cell exhaustion may represent the body's attempt to mitigate the inflammatory response, and in this case, checkpoint inhibition would be harmful to the initial hits in NASH. Our future work will combine NRG4 models including transgenic overexpression and knockout, as well as therapeutic treatment with injection of NRG4 peptides, alongside checkpoint blockade such as PD1 inhibition, to determine if reversal of exhaustion negates the beneficial effects of NRG4 in NASH. Beyond clarifying the mechanism of this NASH checkpoint, it will provide a potential combination therapy for HCC.

While this work on macrophages and T cells in NASH are presented as separate chapters, it is likely that their functions are intertwined, through some paracrine interactions. We have magnified our views of NASH hallmarks, such as steatosis, injury, and fibrosis, by determining specific phenotypes for each cell type in pathophysiology, such as disruption of stellakine secretion, transition of macrophages to the NAM phenotype, and exhaustion of cytotoxic CD8+

155

T cells. Yet, it remains unclear which of all of these hallmarks appear first, and how the first one may lead to the others. Our future directions will continue the curation of specific cell-cell communications that may regulate our cells of interest, under the possibility that the initial signal is an endocrine or paracrine one. We will additionally continue to probe the effects of exogenous lipid droplets on different liver NPCs to assess if the initial response is due directly to the aberrant steatosis. A deeper understanding of the chronology of each of these events will serve to generate a better understood and holistic scheme of NASH development, eventually paving the way for more accessible diagnostics and therapies.